Bio-inspired calcium phosphate mineralization through enzymatic approach

Jihye Lee

Sorbonne Université

Ecole doctorale 397 – Physique et Chimie des Matériaux

Laboratoire de Réactivité de Surface (LRS) – CNRS UMR 7197

Bio-inspired calcium phosphate mineralization through enzymatic approach

---

Par Jihye Lee

Thèse de doctorat de Physique et Chimie des Matériaux

Dirigée par Jessem Landoulsi et Clément Guibert

Présentée et soutenue publiquement le 10 octobre 2023

Devant un jury composé de :

Dr Fouzia Boulmedais	Directrice de recherche	Rapportrice
Pr François Guyot	Professeur des universités	Rapporteur
Dr David Carrière	Directeur de recherche	Examinateur
Dr Audrey Beaussart	Chargée de recherche	Examinatrice
Dr Jessem Landoulsi	Maître de Conférences	Directeur de thèse
Dr Clément Guibert	Maître de Conférences	Co-Directeur de thèse

Acknowledgement

I would like to express my deepest appreciation to all members of the jury for accepting the evaluation of the research project for 3 years doctoral school period. I appreciate Dr Fouzia Boulmedais and Pr. François Guyot for accepting the review of my thesis. I also thank Dr David Carrière and Dr Audrey Beaussart for the examination of my work.

I am also deeply indebted to all members of the individual monitoring committee, Dr Hélène Pernot, Prof Christian Bonhomme and Prof Pierre Schaaf for the monitoring and advice on my PhD work in the annual meetings.

Words cannot express my gratitude to my supervisors Dr Jessem Landoulsi and Dr Clément Guibert for accepting me for this PhD project and for their invaluable patience, feedback, support and time.

Many thanks to the people who worked together: Sandra Casale for TEM measurements and discussions, Adama Konaté for SEM measurements, and Antoine Miche for XPS measurements. I am also thankful to Pauline Cornette for showing me techniques of AFM in liquid and tip functionalization.

Thanks to the all members of the surface reactivity laboratory (LRS, UMR 7197) for welcoming me and supporting me for three years.

I could not have undertaken this journey without my friends and family in Korea. Thank you for encouraging and supporting me anytime.

Abstract

Biomineralization of calcium phosphate (CaP) is the process by which some organism builds hard mineralized tissues, such as bone, enamel and calcified cartilage. This process is regulated through various physicochemical factors and biochemical reactions, involving particularly matrix vesicles (MVs). MVs are small spherical bodies enriched with membrane transporters and enzymes, in particular alkaline phosphatase (ALP). This study investigates enzyme-assisted mineralization of CaP with a focus on the role of MVs. The study was conducted on two different systems: (i) the homogeneous phase, in which enzymes are present in the same phase as substrates of enzymes and calcium ions and (ii) the heterogeneous phase, in which ALP is immobilized on the surface.

The enzyme-assisted mineralization is investigated by modulating the catalytic activity of ALP followed by the addition of a divalent ion in homogeneous phase. Kinetic parameters related to the nucleation and growth of minerals were measured using light scattering measurements in real-time. The enzyme-assisted mineralization on the surface occurred near collagen fibrils. The mineralization of collagens was mainly investigated using atomic force microscopy (AFM) which examined the intra- and extra-fibrillar mineralization of collagens. This study will contribute to the understanding of CaP mineralization in vivo beyond chemical precipitation as it considered the biomolecules present in mineralizing tissues. This can be further expanded by recruiting different or more proteins or enzymes to understand their interactions and their impact on the mineralization process.

Keywords: Biomineralization, calcium phosphate, alkaline phosphatase, collagens, multilayers.

Résumé

La biominéralisation du phosphate de calcium (CaP) est le processus par lequel un organisme construit des tissus minéralisés durs, tels que l'os, l'émail et le cartilage calcifié. Ce processus est régulé par divers facteurs physico-chimiques et réactions biochimiques, impliquant en particulier les vésicules matricielles (VMs). Les VMs sont de petits corps sphériques enrichis de transporteurs membranaires et d'enzymes, en particulier la phosphatase alcaline (PAL). Cette étude porte sur la minéralisation du CaP assistée par des enzymes et plus particulièrement sur le rôle des vésicules matricielles. L'étude a été menée sur deux systèmes différents : (i) la phase homogène, dans laquelle les enzymes sont présentes dans la même phase que les substrats des enzymes et des ions calcium et (ii) la phase hétérogène, dans laquelle l'PAL est immobilisée à la surface.

La minéralisation assistée par enzyme est étudiée en modulant l'activité catalytique de l'PAL suivie de l'ajout d'un ion divalent en phase homogène. Les paramètres cinétiques liés à la nucléation et à la croissance des minéraux ont été mesurés en utilisant des mesures de diffusion de la lumière en temps réel. La minéralisation assistée par l'enzyme sur la surface s'est produite près des fibrilles de collagène. La minéralisation des collagènes a été principalement étudiée à l'aide de la microscopie à force atomique (AFM) qui a examiné la minéralisation intra- et extra-fibrillaire des collagènes. Cette étude contribuera à la compréhension de la minéralisation du CaP in vivo au-delà de la précipitation chimique, car elle prend en compte les biomolécules présentes dans les tissus qui se minéralisent. Elle peut être élargie en recrutant des protéines ou des enzymes différentes ou plus nombreuses afin de comprendre leurs interactions et leur impact sur le processus de minéralisation.

Mots-clés : Biominéralisation, phosphate de calcium, phosphatase alcaline, collagènes, multicouches

Table of contents

List of abbreviations

ACP	Amorphous calcium phosphate
ADP	Adenosine di-phosphate
AFM	Atomic force microscopy
ALP	Alkaline phosphatase
AMP	Adenosine mono-phosphate
ANK	Ankylosis
ATP	Adenosine tri-phosphate
ATR-FTIR	Attenuated total reflectance-Fourier transform infrared spectroscopy
BSP	Bone sialoprotein
Chem	Chemical mineralization
Col	Collagen
CPPD	Calcium pyrophosphate dihydrate
CT	Charge-Transfer
DCHA	Calcium-deficient hydroxyapatite
DCPA	Dibasic calcium phosphate anhydrate
DCPD	Calcium hydrogen phosphate dihydrate
DDS	Guanidine-extracted demineralized bovine dentin
d_H	Hydrodynamic diameter
DLS	Dynamic light scattering
DMP1	Dentin matrix protein
DMSO	Dimethylsulfoxyde
DSPP	Dentin sialophosphoprotein
ECM	Extracellular matrix
EDC	N-(3-dimethylaminopropyl)-N′-ethylcarbodiimide hydrochloride
ENPP1	Ectonucleotide pyrophosphatase/phosphodiesterase 1
FT-IR	Fourier-transform infrared spectroscopy
GAG	Glycosaminoglycan
Gla	Gamma-carboxyglutamic acid
Gly	Glycin
HA	Sodium hyaluronate
HAP	Hydroxyapatite.

Hep	Heparin
iep	Isoelectric point
MC3-E1	Mouse skull osteoblast cells
MEPE	Matrix extracellular phosphoglycoprotein
MilliQ	Ultrapure water
MUD	11-mercapto-1-undecanol
MUDA	11-mercaptoundecanoic acid
MV	Matrix vesicle
NCP	Non-collagenous protein
NHS	N-hydroxysuccinimide
OCN	Osteocalcin
OCP	Octacalcium phosphate
OPN	Osteopontin
PAA	Poly(acrylic acid)
PAH	Poly(allylamine hydrochloride)
pAsp	Polyaspartic acid
PC-1	Plasma cell membrane glycoprotein-1
PCCP	Polyelectrolyte-calcium complex-pre-precursor
PDDA	poly(diallyldimethylammonium chloride)
PEI	Polyethylenimine
Pi	Inorganic phosphate
PILP	Polymer-induced liquid precursor
PLP	Pyridoxal-5′-phosphate
pnp	para-nitrophenol
pnpp	para-nitrophenyl phosphate disodium salt hexahydrate
PPi	Inorganic pyrophosphate
PSS	Poly(sodium 4-styrenesulfonate)
QCM-D	Quartz crystal microbalance with dissipation monitoring
SER 102	Serine 102 position
SIBLING	Small integrin-binding ligand, N-linked glycoprotein
SLS	Static light scattering
Sub-Mg	α-glycerol phosphate magnesium salt hydrate
Sub-Na	rac-Glycerol-1-phosphate sodium salt hydrate

Sub	Substrate of enzymes
TA	Tannic acid
TCP	Tricalcium phosphate
TEM	Transmission electron microscopy

General introduction

Calcium phosphate (CaP) biomineralization is the process by which living organisms produce hard tissues such as bone, enamel, and calcified cartilage. This process involves multiple physicochemical and biochemical factors and remains not completely elucidated. The crystallization of CaP has been widely investigated in model homogeneous phases by precipitation from supersaturated solutions containing calcium and orthophosphate ions. These investigations led to the discovery of several transient phases of CaP minerals, the formation of which is governed by thermodynamic and kinetic factors. They also showed the strong impact of the experimental parameters on the mineralization process.

In vivo, the mechanism of CaP crystallization is more complex as it is regulated through various physicochemical factors and biochemical reactions, particularly matrix vesicles (MVs) in the extracellular matrix (ECM). MVs are small spherical bodies enriched with membrane transporters and enzymes. They are considered as the site where CaP minerals nucleate through two different processes: (i) accumulation of calcium ions by acidic phospholipids and annexin proteins and (ii) regulation of phosphate ions by several enzymes, particularly alkaline phosphatase (ALP). ALP catalyzes the production of orthophosphate ions leading to the initiation of the mineralization process. Minerals first form within MVs and are subsequently released in the vicinity of the collagen matrix for further mineralization. In this stage, it is still unclear how collagen interacts with minerals and how further mineralization occurs to yield the final oriented crystals of hydroxyapatites.

The biomineralization process mediated by MVs and involving collagen matrix mineralization is distinguished from the mineralization conducted in vitro by the fact that the process is controlled in time and in space with two important biological features: (i) homeostasis and (ii) compartmentalization. Homeostasis is a regulating process by which biological systems tend to maintain the internal environment of biological processes. In biomineralization, homeostasis, responsible for regulating mineral formation and phosphate ion levels, is controlled by various enzymes, especially ALP. The location of ALP, which is embedded in MVs with other proteins, and the mineralization in the vicinity of collagen occur then on well-defined distinct locations. This organization and division of a larger system into distinct, separate sections or compartments can be referred to as compartmentalization. Realization of the features is a key to understanding the process in a biological system.

The present PhD work focuses on the development and the investigation of biomimetic CaP mineralization by considering the aspects of homeostasis and compartmentalization in the ECM. For this purpose, ALP is incorporated to generate orthophosphate ions in situ. Moreover, the enzyme can be immobilized on the surface in order to segregate the spatial arrangement of CaP mineralization from the mineralizing solutions. The mechanism of enzyme-assisted mineralization is investigated in both homogeneous and heterogeneous phases. In the homogeneous phase, ALP is introduced in a solution containing the substrate of the enzyme and calcium ions. In the heterogeneous phase, ALP is immobilized using the layer-by-layer (LbL) technique on a flat surface followed by its exposure to a mineralization solution containing the substrate of the enzyme and calcium ions. The simplicity, versatility and nanoscale control of LbL assemblies allow the incorporation of a wide range of biomolecules especially, enzymes with preservation of their biological activities. In the present work, we investigate the possibility to incorporate both collagens and ALP in the same macromolecular assembly and probe the subsequent mineralization process.

This manuscript is organized into four chapters. The first chapter is a literature review describing the main aspects of CaP biomineralization in vivo, and the different strategies designing for biomimetic mineralization systems. This chapter also describes key considerations regarding the self-assembly of collagen and the challenge to incorporate this protein within multilayers in the presence of other macromolecules of biological interest.

The second chapter provides a detailed description of the experimental methods with some principles of the main analytical techniques used in this work.

The third chapter describes the enzyme-assisted mineralization in the homogeneous phase. The study focuses on determining how to control the mineralization by modulating enzymatic activity and further addition of a divalent ion, Mg^{2+}. The mineralization processes in different experimental conditions are studied using in situ real-time light scattering monitoring which provides information on quantitative kinetic parameters.

The fourth chapter shows the study of enzyme-assisted mineralization in the heterogeneous phase. For this purpose, ALP and collagen are immobilized on flat surfaces through the LbL technique. The enzyme-assisted mineralization in multilayers with and without collagen fibrils is studied over 7 days of mineralization using atomic force microscopy (AFM) and x-ray photoelectron spectroscopy (XPS). Moreover, the enzyme-assisted mineralization in the

heterogeneous phase is further studied focusing on the mineralization of collagen fibrils. It aims to probe the process of mineralization from early stages by monitoring the mineralization process in situ in real time.

In conclusion, the key results are briefly summarized and perspectives are discussed to highlight the future challenges.

Présentation générale

La biominéralisation du phosphate de calcium (CaP) est le processus par lequel les organismes vivants produisent des tissus durs tels que l'os, l'émail et le cartilage calcifié. Ce processus implique de multiples facteurs physicochimiques et biochimiques et n'est pas encore complètement élucidé. La cristallisation du CaP a été largement étudiée dans des phases homogènes modèles par précipitation à partir de solutions sursaturées contenant des ions calcium et orthophosphate. Ces études ont conduit à la découverte de plusieurs phases transitoires de minéraux de CaP, dont la formation est régie par des facteurs thermodynamiques et cinétiques. Elles ont également montré le fort impact des paramètres expérimentaux sur le processus de minéralisation.

In vivo, le mécanisme de cristallisation du CaP est plus complexe car il est régulé par divers facteurs physicochimiques et réactions biochimiques, en particulier les vésicules matricielles (MVs) dans la matrice extracellulaire (ECM). Les MVs sont de petits corps sphériques enrichis de transporteurs membranaires et d'enzymes. Elles sont considérées comme le site où les minéraux de CaP nucléent par le biais de deux processus différents : (i) l'accumulation d'ions calcium par les phospholipides acides et les protéines annexines et (ii) la régulation des ions phosphate par plusieurs enzymes, en particulier la phosphatase alcaline (ALP). L'ALP catalyse la production d'ions orthophosphates, ce qui conduit à l'initiation du processus de minéralisation. Les minéraux se forment d'abord à l'intérieur des MV et sont ensuite libérés à proximité de la matrice de collagène pour poursuivre la minéralisation. À ce stade, on ne sait toujours pas comment le collagène interagit avec les minéraux et comment la minéralisation se poursuit pour donner les cristaux orientés finaux d'hydroxyapatites.

Le processus de biominéralisation médié par les MV et impliquant la minéralisation de la matrice de collagène se distingue de la minéralisation réalisée in vitro par le fait que le processus est contrôlé dans le temps et dans l'espace avec deux caractéristiques biologiques importantes : (i) l'homéostasie et (ii) la compartimentation. L'homéostasie est un processus de régulation par lequel les systèmes biologiques tendent à maintenir l'environnement interne des processus biologiques. Dans la biominéralisation, l'homéostasie, responsable de la régulation de la formation des minéraux et des niveaux d'ions phosphate, est contrôlée par diverses enzymes, en particulier l'ALP. La localisation de l'ALP, qui est intégrée dans les MVs avec d'autres protéines, et la minéralisation à proximité du collagène se produisent alors sur des sites distincts bien définis. Cette organisation et cette division d'un système plus vaste en sections

ou compartiments distincts et séparés peuvent être appelées compartimentation. La mise en place expérimentale de modèles de ces deux caractéristiques est une clé pour comprendre le processus dans un système biologique.

Le présent travail de doctorat se concentre sur le développement et l'étude de la minéralisation biomimétique du CaP en mettant en lumière le rôle de l'homéostasie et de la compartimentation dans l'ECM. À cette fin, l'ALP est incorporée pour générer des ions orthophosphates in situ. De plus, l'enzyme peut être immobilisée sur une surface afin de dissocier la localisation de la minéralisation du CaP des solutions de minéralisation, contenant les précurseurs des minéraux. Le mécanisme de minéralisation assistée par enzyme est étudié dans des phases homogènes et hétérogènes. Dans la phase homogène, l'ALP est introduite dans une solution contenant le substrat de l'enzyme et des ions calcium. Dans la phase hétérogène, l'ALP est immobilisée à l'aide de la technique couche par couche (LbL) sur une surface plane, puis exposée à une solution de minéralisation contenant le substrat de l'enzyme et des ions calcium. La simplicité, la polyvalence et le contrôle à l'échelle nanométrique des assemblages LbL permettent l'incorporation d'une large gamme de biomolécules, en particulier des enzymes, tout en préservant leurs activités biologiques. Dans le présent travail, nous étudions la possibilité d'incorporer à la fois des molécules de collagène et de l'ALP dans le même assemblage macromoléculaire et de sonder le processus de minéralisation qui s'ensuit.

Ce manuscrit est organisé en quatre chapitres. Le premier chapitre est une revue de la littérature décrivant les principaux aspects de la biominéralisation du CaP in vivo, et les différentes stratégies de conception de systèmes de minéralisation biomimétiques. Ce chapitre décrit également les considérations clés concernant l'auto-assemblage du collagène et le défi d'incorporer cette protéine dans des multicouches en présence d'autres macromolécules d'intérêt biologique.

Le deuxième chapitre fournit une description détaillée des méthodes expérimentales avec quelques principes des principales techniques analytiques utilisées dans ce travail.

Le troisième chapitre décrit la minéralisation assistée par des enzymes dans la phase homogène afin de reproduire l'homéostasie. L'ALP est utilisée comme générateur de phosphate in situ. La minéralisation a été suivie en temps réel à l'aide de mesures de diffusion de la lumière. Les mesures ont fourni des paramètres cinétiques quantitatifs permettant de comprendre la nucléation et la croissance des minéraux. Dans cette étude, les effets de l'activité catalytique et des ions magnésium ont été étudiés en modulant la concentration du substrat et des ions magnésium dans la solution. L'augmentation de la concentration en substrat était directement

liée à l'amélioration de l'activité catalytique des enzymes. Elle a permis d'accélérer la nucléation et la croissance des minéraux. D'autre part, l'ajout d'ions magnésium n'était pas lié à l'activité catalytique, ce qui a entraîné des taux de nucléation similaires. Cependant, elle a retardé la croissance des minéraux avec l'apparition d'une structure intermédiaire distincte, de type coeur-coquille. Cette étude a montré a possibilité d'initier et de moduler la minéralisation du CaP par l'enzyme ALP.

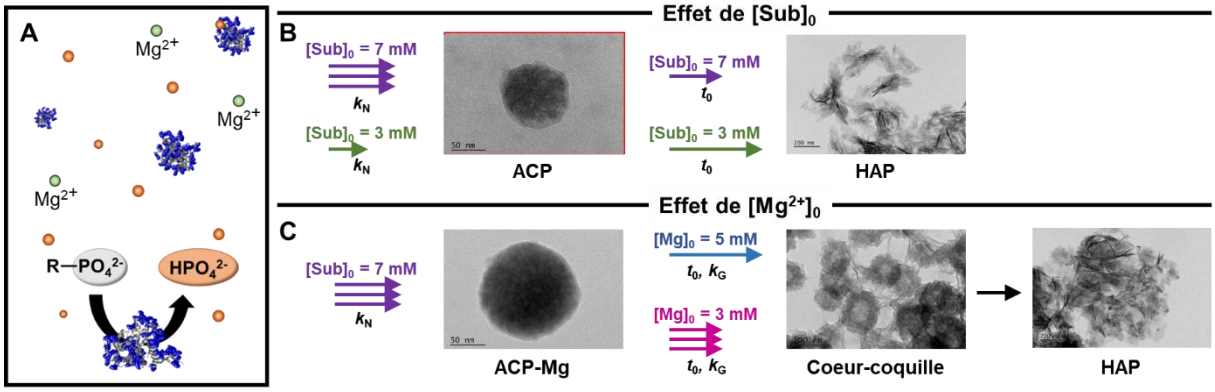

Figure 1 Minéralisation assistée par enzyme en phase homogène. (A) Schéma de la minéralisation assistée par enzyme. (B) Effet de l'activité catalytique. Plus il y a de substrat, plus la vitesse de nucléation (k_N) est rapide et plus le temps de croissance (t_0) est long. (C) L'effet des ions magnésium. L'ajout de magnésium n'influence pas k_N, mais retarde t_0 et le taux de croissance (k_G).

Le quatrième chapitre présente l'étude tenant compte à la fois de l'homéostasie et de la compartimentation. A cette fin, le système de minéralisation assistée par enzyme a été déplacé vers un système hétérogène. Pour ce faire, l'ALP et le collagène ont été immobilisés sur des surfaces planes par la technique LbL. Les minéralisations assistées par l'enzyme dans des multicouches avec et sans fibrilles de collagène ont été analysées à l'aide de la microscopie à force atomique (AFM), de la microscopie électronique à balayage (SEM) et de la spectroscopie photoélectronique à rayons X (XPS). Dans les premiers stades de la minéralisation, les multicouches sans collagène ont montré une désorption des multicouches en exposant la surface à la solution de minéralisation. Contrairement aux multicouches avec ALP, la minéralisation sur la surface avec ALP et collagènes a montré l'apparition de particules CaP le long des fibrilles de collagène, induisant une minéralisation étendue sur les multicouches. Cela a révélé que la présence de collagènes renforçait la minéralisation sur la base d'interactions préférentielles entre l'ALP et les collagènes. Le suivi en temps réel de la minéralisation assistée par enzyme sur les multicouches en présence de collagènes a également été présenté dans ce

chapitre afin d'explorer le processus de minéralisation : s'il s'agit d'une minéralisation intra ou extrafibrillaire. D'après le suivi, nous avons observé l'étape de nucléation, où augmente le nombre de particules globulaires au fil du temps, et l'élargissement des molécules de collagène avec une rugosité stable sur les surfaces des fibrilles. On peut conclure que la minéralisation intrafibrillaire se produit d'abord dans les multicouches avec des fibrilles de collagène.

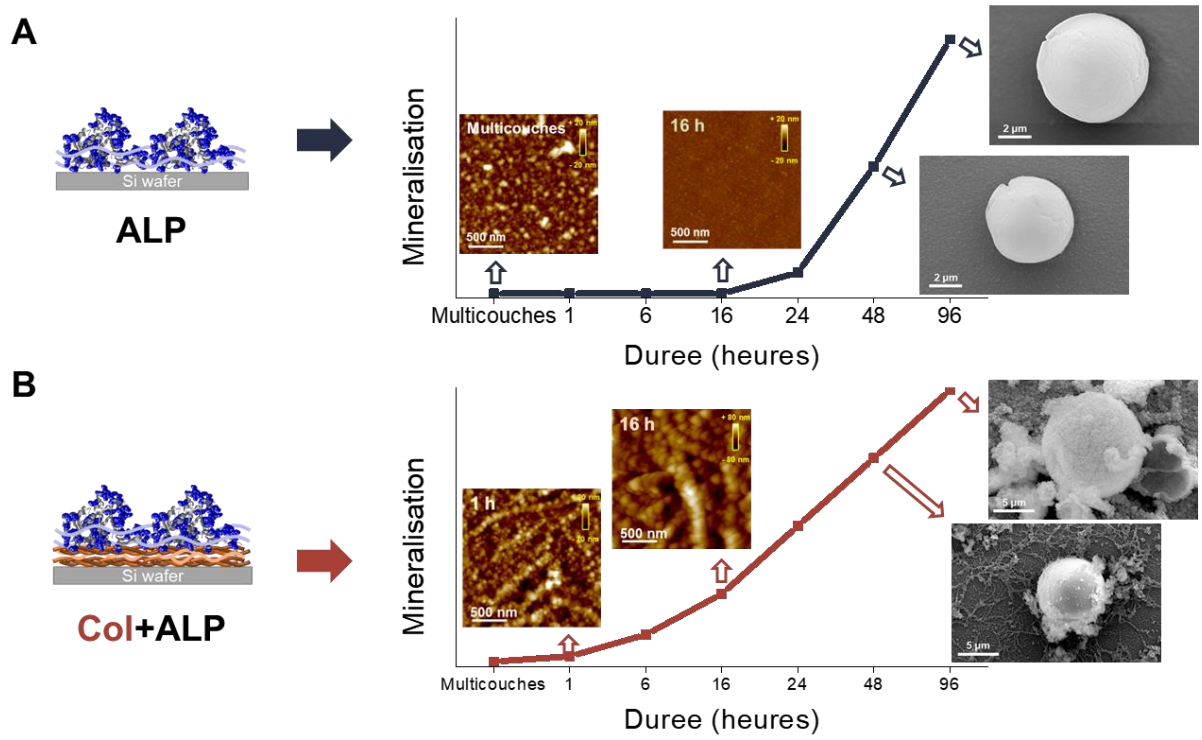

Figure 2 Comparaison de la minéralisation assistée par enzyme sur des multicouches. (A) multicouches avec seulement l'ALP. (B) multicouches avec collagène et ALP.

Ce travail de recherche a commencé par la question suivante : comment la biominéralisation se produit-elle ? L'étude a commencé par imiter un système biologique en apportant deux caractéristiques biologiques clés : l'homéostasie et la compartimentation. L'homéostasie a été réalisée en introduisant une enzyme, l'ALP, dans les systèmes. Le suivi de la minéralisation assistée par enzyme en temps réel dans une phase homogène par la méthode de diffusion de la lumière a été appliqué pour extraire les paramètres cinétiques afin d'étudier le processus dans différentes conditions : (i) l'effet de l'activité catalytique et (ii) l'effet de l'ajout d'ions magnésium. Ensuite, il est envisagé d'apporter les deux caractéristiques biologiques en combinant la minéralisation assistée par enzyme et la minéralisation assistée par la surface. Dans ce but, l'ALP a été immobilisée en utilisant l'assemblage LbL. L'étude a montré le rôle du collagène et de la minéralisation intrafibrillaire dans les premières étapes. Ce travail montre

l'intérêt de l'étude sur la minéralisation biomimétique du CaP pour expliquer comment la biominéralisation se produit. Cependant, il reste encore des questions telles que la régulation précise dans les systèmes biologiques, le rôle des protéines non collagéniques et le devenir des minéraux formés. À cet égard, l'un des aspects de la perspective est d'étendre le système à des systèmes multiprotéiques qui incluent différentes protéines impliquées dans la minéralisation, telles que la fétuine. L'autre perspective consiste à suivre la minéralisation associée à l'évolution des propriétés mécaniques. On s'attend à ce que la minéralisation modifie le module d'Young, en particulier dans le cas d'une minéralisation étendue.

Chapter 1. State of the art

1 Biomineralization

Biomineralization is a process, which is responsible for the deposition and organization of inorganic minerals within soft tissues. Bone, teeth, sea shells, and sponges are some examples of mineralized tissues (Figure 1.1A). In vertebrates, skeletal systems are vital components mainly composed of calcium phosphate (CaP) minerals. The formation of mineralizing tissues is based on complex processes combining various cellular and molecular components. For example, bones are rigid organs composed of collagen fibers, CaP, and other proteins in the extracellular matrix [1]. Therefore, biomineralization is carried out through intricate interplays of various biological components to produce and control the mineralization in cells and extracellular matrix.

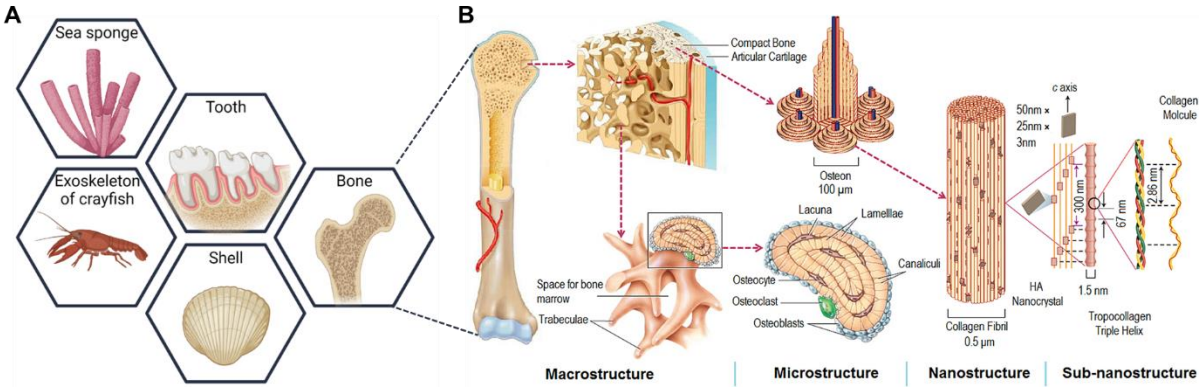

Figure 1. 1 Biomineralization. (A) Examples of mineralized tissues (B) Hierarchical structure organization of bone [2].

2 Bone tissue

2.1 General description

Bone is a natural well-structured composition containing both organic and inorganic components. The organic component primarily consists of proteins such as collagens, while the inorganic component is mainly composed of CaP, specifically hydroxyapatite (HAP). The structure of bone is hierarchically divided into several levels in different scales from macro- to sub-nano scales (Figure 1.1B) [2, 3]. The macroscale level represents the whole bone which can be classified as compact bone (cortical bone) and trabecular bone (cancellous bone). The compact bone is almost solid with osteons as building blocks surrounded by blood vessels, whereas trabecular bone has a porous network of trabeculae filled with bone marrow. At the microscale, the osteons have a lamellar structure, with individual lamella consisting of fibers

arranged in geometrical patterns. The fibers are composed of mineralized collagen fibrils with HAP at the nano and sub-nano scale.

The process of skeletal change, known as bone remodeling, is a tightly regulated process by mineralizing cells [4]. The equilibrium between the process of bone resorption and bone formation ensures the continuous adaptation of bones to changing mechanical loads, microdamage repair, and the preservation of bone strength.

2.2 Cells

Cells are the control tower of mineralization by starting the creation of the organic matrix which becomes mineralized, controlling the ion concentrations in the matrix, and signaling the entire process. The coordinated work of the cells is crucial to balance and regulate mineralization.

In bones, several types of cells are found in the mineralizing tissues; Osteoblast, Osteoclast, and Osteocytes (Figure 1.2). Osteoblasts are mononucleate square-shaped cells secreted by stem cells. They are attached to the surface of bones representing 4~6 % of total bone cells. The cells are responsible for bone forming by creation and secretion of the bone matrix through two steps: (i) formation of organic matrix constituted with collagens, non-collagenous protein, and proteoglycans, (ii) mineralization of matrix by mainly releasing matrix vesicles (MVs) from apical membrane domain of osteoblast [5].

Osteocytes are cells embedded within the bone comprising 90~95 % of bone cells. They are placed in little pockets named lacunae, which communicate through small canaliculi connected with other osteocytes or with the surface of the osteoblast. The dendritic morphology of canaliculi serves as a large surface area in which calcium and phosphate exchange between plasma and bone [5, 6].

Osteoclasts are large (150~200 μm) and multinucleated (10~20 nuclei) cells secreted by blood stem cells. They closely attach to the bone matrix by binding their transmembrane receptors, called integrins, to a bone protein called vitronectin. They are responsible for the resorption of bones by creating a border where enzymes and H^+ ions are released causing the dissolution of the mineral and the digestion of the organic matrix [5, 6].

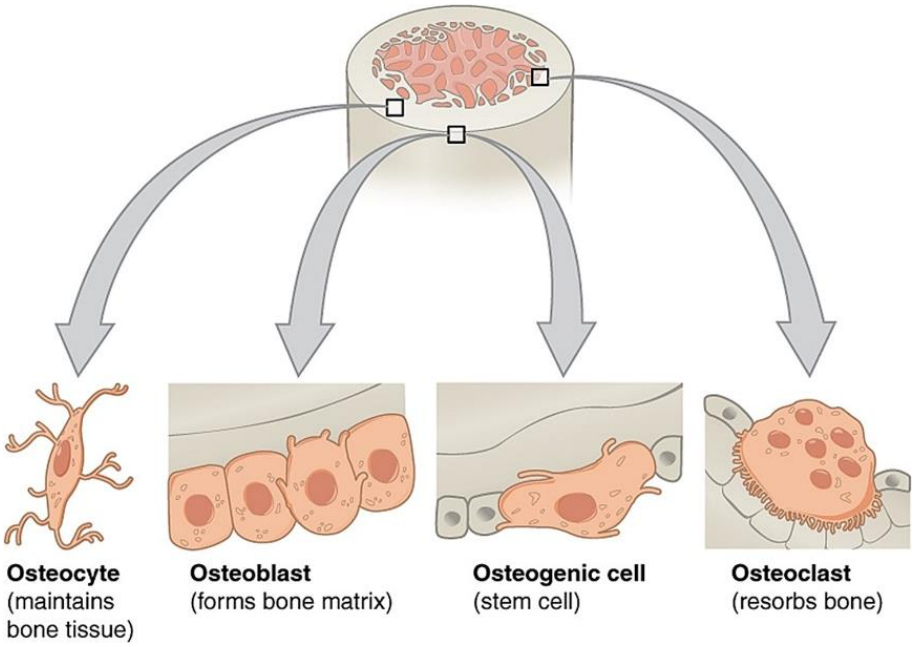

Figure 1. 2 Bone tissue cells [7]. There are four type of major bone cells: (i) osteogenic (stem) cells which may differentiate to become osteoblast, (ii) osteoblast which is responsible for secreting organic components of matrix and for mineralization, (iii) osteocyte which is trapped within calcified matrix to maintain it, and (iv) osteoclast which secrets acid and enzymes to dissolve bone matrix.

2.3 Extracellular matrix (ECM)

The ECM is a reservoir of bioactive molecules forming a complex network consisting of different multi-domains of macromolecules organized in a cell/tissue-specific manner. The components of ECM are related together to form a structurally stable composite, which determines the mechanical properties of the tissues. The major components of ECM are: (i) fibrous elements especially collagens (Cols), (ii) non-collagenous proteins (NCPs), and (iii) other molecules like different types of glycans.

2.3.1 Collagen (Col)

Col is the most abundant protein accounting for 30~35 % of the body proteins and 90 % of ECM proteins [8, 9]. There are 28 types of collagens classified on the basis of their structural organization, sequence homologies, location in the tissues and further diversity caused by molecular isoforms [10, 11]. During biomineralization in bone, type I collagen is predominantly found in ECM of mineralization with some trace amounts of type III and V [1, 5, 12]. The main characteristics and functions are presented in Table 1.1 [1, 11].

The molecular structure of type I collagens starts from “Gly-X-Y”, where X and Y can be any

amino acids but typically represent proline and hydroxyproline (~ 30 %) (Figure 1.3A). By repetition of the Gly-X-Y, single left-handed polypeptide α- chains are generated. Then, the coiling of three left-handed α-chains based on hydrogen bonding forms a right-handed triple helix named procollagen with a length of ~300 nm, a diameter of 1.4 nm and a molecular weight of ~300 kDa. The triple helix can be organized with identical α- chains (homotrimers) or distinct α- chains (heterotrimers). Collagens types I and V are heterotrimers and collagens type III is homotrimers. After the cleavage of the N- and C-terminal of procollagen by procollagen-peptidase, it becomes tropocollagen which self-assembles via fibrillogenesis to form fibrils and fibers. The self-assembly creates a highly organized pattern with the distance between longitudinally aligned tropocollagen helices as 67 nm (64 nm when dehydrated), known as D-spacing, which is the combination of a 40 nm hole zone and a 27 nm overlap zone. The D-spacing can be found by atomic force microscopy (AFM) as shown in Figures 1.3B and C. The space between assembled tropocollagen is 0.24 nm. The final fiber diameter varies from 300 nm to 1 μm with alternated d-spacing along the fiber [13, 14].

Table 1. 1 Different types of Collagens in bone mineralizing matrix [1, 11]

Type	Class	Composition	Function
I	Fibrillar	$\alpha 1[\mathrm{I}]_2\alpha 2[\mathrm{I}]$	Scaffolding, Interaction with other proteins that mineralize and deposit HAP
III	Fibrillar	$\alpha 1[\mathrm{III}]_3$	Presence in bone with trace amount Regulation of size of collagen fibrils
V	Fibrillar	$\alpha 1[\mathrm{V}]_2\alpha 2[\mathrm{V}]$ $\alpha 1[\mathrm{V}]\alpha 2[\mathrm{V}]\alpha 3[\mathrm{V}]$	Presence in bone with trace amount Regulation of size of collagen fibrils

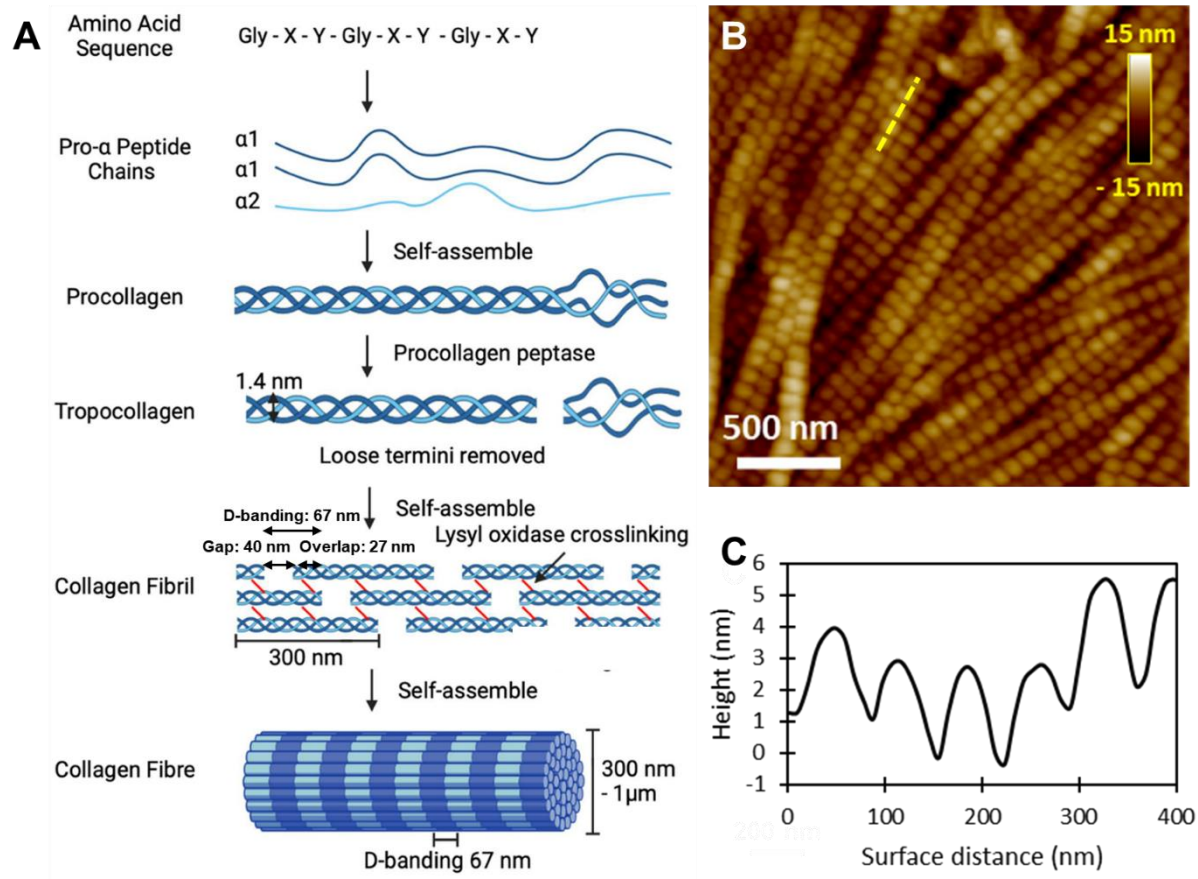

Figure 1. 3 Type I Collagen. (A) Structure from amino acid sequence to fiber [14]. (B) Height image of type I collagen matrix in a human capsule [15] (C) Scan line taken at the location indicated by the dashed line in (B) showing d-spacing (66.9 ± 3.2 nm) of individual fibrils.

2.3.2 Non-collagenous proteins

As bone tissues are subjected to regular remodeling, non-collagenous proteins (NCPs) play a pivotal role in the regulation of the mineralization process. NCPs are a complex set of molecules in mineralizing matrix taking 10~15 % of the total bone protein content [1]. They are classified based on their structural characteristics into three groups; glycoproteins, gamma-carboxyglutamic acid(Gla)-containing proteins, and proteoglycans (Figure 1.4). Glycoproteins undergo glycosylation, which is able to covalently attach to the protein backbone through carbohydrates. One of the well-known protein groups among glycoproteins is a small integrin-binding ligand, N-linked glycoproteins (SIBLINGs) such as osteopontin (OPN), bone sialoprotein (BSP), dentin matrix protein-1 (DMP1), dentin sialophosphoprotein (DSPP), and matrix extracellular phosphoglycoprotein (MEPE) [16]. The SIBLING family is highly acidic with abundant Arg-Gly-Asp motifs which mediate attachments on cells, collagens and minerals [17]. Although their precise roles in CaP crystallization are not fully elucidated, but they are

considered to be deeply involved in the regulation of mineralization and interact with CaP minerals. For example, OPN was identified between bone cells and minerals in the ECM of bone [18]. During bone formation, OPN increases the adhesion of osteoblasts and osteoclasts by concentrating on the mineralized collagen matrix [19, 20]. Concurrently, OPN binds to the surface of HAP through electrostatic interaction based on their acidic property. Some studies suggested that the attachment has an inhibitory effect on the formation and growth of minerals [21-23]. As SIBLINGs commonly contain Arg-Gly-Asp motifs, other SIBLINGs such as BSP, MEPE, DMP1 and DSPP are also considered to interact with HAP to enhance or inhibit the mineralization [24-28]. Gla-containing proteins allow the proteins to bind calcium ions. For example, osteocalcin (OCN) uses Gla residues to bind to HAP and regulates mineralization [16]. Proteoglycans are proteins with glycosaminoglycan (GAG) chains which are long, linear polysaccharide chains. Decorin, which is found in bone, dentin or other connective tissues, belongs to the proteoglycan group. It is known to work as a regulator of mineralization and to interact with other components in ECM [29].

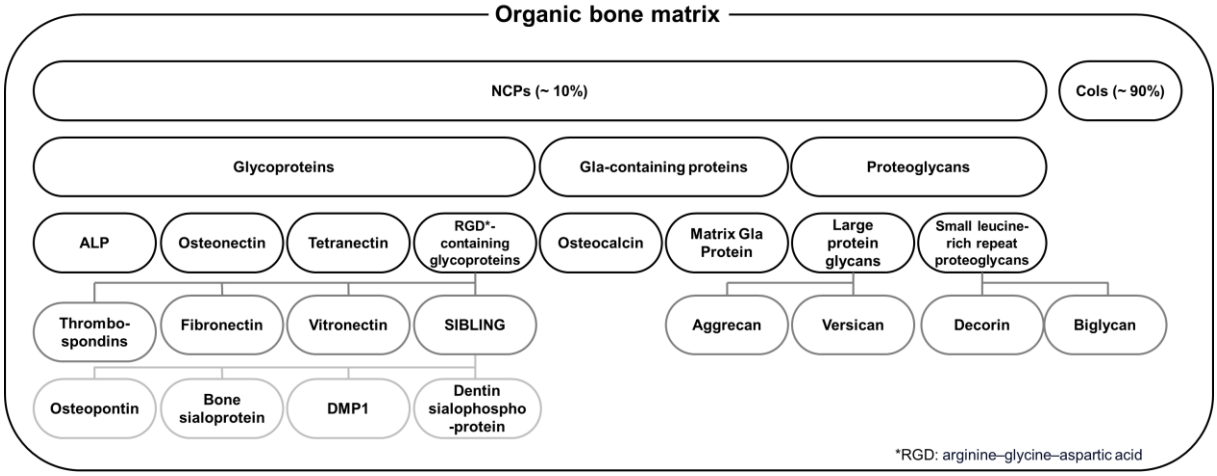

Figure 1. 4 NCPs in bone ECM. ECM is composed of ~ 90 % of Col and ~ 10 % of various types of NCPs roughly glycoproteins, Gla-containing proteins, and proteoglycans. Figure adapted with modifications from [16].

2.3.3 Matrix vesicles (MVs)

The MVs are small spherical bodies sized 20~300 nm in diameter found in the mineralizing matrix [30, 31]. As MVs are deeply involved in the initiation of mineralization in the ECM, the aspects will be detailed in the following section *3*.

2.3.4 Minerals

Bone is composed of 60~70 % of calcium phosphate mineral, 20~30 % of organic matrix and 10 % of water [8, 32]. The most abundant form of CaP in human bone was considered HAP with the chemical formula $Ca_{10}(PO_4)_6(OH)_2$ with a Ca/P ratio of 1.67 [33]. However, comprehensive studies on bone and synthetic apatite suggested that bone mineral is not pure HAP but associated with minor groups and impurities such as CO_3^{2-}, HPO_4^{2-}, Na^+, Mg^{2+} [34]. The intensive study on the formation of bioapatites discovered various CaP mineral phases (Table 1.2).

3 Matrix-vesicle mediated mineralization

MVs have a long history as the site where CaP mineralization is initiated in mineralizing tissues, particularly in bone and cartilage since they were discovered through ultrastructural analysis of mineralizing tissues in 1967 by Bonucci and Anderson [42-44]. They are secreted by the budding process from the specific region of the plasma membrane of bone tissue cells (Figure 1.5A). The budding process is observed by TEM in mouse skull osteoblast cells (MC3-E1). The vesicles firstly aggregate near the plasma membrane in a “sac” then pinch off and release into extracellular space (Figure 1.5A a-d) [45]. Although it is generated from the plasma membrane of cells, the membrane compositions of MVs are different from cells: they are enriched with enzymes and membrane transporters (Figure 1.5B), which are strongly involved in the mineralization process [30, 46].

3.1 Alkaline phosphatase (ALP)

Alkaline phosphatase (ALP, EC 3.1.3.1), firstly identified in bone by Robinson, is the most studied enzyme in MVs [48-50]. It is a glycoprotein bound to the plasma membrane of vesicles. It catalyzes the hydrolysis of phosphate esters to produce inorganic phosphate (Pi) as follows:

$$R - PO_4^{2-} + H_2O \rightarrow R - OH + HPO_4^{2-}$$

ALPs exist in different body tissues (liver, bone, intestine, kidney, intestinal, placental, germ cell) with different physiochemical properties but they catalyze the same reaction even though it is in different regions as a group of isoenzymes.

Table 1. 2 Variety of CaP phases. Table reproduced from ref [35].

	Name	Formula	Ca/P ratio	Examples of occurrence
Minerals found in bone	HAP	$Ca_{10}(PO_4)_6(OH)_2$	1.67	In an impure form (main impurities: CO_3^{2-}, Mg^{2+} and HPO_4^{2-}) as the mineral in bones and teeth. Pure HAP as a synthetic biomaterial.
	Calcium-deficient HAP (DCHA)	$Ca_{10-x}(HPO_4)_x(PO_4)_{6-x}(OH)_{2-x}$ (0<x<1)	1.5-1.67	Variation of HAP In dental enamel and dentin with carbonated form. Transformation from α-TCP or ACP [36]
	Octacalcium phosphate (OCP)	$Ca_8H_2(PO_4)_6{\cdot}5H_2O$	1.33	Found in the initial stage of bone mineralization Transient phase in precipitation of biological HAPs
	Magnesian whitlockite	Approximately $Ca_{18}Mg_2H_2(PO_4)_{14}$	1.29 - 1.36	Dental calculus, urinary and salivary calculi, carious lesions in teeth and other pathological calcifications
	α- and β-tricalcium phosphate (TCP)	α- and β-$Ca_3(PO_4)_2$	1.5	In bone tissue Play a role in bone remodeling and repair
Minerals found in biological tissues	Amorphous calcium phosphate (ACP)	$Ca_xH_y(PO_4)z{\cdot}nH_2O$ n = 3 - 4.5 15% - 20% H_2O	~ 2.2*	Found in various soft tissues Present in initial stages of bone mineralization
	Calcium hydrogen phosphate dihydrate (DCPD, Brushite)	$CaHPO_4{\cdot}2H_2O$	1.0	Dental and urinary calculi
	Calcium pyrophosphate dihydrate (CPPD)	$Ca_2P_2O_7{\cdot}2H_2O$ triclinic and monoclinic	1.0	Joints, particularly knee or other large peripheral joints
	Tetracalcium phosphate	$Ca_4(PO_4)_2O$	2.0	Dental calculus, teeth
	Dibasic calcium phosphate anhydrate (DCPA or monetite)	$CaHPO_4$	1.0	Not a nature component of biological tissues

* Different Ca/P ratios were reported: 1.2~2.2 [37-39] or ~ 1.5 [40, 41].

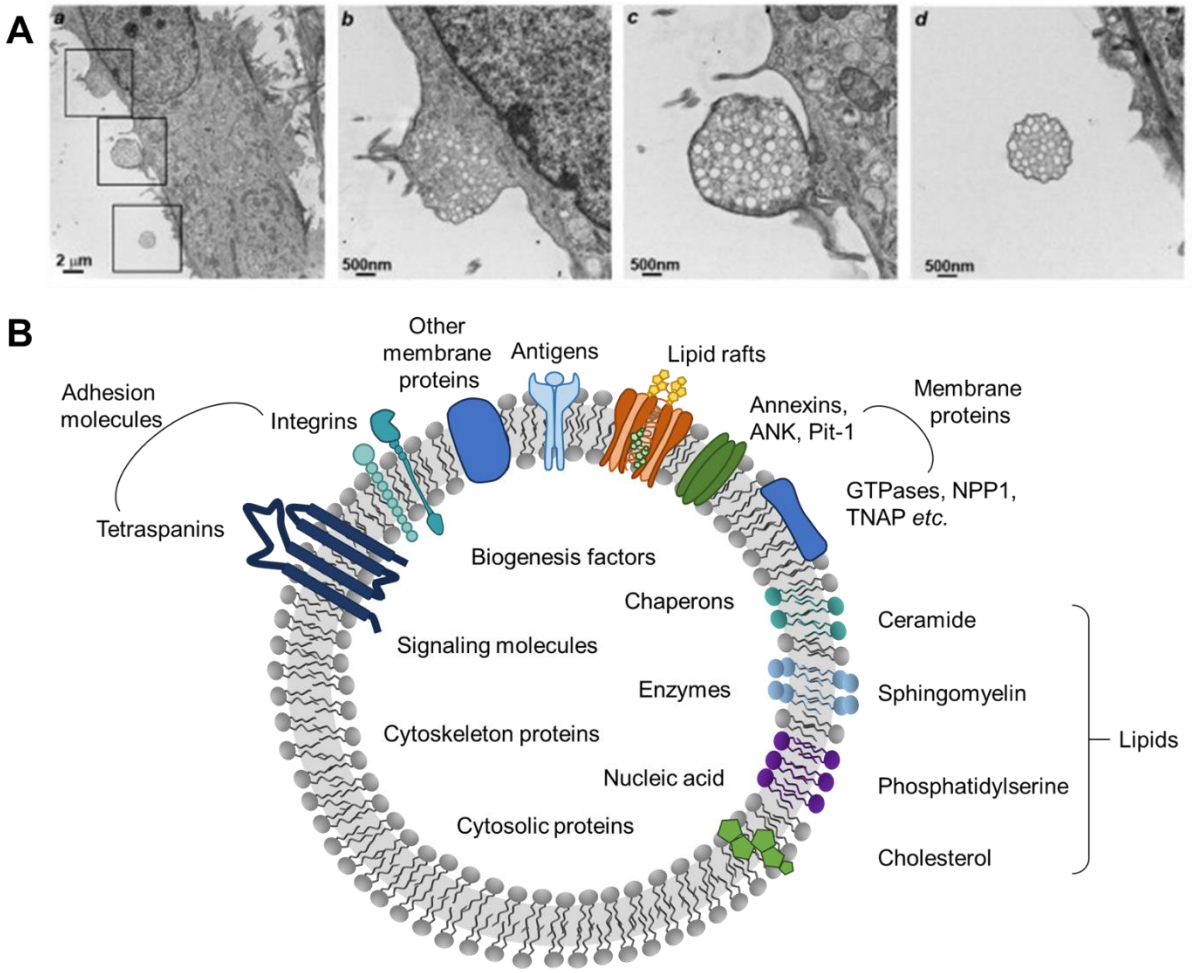

Figure 1. 5 MVs. (A) TEM observation of budding process of MVs from osteoblasts [45]. (B) Composition of MVs: different proteins and lipids inside or on membranes of MVs [47].

The structure of ALP is studied using intestinal ALP. It showed homodimers with monomers (molecular mass of 57.1 kDa) as shown in Figure 1.6 with dimensions 8.9 x 5.8 x 7.9 nm^3. In the solution, the hydrodynamic size of ALP was obtained as ~20 nm which suggested the predominant presence of a tetrameric form at pH $\geq$ 6 [51]. In mineralizing tissues, it binds to MV membranes through a glycosylphosphatidylinositol hydrophobic anchor covalently bound to the C-terminus of the enzyme [52, 53]. Each protein includes sites for three metal ions, two zinc and one magnesium ions which are necessary for enzymatic activity. The active site was identified as a serine residue located at position 102 (SER 102) of the protein chain. By coordination with serine, the three metal ions are involved in the formation of the nucleophile corresponding to the deprotonated hydroxyl group of serine (Figure 1.6B(i $\rightarrow$ ii)). The nucleophilic attack can subsequently occur on the phosphorus of the substrate, leading to the formation of a covalent phosphoserine intermediate (Figure 1.6B(ii $\rightarrow$ iii)). Then, the Zn^{2+} ion

coordinated to serine enables the release of alcohol and the Pi (Figure 1.6B(iv → i)). The latter, generated during the enzymatic reaction, is a competitive inhibitor of ALP that may potentially inactivate the enzyme (Figure 1.6B(i → iv)). The presence of calcium ions, present during the mineralization, may prevent the enzyme inactivation, as it precipitates with Pi at physiological pH [54, 55].

The substrate of ALP can be inorganic pyrophosphate (PPi), pyridoxal-5′-phosphate (PLP) and adenosine tri-/di-/mono-phosphate (ATP/ADP/AMP). Therefore, lack or mutation of ALP results in a disease known as hypophosphatasia which shows poorly mineralized bones, spontaneous fractures, and elevated concentration of PPi in ECM [56].

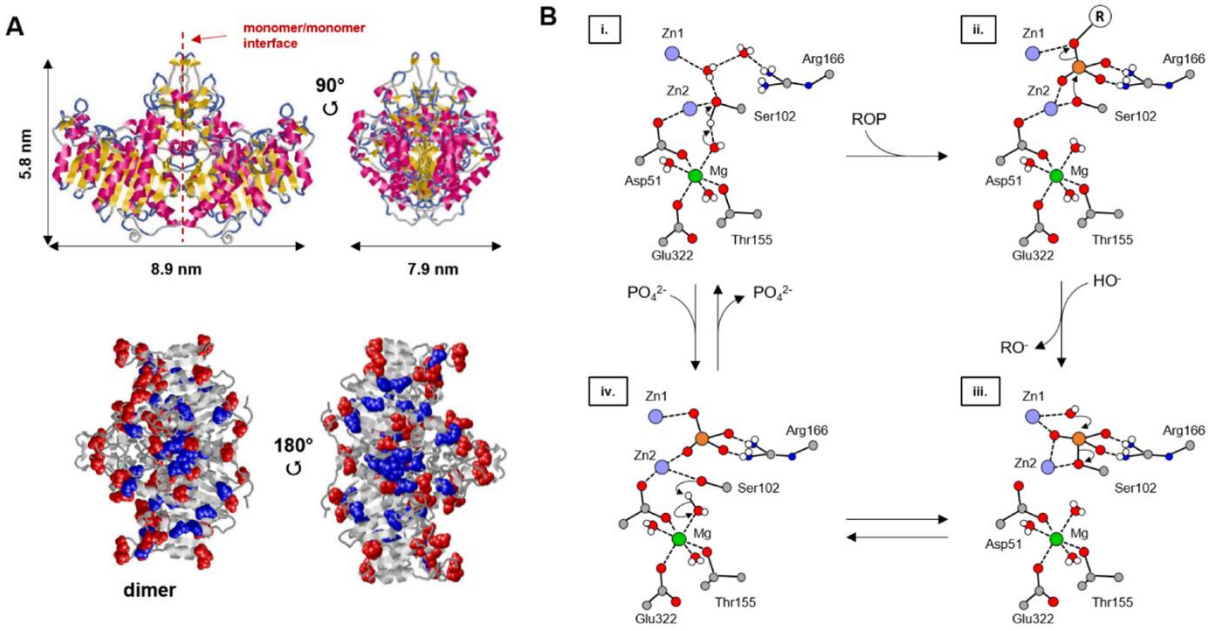

Figure 1. 6 Structure of ALP [54] (A) 3D structure of homodimer (protein database, P19111). Various perspectives illustrate the homodimer's dimensions and the arrangement of superimposed Glu (blue) and Asp (red) amino acids (adapted with modifications from reference [51]). (B) Catalytic mechanism of ALP [55]. Subset of hydrogen atoms shown. Initial stage (i. → ii.): hydroxide ion binds to magnesium ion, inducing Ser102's gamma oxygen deprotonation. Simultaneously, phosphomonoester substrate (ROP) binds zinc ions and Arg166's guanidinium group. Transition to ii. → iii.: Ser102's deprotonated gamma oxygen acts as nucleophile, RO- departs. In iii. → iv.: hydroxide ion enters active site, coordinates with Zn1. It attacks phosphorus atom of prior phosphoserine via nucleophilic substitution, Ser102's gamma alkoxide leaves. Finally, iv. → i.: alcohol group and hydroxide ion regenerate on Ser102 and magnesium ion, yielding Pi ion.

3.2 Different proteins in MVs

In addition to ALP, other enzymes and proteins are highly involved in the mineralization process. For example, ectonucleotide pyrophosphatase/phosphodiesterase 1 (ENPP1), also named plasma cell membrane glycoprotein-1 (PC-1), is a membrane-bound glycoprotein that can hydrolyze extracellular nucleotides and phospholipids to produce Pi and PPi. As PPi acts as an efficient inhibitor of CaP mineralization [57, 58], the regulation of the Pi/PPi concentration ratio has great importance. In MVs, it is precisely controlled by sequential actions of enzymes: (i) NPP1 generates PPi and Pi (ii) ALP hydrolyzes PPi and ATP to Pi and (iii) phosphatase orphan 1 (PHOSPHO1) generates Pi from phosphocholine groups within MVs.

Ankylosis (ANK) protein is a multiple-pass transmembrane protein which transports PPi from the cytoplasm to the extracellular space. The ANK gene mutations in humans and mice resulted in disorders in mineral depositions in bone, joint fluid, cartilage and periarticular tissues [59-62]. In the studies of ANK mutations, significant changes in the level of PPi were found in intra- or extra-cellular areas [61, 63-66]. It indicates that ANK proteins regulate the PPi level in multiple tissues to suppress excessive mineralization.

Unlike other proteins presented above, annexins are ion channels piercing MVs in charge of transporting calcium ions. In matrix vesicles, three annexins were identified; annexin A2 [67], A5 [67, 68], and A6 [69].

3.3 Mechanism of mineralization

Matrix vesicle-mediated mineralization is an orchestrated series of ultrastructural and biochemical events that lead to crystal nucleation and growth (Figure 1.7A). Calcium ions start to accumulate around or inside MVs by concentrated acidic phospholipids such as phosphatidyl serine [70] and by annexin proteins [68]. At the same time, with collaborative works of enzymes, ALP, ENPP1 and ANK proteins, the final Pi is concentrated within and around MVs. The uptake of Pi is facilitated by phosphate ion transporters in the membrane of MV [71]. When the accumulation of calcium and phosphate ions within MVs reaches supersaturation, it leads to the nucleation of CaP minerals inside MVs (Figure 1.7B) [30, 46, 72]. While the precise mineral phases and transitions remain not completely understood, the initial phase seems to be an amorphous calcium phosphate (ACP) [73, 74].

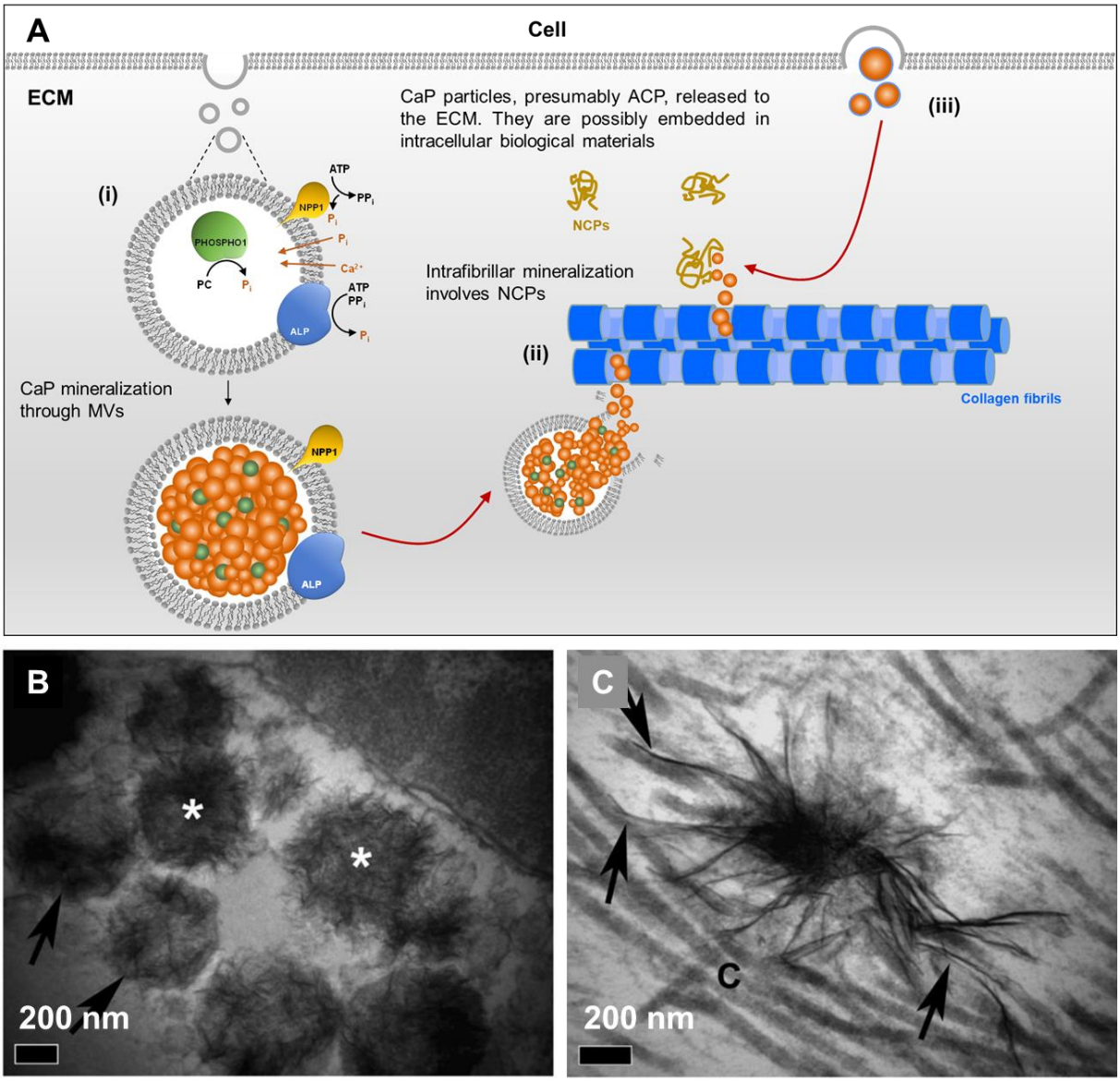

Figure 1. 7 MV-mediated mineralization. (A) Scheme of CaP mineralization in ECM [54] (i) MV-mediated mineralization by enzymatic control of phosphate ions and accumulation of Ca^{2+}, (ii) Intrafibrillar mineralization mediated by NCPs and (iii) release of ACP particles from the cytosol to ECM. (B, C) TEM images of intracellular MV-mediated mineralization in mouse osteoblast culture [74]. (B) CaP-containing vesicles located in ECM. Plate- or needle-like ribbons (shown with arrows) in CaP aggregate (*). (C) Mineral (arrows) propagation from CaP aggregates within the collagen matrix (C) in ECM.

4 Mineralization of collagen matrix

After the initiation of CaP mineralization in MVs, the propagation of mineralization is considered to attach to ECM and release minerals in the vicinity of the collagen matrix (Figure 1.7C) [46, 74]. According to the work by Marin *et al.*, the apatite minerals are sited intrafibrillar (58 %), interfibrillar (14 %) and in the gaps between collagens (28 %) in the bone of dogs [75].

This suggests that the mineral is present both within and around collagen fibrils. This question has been the subject of a vast literature, but the precise mechanism by which the mineral forms in the different locations remains not fully elucidated.

4.1 Intrafibrillar mineralization

Landis and coworkers provided evidence of nucleation of HAP within the gap of collagen fibrils through 3D tomographic TEM analysis. The proposed mineralization pathway is shown in Figure 1.8. According to the authors, the growth of the crystal is not limited to a single zone but it proceeds through unoccupied hole zones in neighboring molecules. The (001) planes of crystals remain parallel. If two crystals are located in adjacent zones, they apparently fuse to create a larger unit which leads to fused bands of mineral, irregular in c-axial length, along collagen hole zones and ultimately to thin parallel sheets of mineral throughout the assembly of fibrils [76]. Over the decades, different models have been proposed to understand intrafibrillar mineralization. The main aspects regarding these models will be described hereafter.

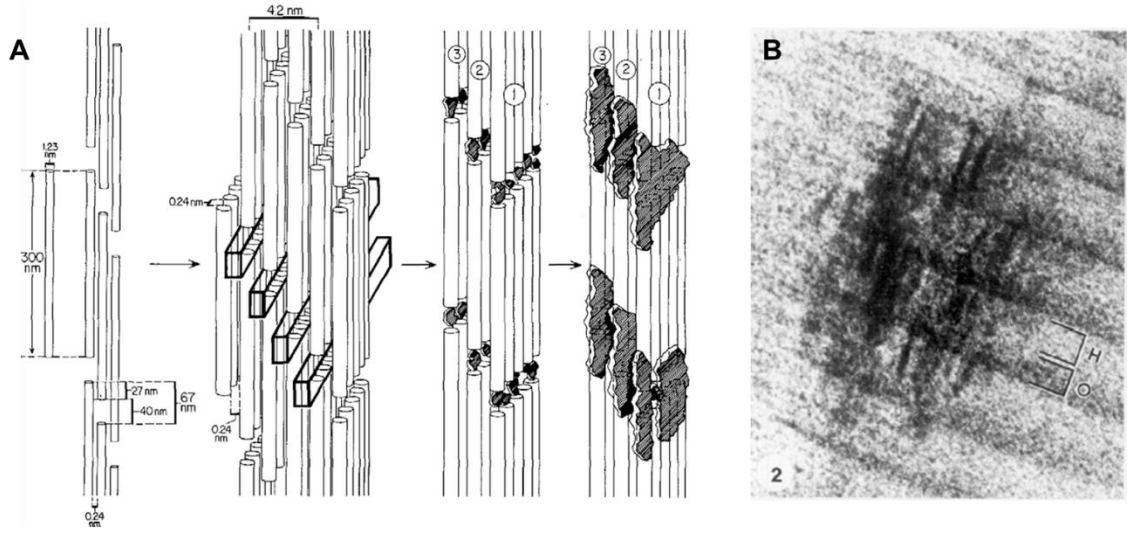

Figure 1. 8 Evidence of intrafibrillar mineralization [76]. (A) Scheme of mineralization of turkey tendon based on the observation using TEM and topographic reconstruction. The cylindrical rods, portraying tropocollagen units, consist of triple helical collagen molecules. Denser electron-rich mineral, appearing as striations within collagen fibrils. Crystals align with crystallographic c-axes parallel to molecular axes, (100) planes nearly parallel. Varied mineral deposits occupy voids, preferential growth in c-axis length along collagen's axis (B) TEM microscope of the early stage of mineralization in turkey tendon. The CaP minerals located in the collagen are oriented perpendicular to the collagen bands.

4.1.1 Collagen-directed intrafibrillar mineralization

The models explore the physical and chemical structures of collagen, suggesting that minerals are directly forming within or in the vicinity of collagen fibrils. In 2007, Toroian *et al.* proposed the mineral in bone is located primarily within type I collagen by replacing water within collagen to mineral. In this view, the authors proposed an important role of the physical structure of fibrils as a gatekeeper. Molecules smaller than 6 kDa protein can enter into fibrils and interact directly with crystals. [77]. In 2009, Landis and co-workers proposed that the specific sites with amino acid residues, glutamic acid, aspartic acid, lysine, arginine, hydroxylysine, and histidine, can be critical locations to serve as ion binding sites to lead subsequent nucleation in type I collagen [78]. Another study by Wang *et al*. showed that the precipitation of minerals occurs during the self-assembly of type I collagen fibrils [79].

Despite the relevant information provided by these hypotheses, the mechanism of intrafibrillar mineralization remains unclear. This is because intrafibrillar mineralization was not observed by simply immersing collagen in a supersaturated solution of ions [80]. It seems that it requires additional molecules, such as polymers, to stabilize ion complexes until they move into the fibrils and then nucleate.

4.1.2 Polymer-induced process

The intrafibrillar mineralization models based on non-classical nucleation theory are based on the use of polymers as stabilizers of nucleated clusters. Polymers, especially anionic polyelectrolytes such as polyaspartic acid (pAsp) and polyacrylic acid (PAA), are considered analogs of NCPs which have excessive anionic groups. Many researchers have indicated that the anionic polyelectrolytes can stabilize ACP precursors by capturing Ca^{2+} and mediating the nucleation and growth of minerals [81-83].

The polymer-induced liquid precursor (PILP) process was first proposed in 2000 for $CaCO_3$ by Gower and Odom [84]. The addition of pAsp formed some unusual morphologies of $CaCO_3$ as calcitic tablets, films and aggregates with helical protrusion. The helical protrusion was shown to be a metastable polymorph of $CaCO_3$. The direct observation of the crystallization using optical microscopy revealed the addition of pAsp-induced liquid-liquid phase separation of precursor droplets which deposit on the substrate and then solidify into calcite films.

The model was further applied to CaP mineralization [85]. The PILP process generates an amorphous liquid-phase mineral precursor, which facilitates intrafibrillar mineralization of

type I collagen because of the fluidic character of amorphous precursors. The precursors enter into collagens through the gap of fibrils by capillary action then solidify and mineralize followed by the loss of water to reach thermodynamically stable phases, HAP (Figure 1.9A).

In contrast to PILP, the polyelectrolyte-calcium complex-pre-precursor (PCCP) process generates a polyelectrolyte-Ca complex which infiltrates collagen fibrils followed by recruiting free Ca^{2+} and phosphate ions to form ACP within collagen fibrils (Figure 1.9B) [86].

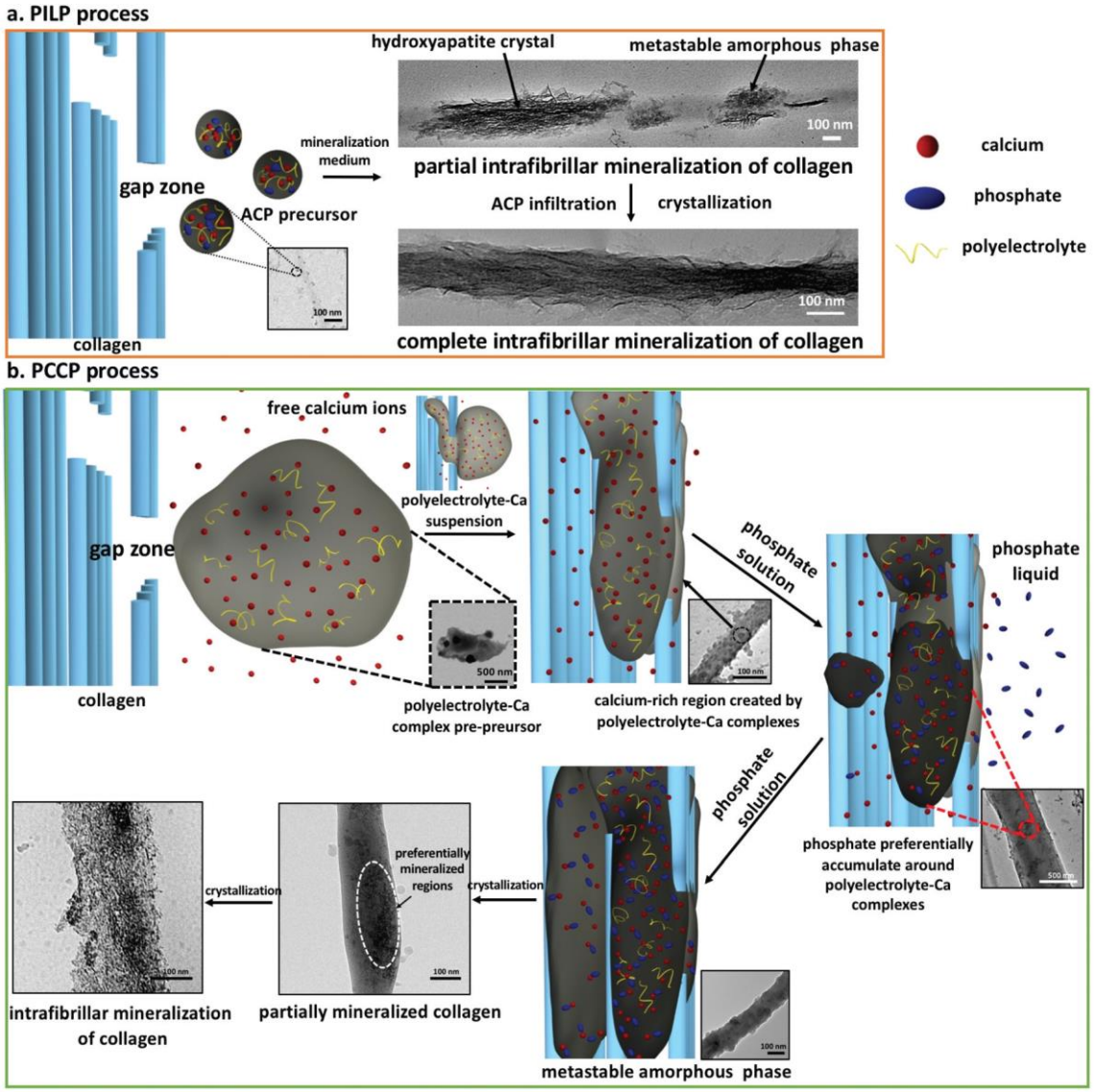

Figure 1. 9 Schematic illustration of (A) PILP and (B) PCCP process [86] (A) PILP process: involves polyelectrolyte-stabilized ACP precursors, infiltrating intrafibrillar interstice via gap zone, then gradually crystallizing. In the initial stage, partial and poor crystallization was observed. (B) PCCP process: involves polyelectrolyte–Ca complexes, infiltrating collagen fibrils along with free calcium ions and recruiting phosphate to form ACP within collagen and gradually crystallizing.

4.2 Extrafibrillar mineralization

Extrafibrillar mineralization is the form of mineralization that can be easily mimicked by simply exposing collagen fibrils to a supersaturated solution without adding NCPs or biological analogs (e.g., polymers) (Figure 1.10).

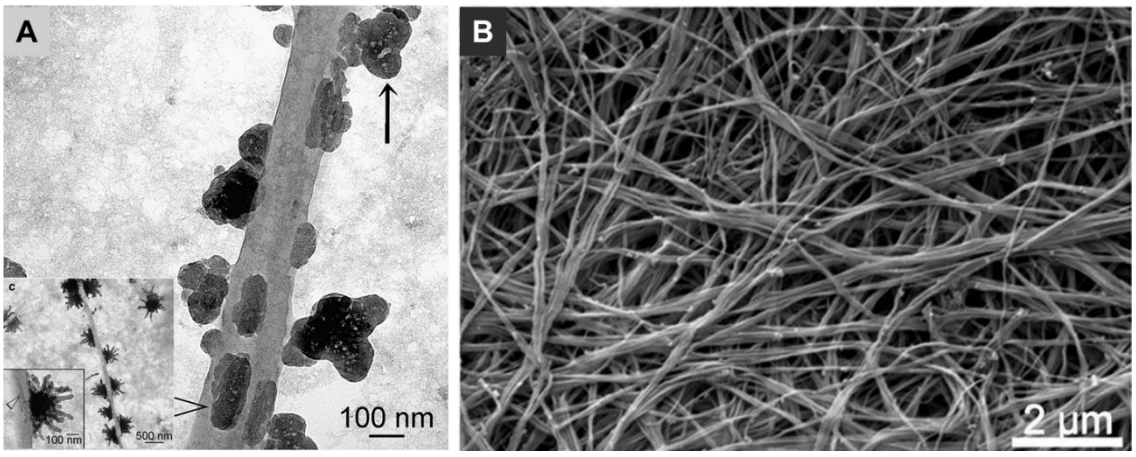

Figure 1. 10 Extrafibrillar mineralization (A) without additives (PAA as biomimetic analogs) [80] (B) interfibrillar mineralization in citrate functionalized collagens [87].

However, the scenario of extrafibrillar mineralization in vivo is not easy to explain, for instance, it is not known whether intra- and extra-fibrillar mineralization occur simultaneously. The extrafibrillar mineralization may contribute to the overall strength of mineralized tissues. The typical stress-strain curves between a mouse tendon and bovine bone femur show that the bone tissue exhibits a linear portion with a higher slope corresponding to that obtained on the tendon (Figure 1.11A) [88]. This indicates that the bone tissue is significantly more rigid than the tendon, owing to the presence of the mineral phase. Indeed, Nair and coworkers showed the contribution of mineralization to the mechanical properties by studying the relevance of intra- and extrafibrillar mineralization on Young's modulus (Figure 1.11B) [89]. The results show a decrease in the modulus when both extra- and intrafibrillar mineralization were reduced. The modulus of reduced intrafibrillar mineralization is 10 times lower than the wild type.

The mineralization of collagen matrix has been widely investigated in detail the process and the contribution to mechanical properties. However, there are still remaining questions on how

intra- and extrafibrillar mineralization occurs and how NCPs are involved in mineralization for example as an inhibitor or a guiding reagent for infiltration to the collagen fibrils.

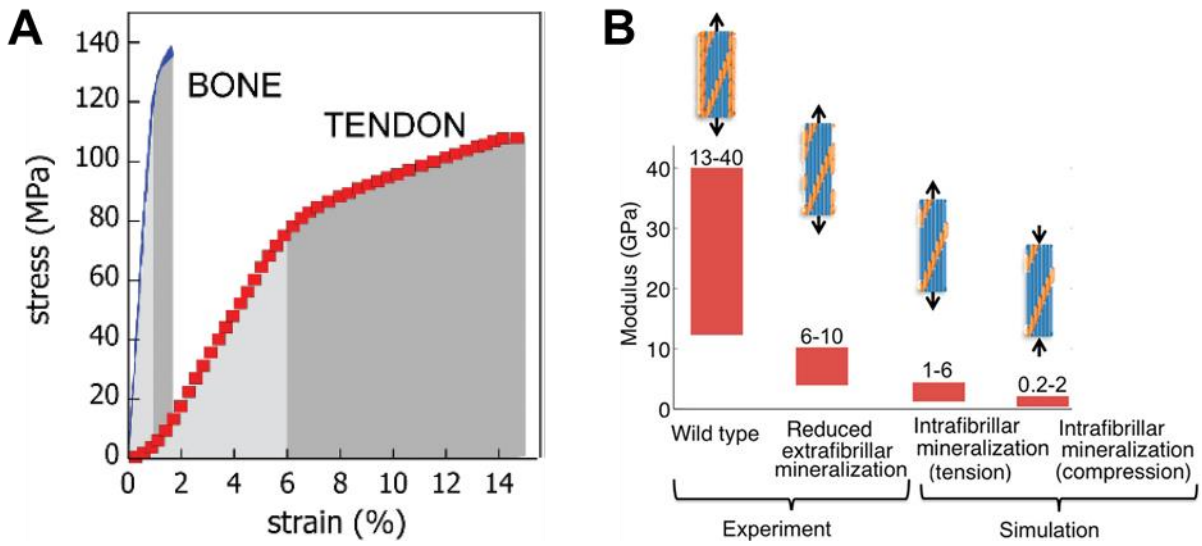

Figure 1. 11 Mechanical properties of mineralized tissues. (A) Typical stress-strain curves for mouse tail tendon and bovine bone femur [88]. The dark grey area corresponds to the energy per unit volume dissipated in the post-yield deformation. The light gray area indicates the elastic energy per unit volume during deformation. (B) Variation of Young's modulus for intra- and extrafibrillar mineralization [89]. The modulus for intrafibrillar mineralization was obtained by experiments using a wild-type mouse and a mouse model with hypophosphatemic rickets [90] while the modulus of intrafibrillar mineralization was based on simulations [89, 91].

5 Approaches for biomimetic mineralization

Through the mechanisms described above about MV-mediated mineralization and collagen matrix mineralization, two main biological features can be referred to: (i) homeostasis and (ii) compartmentalization. In the content of biomineralization, homeostasis refers to the balance and regulation of mineral deposition through the regulation of calcium and phosphate ion levels, especially by different enzymes and proteins. Compartmentalization is the spatial organization which allows a physical separation of a chemical environment such as MVs, which embed various biomolecules. These key features have motivated the development of systems mimicking the biological environment for a better understanding of the mineralization processes and designing functional materials.

5.1 Homeostasis: the regulations by enzymes and proteins

The pivotal roles of enzymes and proteins in the regulation of the nucleation and growth of minerals in space and in time have stimulated scientists to use them in experimental in vitro systems. In 2001, Urease, which catalyzes the hydrolysis of urea into carbon dioxide and ammonia, was introduced into CaP mineralization from urea-containing body fluid for control of the pH [92]. One of the main enzymes found in MVs, ALP, is used to generate phosphate ions as precursors in situ to induce CaP precipitation [93, 94]. Rauner and coworkers introduced ALP into polymer networks. The ALP hydrolyzed its substrate, glycerol phosphate, to generate Pi. It formed ACP nanostructure within polymer hydrogels homogeneously [95]. In the previous work of our group, enzyme-assisted mineralization was studied in a homogeneous phase. Calcium ions and orthophosphate precursors, α-glycerol phosphate, were mixed together in the presence of ALP. The comparison of systems with and without enzymes was investigated (Figure 1.12) [94]. One of the most important parameters to consider in the nucleation and growth of CaP minerals is supersaturation (σ) which is related to the concentration of calcium and phosphate ions in the solution [54]:

$$\sigma = \ln(\frac{IP}{K_{sp}})^{\frac{1}{v}}$$

IP: the ionic product. For HAP, $IP = a(\mathrm{Ca^{2+}})^5 \times a(\mathrm{PO_4^{3-}})^3 \times a(\mathrm{OH^-})$

K_{sp}: the solubility product

v: the number of growth unit

In the presence of excess Ca^{2+}, CaP mineralization without enzymes (depicted as chemical mineralization, *Chem*), starts when the total phosphate concentration (n(Pi)) is above the supersaturation (pointed as a blue arrow in Figure 1.12A, σ>0) which is already fixed in the experiments. As the system does not supply further Pi, the supersaturation drops over time and tends to reach σ=0. On the other hand, in an enzyme-assisted system, the n(Pi) increases as phosphate ions are generated from the substrate of enzymes (S) in situ. Therefore, σ starts to increase following the catalytic action of enzymes. When the Pi generation is over the critical value (blue arrow in Figure 1.12A), the nucleation can start. However, it continues to increase until the speed of Pi consumption through the mineralization process becomes larger than the enzymatic generation rate of Pi (red arrow pointing down). Based on the difference between the two approaches, we can expect that they undergo different mechanisms of CaP

mineralization. The preliminary work showed that the mineralization pathway involved different CaP intermediates whether *Chem* and enzyme-assisted procedures were used. However, this observation is difficult to decipher, owing to the interference of Mg^{2+} in the mineralization process. This issue will be profoundly investigated in the following chapter 2.

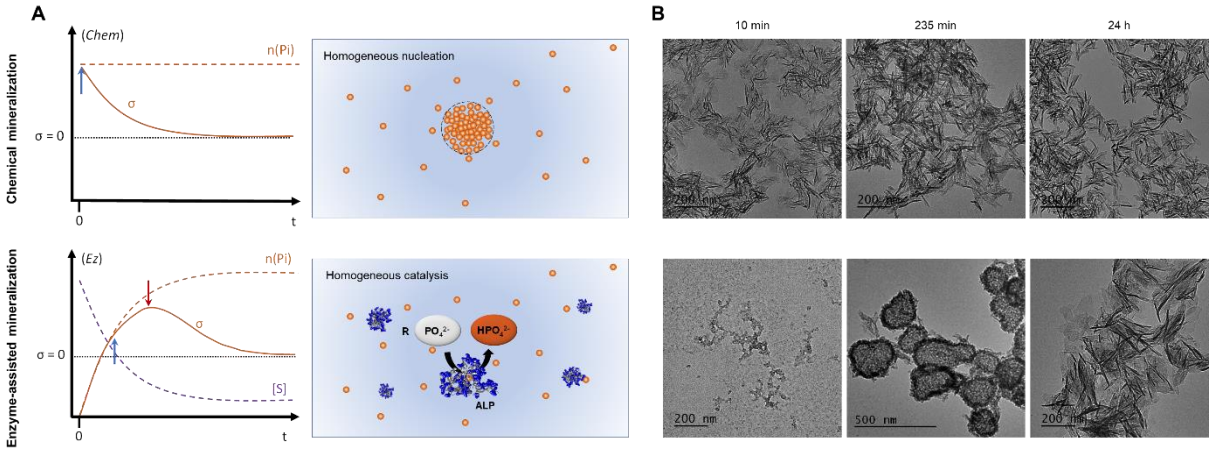

Figure 1. 12 Comparison between *chem* and enzyme-assisted CaP mineralization [94] (A) Illustration of supersaturation by time in the different systems; without(up, as Chem) and with enzymes (bottom). (B) comparison of two different systems with TEM micrographs.

5.2 Compartmentalization: heterogeneous catalysis

Compartmentalization is a key feature, which provides a suitable spatial chemical environment to control the mineralization process. It can be achieved by converting the homogeneous to a heterogeneous catalysis-based system, i.e. where the catalyst and reactants are in different phases. This is how biological systems explore MVs for the production of phosphates in the ECM. Such a system can be mimicked by immobilizing enzymes on a solid surface while introducing its substrate in mineralizing solutions. The immobilized enzymes have been defined as "enzymes physically confined or localized in certain defined regions of space with retention of their catalytic activities, and which can be used repeatedly and continuously" [96]. Since 1916, the immobilization of invertase was reported by Griffin and Nelson [97], the immobilization of various enzymes has been the subject of extensive research studies leading to the improvement of their properties including stability, specificity, activity or even inhibition by reaction products.

In the context of biomineralization, for several decades, different methods to immobilize ALP

have been developed on different substrates via cross-linking, covalent, and physical adsorption. Chemical crosslinking is based on covalent bonds between molecules and enzymes but with the use of crosslinking reagents such as N-(3-dimethylaminopropyl)-N′-ethylcarbodiimide hydrochloride (EDC). Osathanon and co-workers immobilized ALP on a fibrin scaffold using EDC followed by mineral deposition within the scaffold [98]. This method was also used to immobilize ALP on the alumina surface, showing successful initiation of CaP mineralization on the surface [99]. Ferrairs *et al.* used another chemical method, which consists of the ALP grafting via tresyl chloride activation on the surface of Ti alloys. It preserved the catalytic activity of ALP, resulting in the formation of calcium-rich HAP on a bioactive surface after 15 days [100]. Jonge *et al.* used the electro-spraying method to introduce ALP on a Ti surface to induce surface mineralization via a local increase of phosphate anions by hydrolysis of organic phosphate monoesters. The mineral was observed on the surface after 3 days of incubation [101]. Andrade *et al*. immobilized ALP into Langmuir-Blodgett films on a titanium substrate. The surface was exposed to synthetic cartilage lymph solution, containing different components including Ca ions and ATP, one of the substrates for ALP, resulting in the growth of CaP [102]. Furthermore, the direct incorporation of ALP into different hydrogels (chitosan, collagen, or synthetic polymers) and porous scaffolds were reported with successful mineralization by diffusion of calcium ions and substrate of the enzymes within the gel [95, 103-109].

Beyond the individual role of ALP as catalysis regulating the level of phosphate ions, their interaction with collagen and further mineralization on collagen matrix also caught the eye of scientists. In 1992, Beertsen and his coworker immobilized ALP covalently to slice guanidine-extracted demineralized bovine dentin (DDS) to determine whether ALP causes mineralization of collagenous matrix [110]. ALP-coupled DDS showed extensive mineralization after 4 weeks of incubation with a similar amount found in normal bovine dentin (~ 80% of HAP per microgram of hydroxyproline). In 2004, Yamauchi and coworkers built alternative multilayers of Col and CaP which were mineralized by means of the catalytic activity of ALP. The mineralized layer adds interesting mechanical properties but also supports the attachment and growth of fibroblast cells [111]. Later, Bosco and co-workers immobilized both collagen and ALP on Ti surfaces by an electro-spraying method and showed that collagen improves the retention of ALP through protein-protein interaction which improves the surface mineralization [112].

As shown above, the incorporation of enzymes and proteins is a promising strategy to regulate mineralization. The immobilization provides the possibility to initiate the mineralization at the solid-liquid interface rather than in the bulk solution.

As a preliminary work, the ALP was immobilized on a self-assembled monolayer on a gold flat surface to assess the enzyme-assisted mineralization in a heterogeneous phase (Figure 1.13). For this purpose, a gold-coated surface is functionalized with thiols with carboxylic end-groups and the ALP was grafted via EDC/NHS crosslinking. The surface was immersed in a mineralizing solution containing glycerol phosphate, as a substrate of the ALP, and calcium ions (pH 8.6, 37 °C) for 24 hours. According to infrared analysis, it showed that the surface was mineralized with the action of enzymes, which preserved a weak catalytic activity. However, the surface morphology studied by AFM showed that the minerals were specifically located at the edge of Au grains rather than distributed homogeneously on the overall surface (Figure 1.13 B and C). The amount of minerals and their organization on the surface were not sufficient for further characterization.

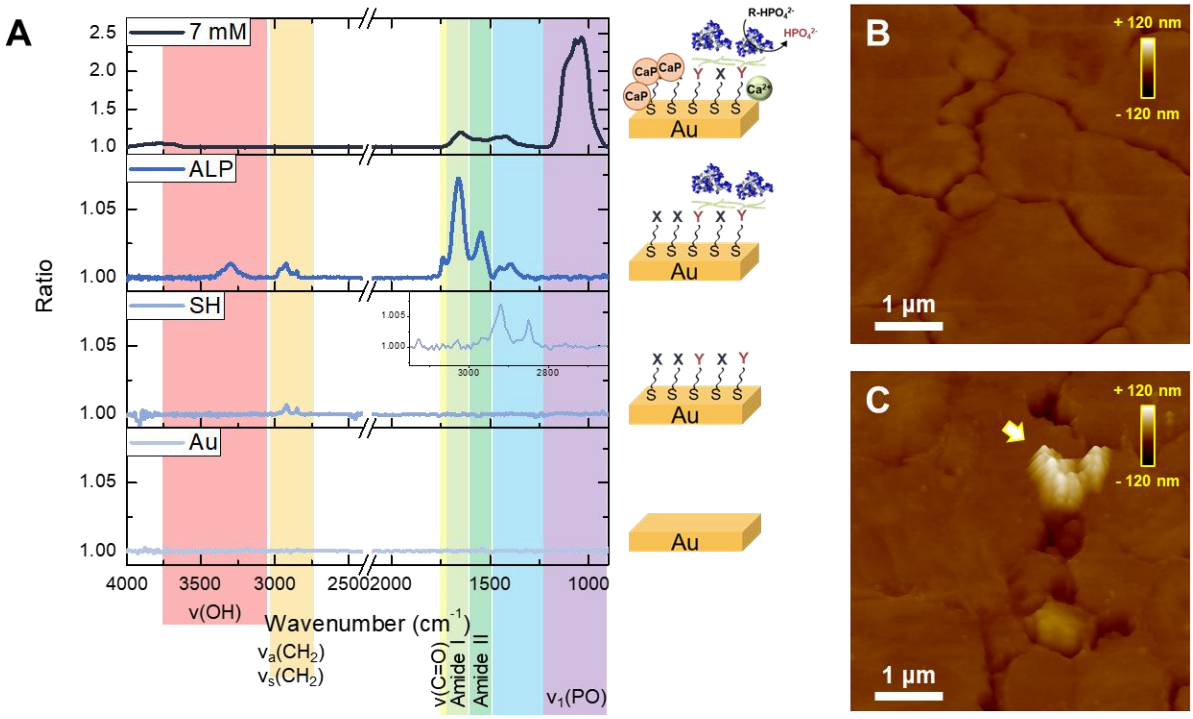

Figure 1. 13 Enzyme-assisted mineralization on a gold surface. (A) Infrared analysis from clean Au surface (bottom) to surface functionalization with self-assembled monolayer with thiols, cross-linkage with ALP and CaP mineralization (top). AFM height images on clean (B) and mineralized Au surface (C). The mineral is marked with an arrow.

These findings suggest that immobilization of ALP in a monolayer-like structure is not a suitable configuration to perform mineralization. Instead, there is a need for a “reservoir” of enzymes located at the solid-liquid interface. For this purpose, a more suitable surface functionalization technique is thus considered as the sequential layer-by-layer (LbL) method.

6 Layer-by-Layer (LbL) assembly

6.1 Principle

The concept of LbL has emerged from 1966 by Iler who built alternative layers of differently charged colloidal particles on glass [113]. After numerous technological iterations, it was (re)discovered by Decher in 1997 [114]. Based on the concept, the conventional LbL assembly protocols have become well-established and very common in many laboratories [115]. LbL is a method to generate thin films by alternative and repetitive exposure of a given support to charged species with spontaneous adsorption of an oppositely charged material. Between each exposure, the substrate is washed to remove the access of charged species. A cycle of exposures constitutes a single bilayer with a thickness in a range of nanometers. The repetition can be conducted to build multilayers until it yields the desired thickness [114]. The simplicity, versatility and nanoscale control of LbL assemblies provide the method as one of the most widely used technologies for coating on any type of substrate (planar, polar, particles, *etc*.) with a diverse range of building blocks on the layer such as polymers, nanoparticles, proteins and lipids [115]. Generally, it is performed by immersing substrate into solutions but it is expanded to different methods such as spin coating, spraying or fluidics (Figure 1.14B). Moreover, the entire process can be performed in mild conditions, for example in aqueous solutions, at room temperature without the addition of harmful solvents or extreme pH values, which give high benefits to deal biomolecules to preserve their own structure and bioactivity.

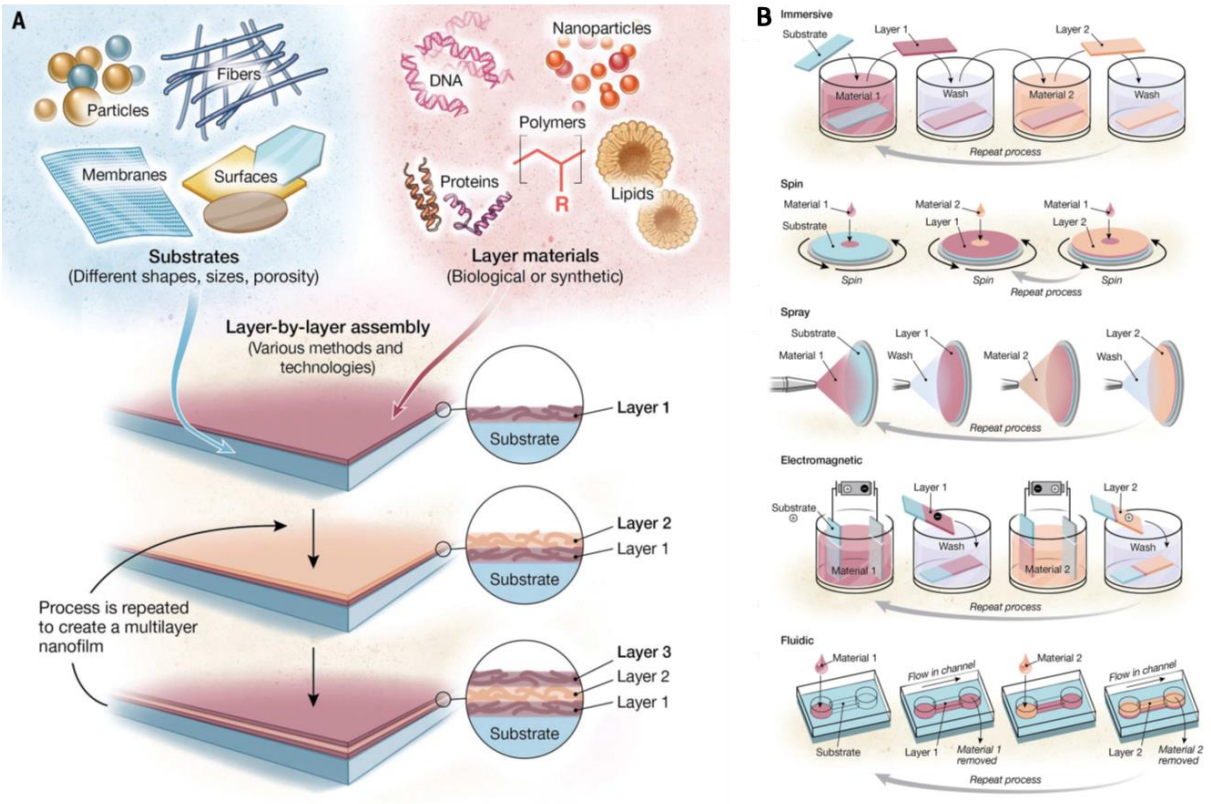

Figure 1. 14 Layer-by-Layer method [116]. (A) Overview of LbL assembly. (B) five major techniques to conduct LbL: Immersive, spin, spray, electromagnetic, and fluidic methods.

6.2 Molecular interactions

Electrostatic interaction

In LbL assembly, electrostatic interactions between oppositely charged molecules are generally dominating [114, 117]. In early studies, the interaction was considered a main driving force. It suggested that polyelectrolytes require a minimum charge density for successful build-ups of multilayers [118, 119]. In this regard, the polyelectrolytes with low charge density resulted in weak stability of multilayers, sometimes leading to the desorption of layers. However, it was reconsidered as some polymers with unexpectedly low charge density were successfully incorporated in multilayers by the LbL method [120, 121]. It demonstrated that the build-up of multilayers through the LbL method is not only restricted to the electrostatic interaction but may involve different interactions: hydrogen bonding, charge transfer, biologically specific interaction (Figure 1.15) [122].

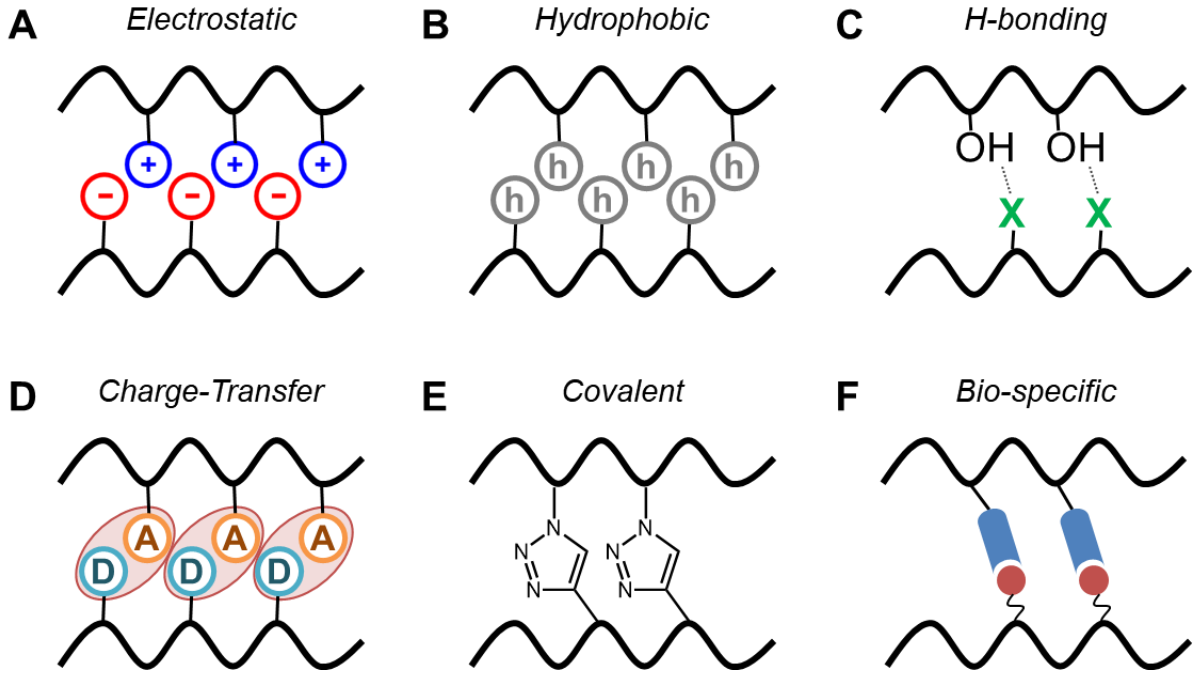

Figure 1. 15 Molecular interactions in LbL assembly. (A) Electrostatic interaction: the basic interaction between charged molecules (B) Hydrophobic interaction: interaction between molecules either charged or uncharged. (C) H-bonding: attractive forces between molecules with hydrogen atoms bonded to electronegative atoms (indicated as X, typically nitrogen, oxygen or fluorine) (D) Charge-transfer (CT): the interaction between electron donor and acceptor (E) Covalent bond: strong chemical bonds between polyelectrolytes in multilayers (F) Biological specific interactions: strong binding based on specific interaction between biomolecules such as avidin-biotin, lectin-carbohydrate and antibody-antigen.

Hydrogen bonding

Hydrogen bonding is also one of the most studied driving forces for building multilayers using the LbL method. LbL assemblies based on hydrogen bonding were first studied using polyaniline and a variety of polymers such as poly(vinylpyrrolidone), poly(vinyl alcohol), poly(acrylamide), and poly(ethylene oxide) [123]. Wang and coworkers showed hydrogen-bonded LbL assemblies through alternate deposition of poly(4-vinyl pyridine) as hydrogen bonding accepter with poly(acrylic acid) (PAA) as hydrogen bonding doner [124-126]. The multilayers with hydrogen bonding were sensitive to the environment and easily broken by external stress such as pH, ionic strength, temperature or electric fields [127-129]. So, the stability of multilayers was improved by some crosslinking approaches [130, 131]. On the other hand, it is used as a stimulus for further applications for example the construction of degradable capsules [132-134] and the development of reversible systems [135].

Hydrophobic interaction

The hydrophobic interaction is considered another driving interaction of building multilayers. Serizawa and co-workers showed the fabrication of thin films of poly(vinylamine) or type I collagen on quartz crystal coated with silver or gold by repetition of exposure of the substrate to polyelectrolyte solution, washing and drying [136, 137]. It showed the formation of the multilayers of a single polyelectrolyte through hydrophobic interactions. The interaction is mostly studied when the molecules and substrates are hydrophobic [138-141] but also extended to the multilayers including proteins. It revealed the interactions between the surface-polyelectrolytes and polyelectrolytes-proteins in multilayers are not only electrostatic interactions but also hydrophobic interactions [142].

Covalent bonding

Covalent bonding is also a driving force to assemble multilayers using LbL techniques. It contributes to the stability and strength of the multilayers. The first covalent bond driven multilayers were built with the use of functionalized dendrimers and maleic anhydride [143]. The synthesis was carried out by an alternating deposition and crosslinking reaction leading to the covalent assembly of multilayers. The covalent bonding-based multilayers were constructed by various chemical reactions: crosslinking [143], alternating co-polymerization [144], hydrolysis [144], EDC activation [145, 146], and click-chemistry [147, 148]. Based on the use of different chemistry, the covalent bonding LbL assemblies were applied to construct 3D structures such as hollow capsules in organic solvents [149], to conjugate polymer and nanoparticles [150] and to build organic-inorganic hybrid materials [151]. The multilayers based on covalent bonding are generally highly stable, robust and capable of functionalizing with other materials.

Charge-transfer (CT) interactions

The CT interaction-based multilayer films were suggested by Shimazaki and co-workers by building up the multilayers using the electron donor and acceptor polymers [152-156]. The films have periodic layers of CT complexes as shown in Figure 1.15D which can provide unique physical properties which are not expected from the homogeneously dispersed complexes [122].

6.3 Factors influencing LbL assembly

Overall, the LbL method mainly based on electrostatic interactions is considered a simple, versatile and reproducible method. However, the construction of multilayers is influenced by

various parameters, including the nature of polyelectrolytes (weak/strong polyelectrolyte, molecular weight and charge density) and parameters related to the medium (pH, ionic strength and temperature). The successful build-up of multilayers can be achieved by a careful selection of the parameters.

pH

The influence of pH on the LbL assemblies has been widely investigated. The multilayers containing weak electrolytes such as PAA, poly(allyl amine hydrochloride) (PAH) and poly(styrene sulfonate) (PSS) were highly influenced by modulating the pH of the solution. The simple adjustments of pH (ranging from 2.5 to 9.0) of the dipping solution influenced the thickness and the growth mechanisms of multilayers [157, 158]. When the pH of PAH and PAA solution varied from 3.5 to 7.5, the thickness of multilayers changed from very thin (< 10 Å) to thicker (> 120 Å) bilayers or even halted the growth of multilayers (Figure 1.16A) [157].

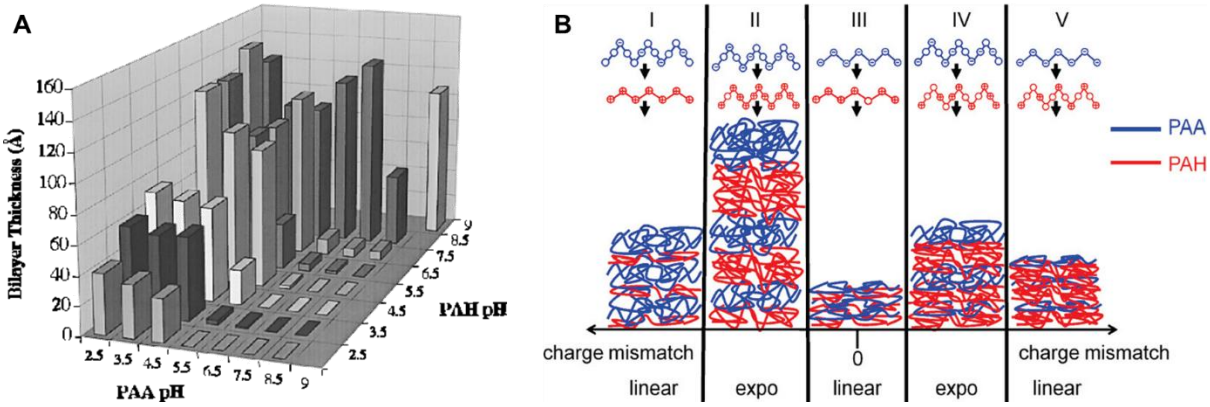

Figure 1. 16 pH effect on PAH/PAA multilayers. (A) pH matrix showing the average increase of thickness of bilayers as a function of pH in solutions [157]. (B) Growth behavior in dependence on charge mismatch [158]

The dependence of charge density of polyelectrolytes at different pH was investigated by QCMD and ellipsometry. It suggested five distinct regimes with different growth mechanisms [158].

(I) In this regime, the pH region is from 3.5 to 4.5. At this pH range, the weak base PAH is almost fully charged as the pKa of PAH is 8~9, while the weak acid PAA is partially charged. The increase of pH in this regime induces the further charging of PAA and the discharge of PAH which results in a transition toward a more symmetric layer growth.

The multilayer becomes more rigid with the higher density of electrostatic interactions. In this region, the growth of multilayer is linear where the overall absorbed mass and film thickness increase constantly at each polyelectrolyte adlayer.

(II) In the second regime, the pH is from 4.5 to 6 which forms soft and thick films as both PAA and PAH are absorbed in large amounts. In this region, the mass per layer reaches a maximum for both polyelectrolytes and the build-up becomes more symmetric. As mentioned for regime I, it can be expected that the increase of pH reduces the charge density of PAA resulting in less adsorption of polyelectrolytes for charge compensation. However, QCM-D analysis indicates a new growth mechanism, where the increases of the thickness of the layers and the deposited mass follow an exponential growth. This is attributed to an interdiffusion of the polymer chains within the multilayered film [159].

(III) In the third regime, pH from 6.5 to 7.5, the total adsorbed mass and the layer thickness have the lowest values. In this range, the polyelectrolytes are almost fully charged and behave like strong polyelectrolytes, thus restricting the interdiffusion. In this regime, multilayers are formed based on linear growth as commonly observed for strong polyelectrolytes.

(IV) In the fourth regime ranging from pH 8 to 10, the polyelectrolyte charge density is similar to regime II. PAA is nearly fully charged in contrast to PAH which becomes less charged with increasing the pH to be close or exceeding its pKa. Therefore, in this region, the multilayer growth relies on exponential growth, which is supported by the results obtained by QCM-D [159].

(V) The last regime is from pH 10 to 12. It shows similarity with the first regime. The asymmetric charge densities (almost fully charged PAA, partially charged PAH) result in asymmetric multilayer formation following linear growth.

In summary, the pH of the polyelectrolyte solutions not only affects the thickness of the multilayers but can also change their growth mechanism.

Temperature

The temperature can change the thickness, the internal structure and growth mechanism of multilayers. Tan and co-workers investigated fabrication of poly(diallyldimethylammonium chloride) (PDDA)/poly(styrene sulfonate) (PSS) multilayers varying the temperature from 10

to 70 °C. They observed that the LbL assembly performed at high temperatures generates thicker multilayers than at lower temperatures, owing to the swelling of the films and the enhancement of the interpenetration process [160]. Salomäki and co-workers expanded the study to build two kinds of multilayers (PSS/PDDA and PSS/PAH) in different temperatures. They found that the temperature changed not only the film thickness but also the growth mechanism from linear growth at low temperatures to the exponential growth regime at higher temperatures.

Ionic strength

Ionic strength and counterion species can also influence the stability, permeability, internal structure, and growth mechanism as the LbL method is mainly based on the electrostatic interactions between polyelectrolytes. Dubas and Schlenoff studied the growth of PSS/PDDA, PAA/PDDA and PSS/PAH at different salt (sodium chloride) concentrations [161, 162]. When the ionic strength was getting higher, the thickness of multilayers was increased until a critical concentration of the salt (~ 0.4 M, Figure 1.17A).

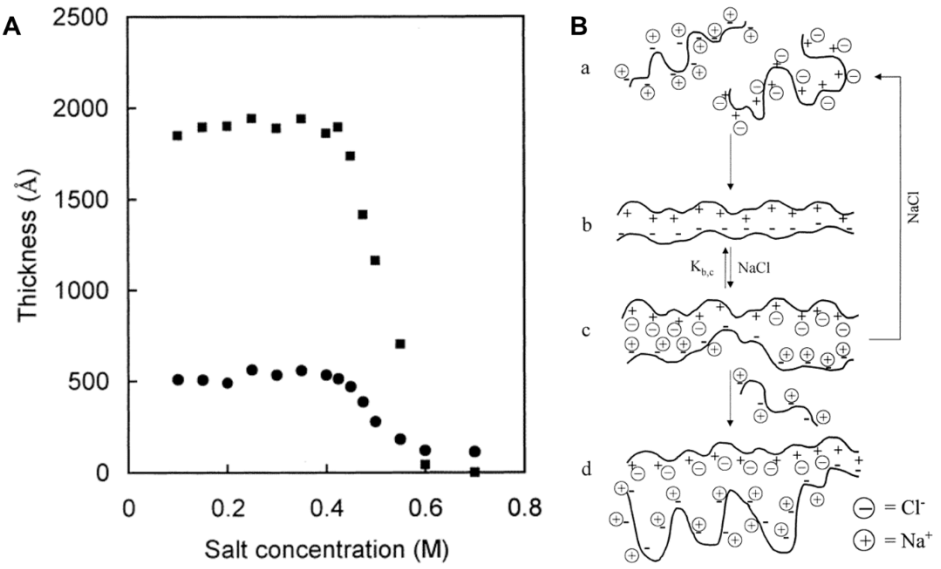

Figure 1. 17 Ionic strength and multilayers [162] (A) Thickness of 10-bilayers of PAA (molecular weight 84.5k (●) and 5.2k (■)) and PDDA as a function of salt concentration. (B) Different steps during the formation, swelling and decomposition of LbL assembly. (a) Compensation of the charge on polyelectrolytes by counterions in solutions inducing the polymer association on multilayers. (b) Electrostatic interaction between polyelectrolytes in multilayers. (c) Additional salts (⊕ or ⊖) induce some swelling. The loose multilayers or the decomposition of multilayers (shown with an arrow between c and d) with sufficient swelling. (d) Charge overcompensation near the surface in the presence of excess polyelectrolyte (here negative). The simultaneous steps b → c → d occur during the adsorption of polyelectrolyte layers.

The swelling of multilayers by salts indicated that it is reversible when there is no decomposition of multilayers (Figure 1.17B) [161]. However, after a certain concentration, multilayers were decomposed as the polyelectrolytes competing with the external salt ions. The salts in solution moderate electrostatic interactions between charged polyelectrolyte segments through a screening charge process.

The salt concentration influences many parameters regarding the polyelectrolyte chains: interpenetration, conformation, and their electrostatic interactions. Zhang and coworkers also observed the thicker multilayers with chain interpenetrations when the higher salt concentration [163]. Moreover, the authors showed that the multilayer growth was governed by each chain conformation or interpenetration of polyelectrolytes at low ([NaCl] < 1.0 M) or high ([NaCl] < 1.0 M) salt concentrations [164].

The ionic strength not only changes the thickness or the swelling of multilayers but also the structure of the LbL assembly. For example, the formation of porous multilayers was reported by varying the salt concentration [165, 166]. It reveals that ionic strength can control the permeability of the assembly. Moreover, the increase in salt concentration induces the formation of coiled conformation of polyelectrolytes resulting in the increase of the thickness and the roughness of the LbL assembly [167, 168].

The type of additional counterions also influences the build-up of multilayers. The use of specific counterions (F^-, Cl^-, Br^-, NO_3^-, ClO_4^-, SO_4^{2-}) changes the growth regime of multilayers with an increase of the film thickness and swelling as they can bind to positively charged polyelectrolytes [169-171].

Molecular weight

Molecular weight also affects the growth, internal structure and morphology of multilayers. The understanding of the role of polymer molecular weight is of great relevance to further design and develop advanced functional controlled release systems. Dubas and Schlenoff also showed that lower molecular weight was more sensitive to the changes of pH building thicker multilayers [162]. Other studies supported that molecular weight impacts the thickness of multilayers via interdiffusion of polyelectrolytes [172, 173] and different growth mechanisms such as growth inhibition [174, 175] or exponential growth [176].

Charge density

As LbL assembly is mostly based on electrostatic interactions, charge density on polyelectrolytes is also an important parameter. Mermut and Barrett reported that the weakly charged polyelectrolytes were more sensitive to environments such as pH, salt concentration and counterion species [177]. Koetse and coworkers reported the increase in thickness when the charge density was decreased [178]. Some researchers suggested the critical charge density (between 50 and 75 %) [179-181]. Below the critical values, the multilayers grew very slightly or even stopped the build-up. However, it was also observed the growth of multilayer assemblies at lower charge density (~ 8 %) which highlights the importance of non-electrostatic interactions such as hydrophobic interaction [121].

6.4 LbL assembly with Col

The immobilization of protein at interfaces has been the subject of extensive studies for applications such as the development of biomaterials, biosensors and control of catalytic activity [182, 183]. In this context, the LbL assembly was also applied to bring proteins to the interfaces and embed them within multilayers. This is because proteins may include amino acids with ionizable groups (e.g., Lys, His, Arg, Asp, Tyr, and Glu). However, proteins are polyampholytes with low conformational entropy and heterogeneous charge distribution [184] while polyelectrolytes have homogeneous charge distribution and conformation. Therefore, it is necessary to have careful choices of pH, ionic strength and the counter polyelectrolyte to achieve successful growth of multilayers and avoid the lack of charge compensation of protein layers or the repulsion between polyelectrolytes and proteins. In addition, the incorporation of proteins within multilayers may induce their unfolding upon the interaction with polyelectrolytes resulting in the loss of their structure and the bioactivity [185-188]. In this aspect, the target protein should be analyzed to determine its isoelectric point (iep) which provides the overall net charge of proteins in different conditions. The iep can be computed based on its amino acid composition and determined by performing electrophoretic mobility measurements at different pH. This is particularly easy for many globular proteins.

By contrast, determining the ep of type I collagen is a challenge, owing to its anisotropic structure (see section *1.2.1*). This explains the divergent experimental values of iep ~6.0 [189] or 9.3 [190]. These values indicate that the incorporation of Col in multilayers can be achieved in an acidic media. This is supported by many studies [191-193]. Moreover, it showed that the

growth of multilayers Col/ polyanion and poly(ethylenimine) (PEI) was not possible at pH ~8.3 [191].

The LbL assemblies using Col as a polycation have been studied not only with synthetic polymers such as PSS [194] or PAA [195] but also biopolymers such as hyaluronic acid (HA) [196], heparin (Hep) [197, 198] and tannic acid (TA) [199, 200].

Col/HA multilayers

The first LbL assembly with Col and HA was built on glass slides [196]. The results show the successful build-up of $(PEI)(HA/Col)_n$ multilayers up to 120 bilayers (13.6 μm in thickness) following a linear growth regime (Figure 1.18A). The obtained multilayers showed the formation of well-defined collagen fibrils, suggesting their possible self-assembly within the multilayers (Figure 1.18B). The study also includes the adhesion of chondrosarcoma cells on collagen layers which can produce a biomimetic environment of ECM.

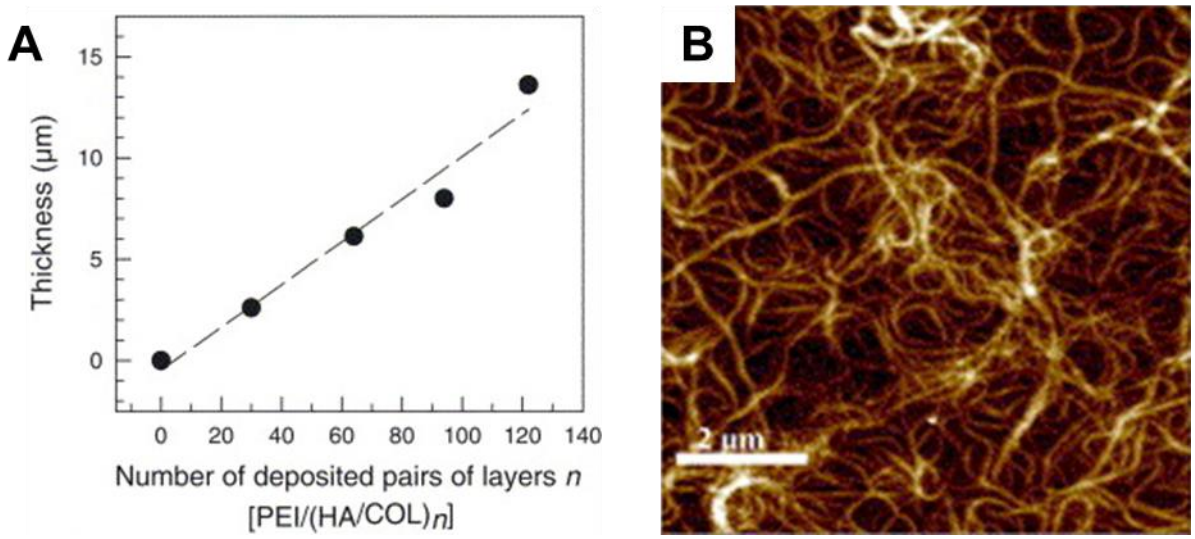

Figure 1. 18 Multilayers with Col and HA [196] (A) Thickness evolution from confocal microscopy section. The data is fitted with a linear relation with r^2 as 0.96. (B) AFM heigh image of 122 bilayers of PEI/(HA/Col). Z scale from 0 up to 50 nm.

The construction of multilayers with collagen can be achieved in acidic media pH of around 4. However, when the multilayers moved into physiological pH, drastic dissolution of multilayers was observed by deprotonation of carboxylic groups in HA [201]. The enhancement of stability and durability was achieved by further chemical crosslinking using EDC and NHS [201].

Col/Hep multilayers

The LbL assemblies with Col were also built with the use of Hep as a polycation. The high charge density of Hep induced the exponential growth of multilayers with interdiffusion of polyelectrolytes through multilayers resulting thick multilayers [197]. Interestingly, the growth of five bilayers of Col/Hep didn't show a significant increase in the diameter of fibrils. Chen and coworkers built Hep/Col multilayers on a titanium substrate of up to 15 bilayers [198]. The multilayer showed enhanced hemocompatibility with the advantage of the anticoagulant property of Hep. However, a fast degradation was observed at physiological saline conditions by deprotonation of amine groups on Col.

Col/TA multilayers

A natural polyphenol, tannic acid (TA), was used to build (TA/Col) multilayers by the dipping method in buffers at pH 4 [199]. Unlike the other cases, tannic acid interacts with collagen through hydrogen bonding (Figure 1.19A) [200] which can give high stability to the multilayers.

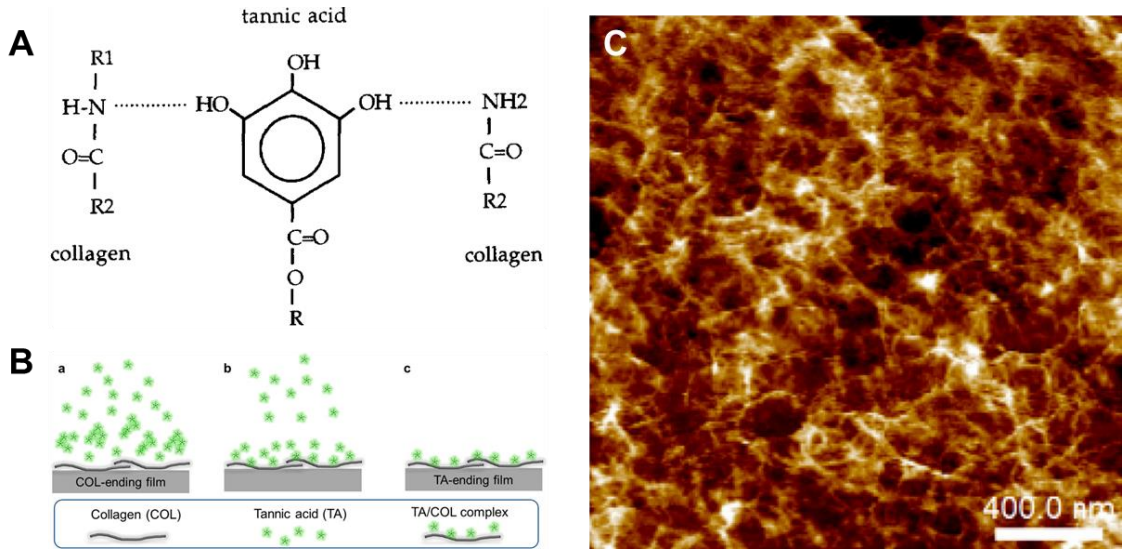

Figure 1. 19 Multilayers with Col and TA in acetate buffer pH 4. (A) Possible hydrogen bonds between Col and TA [200]. (B) Build-up of (Col/TA) multilayers [199]. (a) Col exposed to TA solution, (b) TA binds to Col and (c) rinsing steps remove excess TA. (C) AFM image of $(Col/TA)_2$ in liquid (z-scale: 50 nm) [199].

A recent study has revealed that the use of different buffers impacts the physicochemical and antibacterial properties of Col/TA multilayers [199]. In acetate buffer, the TA molecule binds to Col generating TA complexes without structural changes of Col. It resulted in a fibrillar

organization of Col as shown in Figure 1.19C. However, the use of citrate buffer at pH 4 caused a different fate on collagen structure (Figure 1.20). When Col was exposed to TA solution in citrate buffer, it desorbed from the surface to form Col-TA aggregates. The precipitation of the aggregates led to the granular topography of Col/TA films (Figure 1.20B).

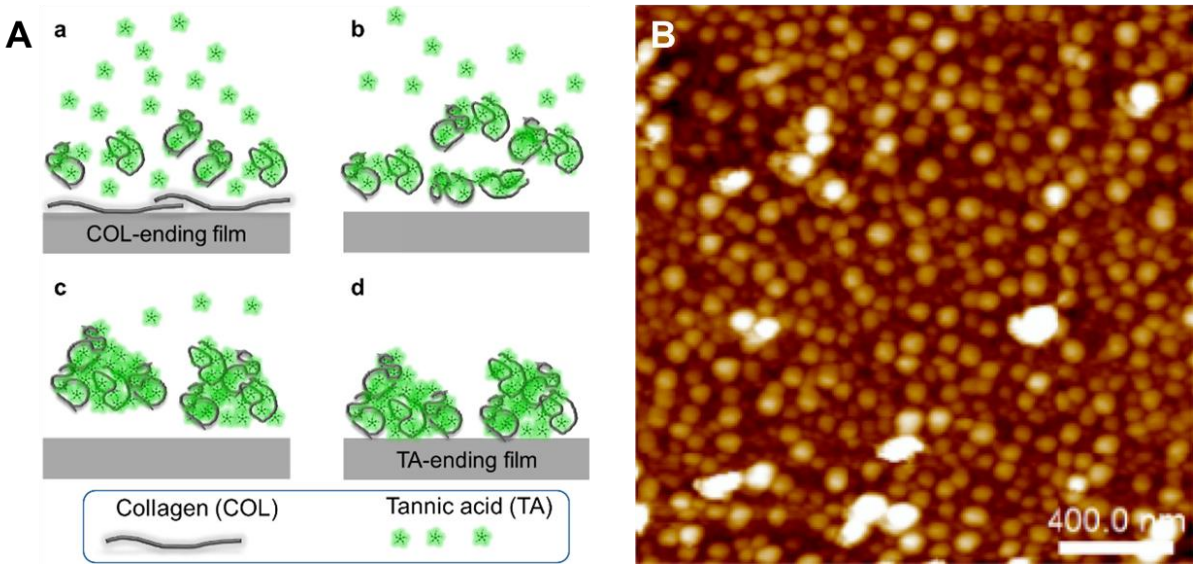

Figure 1. 20 Multilayers with Col and TA in citrate buffer pH 4 [199]. (A) Build-up of (Col/TA) multilayers. When TA was in contact with Col, (a) desorption of Col to form Col/TA complexes, (b) dimerization, and (c) aggregation, and (d) preparation of aggregations on the surface. (B) AFM image of $(Col/TA)_2$ in liquid (z-scale: 50 nm).

This PhD work aims to indicate the physiological characteristics of biomineralization: homeostasis and compartmentalization. In the aspect of realizing homeostasis, enzyme-assisted mineralization with the use of ALP is expanded to the control of CaP mineralization through the modulation of catalytic activity and the introduction of an influential factor of CaP mineralization. For a more advanced biomimetic system in terms of compartmentalization, the collagen fibrils are incorporated in the vicinity of enzyme-assisted mineralization in the heterogeneous phase. To establish the system, LbL assembly was adapted to build multilayers containing two different proteins.

7 References

1. Boskey, A.L. and P.G. Robey, *The Composition of Bone*, in *Primer on the Metabolic Bone Diseases and Disorders of Mineral Metabolism*. 2018. p. 84-92.
2. Wang, X., et al., *Topological design and additive manufacturing of porous metals for bone scaffolds and orthopaedic implants: A review.* Biomaterials, 2016. **83**: p. 127-141.
3. Wegst, U.G.K., et al., *Bioinspired structural materials.* Nature Materials, 2015. **14**(1): p. 23-36.
4. Eriksen, E.F., *Cellular mechanisms of bone remodeling.* Reviews in Endocrine and Metabolic Disorders, 2010. **11**(4): p. 219-227.
5. Florencio-Silva, R., et al., *Biology of Bone Tissue: Structure, Function, and Factors That Influence Bone Cells.* BioMed Research International, 2015. **2015**: p. 421746.
6. Feher, J., *9.8 - Calcium and Phosphorus Homeostasis II: Target Tissues and Integrated Control*, in *Quantitative Human Physiology (Second Edition)*, J. Feher, Editor. 2017, Academic Press: Boston. p. 933-945.
7. Behzadi, S., et al., *Nanomedicine for safe healing of bone trauma: Opportunities and challenges.* Biomaterials, 2017. **146**: p. 168-182.
8. Beniash, E., *Biominerals—hierarchical nanocomposites: the example of bone.* WIREs Nanomedicine and Nanobiotechnology, 2011. **3**(1): p. 47-69.
9. Frantz, C., K.M. Stewart, and V.M. Weaver, *The extracellular matrix at a glance.* Journal of Cell Science, 2010. **123**(24): p. 4195-4200.
10. Ricard-Blum, S., *The collagen family.* Cold Spring Harbor perspectives in biology, 2011. **3**(1): p. a004978.
11. Shoulders, M.D. and R.T. Raines, *Collagen Structure and Stability.* Annual Review of Biochemistry, 2009. **78**(1): p. 929-958.
12. Viguet-Carrin, S., P. Garnero, and P.D. Delmas, *The role of collagen in bone strength.* Osteoporosis International, 2006. **17**(3): p. 319-336.
13. Amirrah, I.N., et al., *A Comprehensive Review on Collagen Type I Development of Biomaterials for Tissue Engineering: From Biosynthesis to Bioscaffold.* Biomedicines, 2022. **10**(9): p. 2307.
14. Carr, B.P., et al., *Collagen Alignment via Electro-Compaction for Biofabrication Applications: A Review.* Polymers, 2022. **14**(20): p. 4270.
15. Cornette, P., et al. *Impact of Collagen Crosslinking on Dislocated Human Shoulder*

Capsules—Effect on Structural and Mechanical Properties. International Journal of Molecular Sciences, 2022. **23**, DOI: 10.3390/ijms23042297.

16. Carvalho, M.S., et al., *Bone Matrix Non-Collagenous Proteins in Tissue Engineering: Creating New Bone by Mimicking the Extracellular Matrix.* Polymers, 2021. **13**(7): p. 1095.
17. Bellahcène, A., et al., *Small integrin-binding ligand N-linked glycoproteins (SIBLINGs): multifunctional proteins in cancer.* Nature Reviews Cancer, 2008. **8**(3): p. 212-226.
18. Sodek, J., B. Ganss, and M.D. McKee, *Osteopontin.* Critical Reviews in Oral Biology & Medicine, 2000. **11**(3): p. 279-303.
19. Giachelli, C.M. and S. Steitz, *Osteopontin: a versatile regulator of inflammation and biomineralization.* Matrix Biology, 2000. **19**(7): p. 615-622.
20. McKee, M. and A. Nanci, *Osteopontin at mineralized tissue interfaces in bone, teeth, and osseointegrated implants: ultrastructural distribution and implications for mineralized tissue formation, turnover, and repair.* Microscopy research and technique, 1996. **33**(2): p. 141-164.
21. Boskey, A.L., et al., *Osteopontin-hydroxyapatite interactions in vitro: inhibition of hydroxyapatite formation and growth in a gelatin-gel.* Bone and Mineral, 1993. **22**(2): p. 147-159.
22. Boskey, A.L., et al., *Osteopontin Deficiency Increases Mineral Content and Mineral Crystallinity in Mouse Bone.* Calcified Tissue International, 2002. **71**(2): p. 145-154.
23. Hunter, G.K., *Role of Osteopontin in Modulation of Hydroxyapatite Formation.* Calcified Tissue International, 2013. **93**(4): p. 348-354.
24. Hunter, G.K. and H.A. Goldberg, *Nucleation of hydroxyapatite by bone sialoprotein.* Proceedings of the National Academy of Sciences, 1993. **90**(18): p. 8562-8565.
25. Baht, G.S., G.K. Hunter, and H.A. Goldberg, *Bone sialoprotein–collagen interaction promotes hydroxyapatite nucleation.* Matrix Biology, 2008. **27**(7): p. 600-608.
26. Dobbie, H., et al., *Matrix extracellular phosphoglycoprotein causes phosphaturia in rats by inhibiting tubular phosphate reabsorption.* Nephrology Dialysis Transplantation, 2008. **23**(2): p. 730-733.
27. Tartaix, P.H., et al., *In Vitro Effects of Dentin Matrix Protein-1 on Hydroxyapatite Formation Provide Insights into in Vivo Functions*.* Journal of Biological Chemistry, 2004. **279**(18): p. 18115-18120.
28. He, G., et al., *Phosphorylation of phosphophoryn is crucial for its function as a*

mediator of biomineralization. Journal of Biological Chemistry, 2005. **280**(39): p. 33109-33114.

29. Mochida, Y., et al., *Decorin modulates matrix mineralization in vitro.* Biochemical and Biophysical Research Communications, 2003. **305**(1): p. 6-9.
30. Golub, E.E., *Role of matrix vesicles in biomineralization.* Biochimica et Biophysica Acta (BBA) - General Subjects, 2009. **1790**(12): p. 1592-1598.
31. Bottini, M., et al., *Matrix vesicles from chondrocytes and osteoblasts: Their biogenesis, properties, functions and biomimetic models.* Biochimica et Biophysica Acta (BBA) - General Subjects, 2018. **1862**(3): p. 532-546.
32. Pasteris, J.D., B. Wopenka, and E. Valsami-Jones, *Bone and Tooth Mineralization: Why Apatite?* Elements, 2008. **4**(2): p. 97-104.
33. Mouriño, V. and A.R. Boccaccini, *Bone tissue engineering therapeutics: controlled drug delivery in three-dimensional scaffolds.* Journal of The Royal Society Interface, 2009. **7**(43): p. 209-227.
34. Skinner, H.C.W., *Biominerals.* Mineralogical Magazine, 2005. **69**(5): p. 621-641.
35. Elliott, J.C., *Calcium Phosphate Biominerals.* Reviews in Mineralogy and Geochemistry, 2002. **48**(1): p. 427-453.
36. Sinusaite, L., et al., *Effect of Mn doping on hydrolysis of low-temperature synthesized metastable alpha-tricalcium phosphate.* Ceramics International, 2021. **47**(9): p. 12078-12083.
37. Cheah, C.W., et al. *Synthetic Material for Bone, Periodontal, and Dental Tissue Regeneration: Where Are We Now, and Where Are We Heading Next?* Materials, 2021. **14**, DOI: 10.3390/ma14206123.
38. Dorozhkin, S.V. and M. Epple, *Biological and Medical Significance of Calcium Phosphates.* Angewandte Chemie International Edition, 2002. **41**(17): p. 3130-3146.
39. Zhao, J., et al., *First detection, characterization, and application of amorphous calcium phosphate in dentistry.* Journal of Dental Sciences, 2012. **7**(4): p. 316-323.
40. C. Chow, L., *Next generation calcium phosphate-based biomaterials.* Dental Materials Journal, 2009. **28**(1): p. 1-10.
41. Khan, A., et al., *Bioactive behavior of silicon substituted calcium phosphate based bioceramics for bone regeneration.* Materials science & engineering. C, Materials for biological applications, 2014. **35**: p. 245-52.
42. Anderson , H.C., *ELECTRON MICROSCOPIC STUDIES OF INDUCED CARTILAGE*

DEVELOPMENT AND CALCIFICATION. Journal of Cell Biology, 1967. **35**(1): p. 81-101.

43. Bonucci, E., *Fine structure of early cartilage calcification.* Journal of Ultrastructure Research, 1967. **20**(1): p. 33-50.
44. Xiao, Z., et al., *Proteomic analysis of extracellular matrix and vesicles.* Journal of Proteomics, 2009. **72**(1): p. 34-45.
45. Xiao, Z., et al., *Analysis of the extracellular matrix vesicle proteome in mineralizing osteoblasts.* Journal of Cellular Physiology, 2007. **210**(2): p. 325-335.
46. Anderson, H.C., *Matrix vesicles and calcification.* Current Rheumatology Reports, 2003. **5**(3): p. 222-226.
47. Azoidis, I., S.C. Cox, and O.G. Davies, *The role of extracellular vesicles in biomineralisation: current perspective and application in regenerative medicine.* Journal of Tissue Engineering, 2018. **9**: p. 2041731418810130.
48. Robison, R., *The Possible Significance of Hexosephosphoric Esters in Ossification.* Biochemical Journal, 1923. **17**(2): p. 286-293.
49. Golub, E.E. and K. Boesze-Battaglia, *The role of alkaline phosphatase in mineralization.* Current Opinion in Orthopaedics, 2007. **18**(5): p. 444-448.
50. Millán, J.L. and M.P. Whyte, *Alkaline Phosphatase and Hypophosphatasia.* Calcified Tissue International, 2016. **98**(4): p. 398-416.
51. Colaço, E., et al., *Enzyme-assisted mineralization of calcium phosphate: exploring confinement for the design of highly crystalline nano-objects.* Nanoscale, 2020. **12**(18): p. 10051-10064.
52. Ikezawa, H., *Glycosylphosphatidylinositol (GPI)-Anchored Proteins.* Biological and Pharmaceutical Bulletin, 2002. **25**(4): p. 409-417.
53. Harrison, G., I.M. Shapiro, and E.E. Golub, *The phosphatidylinositol-glycolipid anchor on alkaline phosphatase facilitates mineralization initiation in vitro.* Journal of Bone and Mineral Research, 1995. **10**(4): p. 568-573.
54. Guibert, C. and J. Landoulsi *Enzymatic Approach in Calcium Phosphate Biomineralization: A Contribution to Reconcile the Physicochemical with the Physiological View*. International Journal of Molecular Sciences, 2021. **22**, DOI: 10.3390/ijms222312957.
55. Stec, B., K.M. Holtz, and E.R. Kantrowitz, *A revised mechanism for the alkaline phosphatase reaction involving three metal ions11Edited by R. Huber.* Journal of

Molecular Biology, 2000. **299**(5): p. 1303-1311.

56. Henthorn, P.S. and M.P. Whyte, *Missense Mutations of the Tissue-Nonspecific Alkaline Phosphatase Gene in Hypophosphatasia.* Clinical Chemistry, 1992. **38**(12): p. 2501-2505.
57. Meyer, J.L., *Can biological calcification occur in the presence of pyrophosphate?* Archives of Biochemistry and Biophysics, 1984. **231**(1): p. 1-8.
58. McGaughey, C., *Binding of Polyphosphates and Phosphonates to Hydroxyapatite, Subsequent Hydrolysis, Phosphate Exchange and Effects on Demineralization, Mineralization and Microcrystal Aggregation.* Caries Research, 2009. **17**(3): p. 229-241.
59. Reichenberger, E., et al., *Autosomal Dominant Craniometaphyseal Dysplasia Is Caused by Mutations in the Transmembrane Protein ANK.* The American Journal of Human Genetics, 2001. **68**(6): p. 1321-1326.
60. Nürnberg, P., et al., *Heterozygous mutations in ANKH, the human ortholog of the mouse progressive ankylosis gene, result in craniometaphyseal dysplasia.* Nature Genetics, 2001. **28**(1): p. 37-41.
61. Pendleton, A., et al., *Mutations in ANKH Cause Chondrocalcinosis.* The American Journal of Human Genetics, 2002. **71**(4): p. 933-940.
62. Williams, C.J., et al., *Autosomal Dominant Familial Calcium Pyrophosphate Dihydrate Deposition Disease Is Caused by Mutation in the Transmembrane Protein ANKH.* The American Journal of Human Genetics, 2002. **71**(4): p. 985-991.
63. Zaka, R., et al., *P5L mutation in Ank results in an increase in extracellular inorganic pyrophosphate during proliferation and nonmineralizing hypertrophy in stably transduced ATDC5 cells.* Arthritis Research & Therapy, 2006. **8**(6): p. R164.
64. Ho, A.M., M.D. Johnson, and D.M. Kingsley, *Role of the Mouse ank Gene in Control of Tissue Calcification and Arthritis.* Science, 2000. **289**(5477): p. 265-270.
65. Gurley, K.A., R.J. Reimer, and D.M. Kingsley, *Biochemical and Genetic Analysis of ANK in Arthritis and Bone Disease.* The American Journal of Human Genetics, 2006. **79**(6): p. 1017-1029.
66. Williams, C.J., *Familial calcium pyrophosphate dihydrate deposition disease and the ANKH gene.* Current Opinion in Rheumatology, 2003. **15**(3).
67. Genge, B.R., et al., *Establishment of the primary structure of the major lipid-dependent Ca2+ binding proteins of chicken growth plate cartilage matrix vesicles: Identity with*

anchorin cii (annexin V) and annexin II. Journal of Bone and Mineral Research, 1992. **7**(7): p. 807-819.

68. Kirsch, T., et al., *Annexin V-Mediated Calcium Flux across Membranes Is Dependent on the Lipid Composition: Implications for Cartilage Mineralization.* Biochemistry, 1997. **36**(11): p. 3359-3367.
69. Cao, X., et al., *Characterization, Cloning and Expression of the 67-kDa Annexin from Chicken Growth Plate Cartilage Matrix Vesicles.* Biochemical and Biophysical Research Communications, 1993. **197**(2): p. 556-561.
70. Peress, N.S., H.C. Anderson, and S.W. Sajdera, *The lipids of matrix vesicles from bovine fetal epiphyseal cartilage.* Calcified Tissue Research, 1974. **14**(1): p. 275-281.
71. Montessuit, C., J. Caverzasio, and J.P. Bonjour, *Characterization of a Pi transport system in cartilage matrix vesicles. Potential role in the calcification process.* Journal of Biological Chemistry, 1991. **266**(27): p. 17791-17797.
72. Hasegawa, T., et al., *Ultrastructural and biochemical aspects of matrix vesicle-mediated mineralization.* Japanese Dental Science Review, 2017. **53**(2): p. 34-45.
73. Mahamid, J., et al., *Bone mineralization proceeds through intracellular calcium phosphate loaded vesicles: A cryo-electron microscopy study.* Journal of Structural Biology, 2011. **174**(3): p. 527-535.
74. Boonrungsiman, S., et al., *The role of intracellular calcium phosphate in osteoblast-mediated bone apatite formation.* Proceedings of the National Academy of Sciences, 2012. **109**(35): p. 14170-14175.
75. Martin, R.B., et al., *Skeletal Biology*, in *Skeletal Tissue Mechanics*, R.B. Martin, et al., Editors. 2015, Springer New York: New York, NY. p. 35-93.
76. Landis, W.J., et al., *Mineral and Organic Matrix Interaction in Normally Calcifying Tendon Visualized in Three Dimensions by High-Voltage Electron Microscopic Tomography and Graphic Image Reconstruction.* Journal of Structural Biology, 1993. **110**(1): p. 39-54.
77. Toroian, D., J.E. Lim, and P.A. Price, *The size exclusion characteristics of type I collagen: Implications for the role of noncollagenous bone constituents in mineralization.* Journal of Biological Chemistry, 2007. **282**(31): p. 22437-22447.
78. Landis, W.J. and F.H. Silver, *Mineral Deposition in the Extracellular Matrices of Vertebrate Tissues: Identification of Possible Apatite Nucleation Sites on Type I Collagen.* Cells Tissues Organs, 2008. **189**(1-4): p. 20-24.

79. Wang, Y., et al., *The predominant role of collagen in the nucleation, growth, structure and orientation of bone apatite.* Nature Materials, 2012. **11**(8): p. 724-733.
80. Liu, Y., et al., *Hierarchical and non-hierarchical mineralisation of collagen.* Biomaterials, 2011. **32**(5): p. 1291-1300.
81. Qi, Y., et al., *Effects of Molecular Weight and Concentration of Poly(Acrylic Acid) on Biomimetic Mineralization of Collagen.* ACS Biomaterials Science & Engineering, 2018. **4**(8): p. 2758-2766.
82. Chen, Y., et al., *Stabilizing amorphous calcium phosphate phase by citrate adsorption.* CrystEngComm, 2014. **16**(10): p. 1864-1867.
83. Nudelman, F., et al., *The role of collagen in bone apatite formation in the presence of hydroxyapatite nucleation inhibitors.* Nature Materials, 2010. **9**(12): p. 1004-1009.
84. Gower, L.B. and D.J. Odom, *Deposition of calcium carbonate films by a polymer-induced liquid-precursor (PILP) process.* Journal of Crystal Growth, 2000. **210**(4): p. 719-734.
85. Olszta, M.J., et al., *Bone structure and formation: A new perspective.* Materials Science and Engineering: R: Reports, 2007. **58**(3): p. 77-116.
86. Zhou, Z., et al., *Polyelectrolyte–calcium complexes as a pre-precursor induce biomimetic mineralization of collagen.* Nanoscale, 2021. **13**(2): p. 953-967.
87. Jiang, W., et al., *Multiscale structural evolution of citrate-triggered intrafibrillar and interfibrillar mineralization in dense collagen gels.* Journal of Structural Biology, 2020. **212**(1): p. 107592.
88. Fratzl, P., *Collagen: Structure and Mechanics, an Introduction*, in *Collagen: Structure and Mechanics*, P. Fratzl, Editor. 2008, Springer US: Boston, MA. p. 1-13.
89. Nair, A.K., A. Gautieri, and M.J. Buehler, *Role of Intrafibrillar Collagen Mineralization in Defining the Compressive Properties of Nascent Bone.* Biomacromolecules, 2014. **15**(7): p. 2494-2500.
90. Karunaratne, A., et al., *Significant deterioration in nanomechanical quality occurs through incomplete extrafibrillar mineralization in rachitic bone: Evidence from in-situ synchrotron X-ray scattering and backscattered electron imaging.* Journal of Bone and Mineral Research, 2012. **27**(4): p. 876-890.
91. Nair, A.K., et al., *Molecular mechanics of mineralized collagen fibrils in bone.* Nature Communications, 2013. **4**(1): p. 1724.
92. Bayraktar, D. and A.C. Tas, *Formation of hydroxyapatite precursors at 37 °C in urea-*

and enzyme urease-containing body fluids. Journal of Materials Science Letters, 2001. **20**(5): p. 401-403.

93. Hoffmann, C., C. Zollfrank, and G. Ziegler, *Enzyme-catalysed synthesis of calcium phosphates.* Journal of Materials Science: Materials in Medicine, 2008. **19**(2): p. 907-915.
94. Colaço, E., et al., *Calcium phosphate mineralization through homogenous enzymatic catalysis: Investigation of the early stages.* Journal of Colloid and Interface Science, 2020. **565**: p. 43-54.
95. Rauner, N., et al., *Enzymatic mineralization generates ultrastiff and tough hydrogels with tunable mechanics.* Nature, 2017. **543**(7645): p. 407-410.
96. Brena, B., P. González-Pombo, and F. Batista-Viera, *Immobilization of Enzymes: A Literature Survey*, in *Immobilization of Enzymes and Cells: Third Edition*, J.M. Guisan, Editor. 2013, Humana Press: Totowa, NJ. p. 15-31.
97. Zaborsky, O.R., *Immobilization of Enzymes by Adsorption*, in *Biomedical Applications of Immobilized Enzymes and Proteins: Volume 1*, T.M.S. Chang, Editor. 1977, Springer US: Boston, MA. p. 37-46.
98. Osathanon, T., C.M. Giachelli, and M.J. Somerman, *Immobilization of alkaline phosphatase on microporous nanofibrous fibrin scaffolds for bone tissue engineering.* Biomaterials, 2009. **30**(27): p. 4513-4521.
99. Aminian, A., et al., *Enzyme-assisted calcium phosphate biomineralization on an inert alumina surface.* Acta Biomaterialia, 2015. **13**: p. 335-343.
100. Ferraris, S., et al., *Surface modification of Ti-6Al-4 V alloy for biomineralization and specific biological response: part II, alkaline phosphatase grafting.* Journal of Materials Science: Materials in Medicine, 2011. **22**(8): p. 1835-1842.
101. de Jonge, L.T., et al., *Electrosprayed Enzyme Coatings as Bioinspired Alternatives to Bioceramic Coatings for Orthopedic and Oral Implants.* Advanced Functional Materials, 2009. **19**(5): p. 755-762.
102. Andrade, M.A.R., et al., *Is alkaline phosphatase biomimeticaly immobilized on titanium able to propagate the biomineralization process?* Archives of Biochemistry and Biophysics, 2019. **663**: p. 192-198.
103. Yao, J., et al., *Highly Mineralized Biomimetic Polysaccharide Nanofiber Materials Using Enzymatic Mineralization.* Biomacromolecules, 2020. **21**(6): p. 2176-2186.
104. Douglas, T.E.L., et al., *Enzymatic Mineralization of Hydrogels for Bone Tissue*

Engineering by Incorporation of Alkaline Phosphatase. Macromolecular Bioscience, 2012. **12**(8): p. 1077-1089.

105. Douglas, T.E.L., et al., *Enzymatic mineralization of gellan gum hydrogel for bone tissue-engineering applications and its enhancement by polydopamine.* Journal of Tissue Engineering and Regenerative Medicine, 2014. **8**(11): p. 906-918.
106. Lišková, J., et al., *Phytase-mediated enzymatic mineralization of chitosan-enriched hydrogels.* Materials Letters, 2018. **214**: p. 186-189.
107. Xie, M., et al., *Biocomposites prepared by alkaline phosphatase mediated mineralization of alginate microbeads.* RSC Advances, 2012. **2**(4): p. 1457-1465.
108. Samal, S.K., et al., *Enzymatic Mineralization of Silk Scaffolds.* Macromolecular Bioscience, 2014. **14**(7): p. 991-1003.
109. Chen, L., et al., *Biomineralized Hydrogel with Enhanced Toughness by Chemical Bonding of Alkaline Phosphatase and Vinylphosphonic Acid in Collagen Framework.* ACS Biomaterials Science & Engineering, 2019. **5**(3): p. 1405-1415.
110. Beertsen, W. and T. van den Bos, *Alkaline phosphatase induces the mineralization of sheets of collagen implanted subcutaneously in the rat.* The Journal of Clinical Investigation, 1992. **89**(6): p. 1974-1980.
111. Yamauchi, K., et al., *Preparation of collagen/calcium phosphate multilayer sheet using enzymatic mineralization.* Biomaterials, 2004. **25**(24): p. 5481-5489.
112. Bosco, R., et al., *Configurational effects of collagen/ALP coatings on enzyme immobilization and surface mineralization.* Applied Surface Science, 2014. **311**: p. 292-299.
113. Iler, R.K., *Multilayers of colloidal particles.* Journal of Colloid and Interface Science, 1966. **21**(6): p. 569-594.
114. Decher, G., *Fuzzy Nanoassemblies: Toward Layered Polymeric Multicomposites.* Science, 1997. **277**(5330): p. 1232-1237.
115. Richardson, J.J., et al., *Innovation in Layer-by-Layer Assembly.* Chemical Reviews, 2016. **116**(23): p. 14828-14867.
116. Richardson, J.J., M. Björnmalm, and F. Caruso, *Technology-driven layer-by-layer assembly of nanofilms.* Science, 2015. **348**(6233): p. aaa2491.
117. Lvov, Y. and H. Mohwald, *Electrostatic layer-by-layer assembly of proteins and polyions*. 2000: Dekker: New York.
118. Hoogeveen, N.G., et al., *Formation and Stability of Multilayers of Polyelectrolytes.*

Langmuir, 1996. **12**(15): p. 3675-3681.

119. Arys, X., et al., *Structural studies on thin organic coatings built by repeated adsorption of polyelectrolytes.* Progress in Organic Coatings, 1998. **34**(1): p. 108-118.
120. Cochin, D., et al., *Layered Nanostructures with LC-Polymers, Polyelectrolytes, and Inorganics.* Macromolecules, 1997. **30**(16): p. 4775-4779.
121. Schoeler, B., et al., *Polyelectrolyte Multilayer Films of Different Charge Density Copolymers with Synergistic Nonelectrostatic Interactions Prepared by the Layer-by-Layer Technique.* Langmuir, 2004. **20**(7): p. 2730-2738.
122. Borges, J. and J.F. Mano, *Molecular Interactions Driving the Layer-by-Layer Assembly of Multilayers.* Chemical Reviews, 2014. **114**(18): p. 8883-8942.
123. Stockton, W.B. and M.F. Rubner, *Molecular-Level Processing of Conjugated Polymers. 4. Layer-by-Layer Manipulation of Polyaniline via Hydrogen-Bonding Interactions.* Macromolecules, 1997. **30**(9): p. 2717-2725.
124. Wang, L., et al., *A new approach for the fabrication of an alternating multilayer film of poly(4-vinylpyridine) and poly(acrylic acid) based on hydrogen bonding.* Macromolecular Rapid Communications, 1997. **18**(6): p. 509-514.
125. Wang, L., et al., *Investigation into an Alternating Multilayer Film of Poly(4-Vinylpyridine) and Poly(acrylic acid) Based on Hydrogen Bonding.* Langmuir, 1999. **15**(4): p. 1360-1363.
126. Fu, Y., et al., *Multilayer Assemblies of Poly(4-vinylpyridine) and Poly(acrylic acid) Bearing Photoisomeric Spironaphthoxazine via Hydrogen Bonding.* Langmuir, 2002. **18**(12): p. 4989-4995.
127. Sukhishvili, S.A. and S. Granick, *Layered, Erasable, Ultrathin Polymer Films.* Journal of the American Chemical Society, 2000. **122**(39): p. 9550-9551.
128. Sukhishvili, S.A. and S. Granick, *Layered, Erasable Polymer Multilayers Formed by Hydrogen-Bonded Sequential Self-Assembly.* Macromolecules, 2002. **35**(1): p. 301-310.
129. Yang, S., et al., *The influence of pH on a hydrogen-bonded assembly film.* Soft Matter, 2007. **3**(4): p. 463-469.
130. Yang, S.Y. and M.F. Rubner, *Micropatterning of Polymer Thin Films with pH-Sensitive and Cross-linkable Hydrogen-Bonded Polyelectrolyte Multilayers.* Journal of the American Chemical Society, 2002. **124**(10): p. 2100-2101.
131. Lee, S.-W., et al., *Controlling the Cell-Adhesion Properties of Poly(acrylic acid)/Polyacrylamide Hydrogen-Bonded Multilayers.* Macromolecules, 2012. **45**(15):

p. 6120-6126.

132. Zelikin, A.N., J.F. Quinn, and F. Caruso, *Disulfide Cross-Linked Polymer Capsules: En Route to Biodeconstructible Systems.* Biomacromolecules, 2006. **7**(1): p. 27-30.

133. Zelikin, A.N., Q. Li, and F. Caruso, *Degradable Polyelectrolyte Capsules Filled with Oligonucleotide Sequences.* Angewandte Chemie International Edition, 2006. **45**(46): p. 7743-7745.

134. Ochs, C.J., et al., *Biodegradable Click Capsules with Engineered Drug-Loaded Multilayers.* ACS Nano, 2010. **4**(3): p. 1653-1663.

135. Dou, Y., et al., *Temperature-Controlled Electrochemical Switch Based on Layered Double Hydroxide/Poly(N-Isopropylacrylamide) Ultrathin Films Fabricated via Layer-by-Layer Assembly.* Langmuir, 2012. **28**(25): p. 9535-9542.

136. Serizawa, T., K. Yamamoto, and M. Akashi, *A Novel Fabrication of Ultrathin Poly(vinylamine) Films with a Molecularly Smooth Surface.* Langmuir, 1999. **15**(13): p. 4682-4684.

137. Serizawa, T. and M. Akashi, *A novel approach for fabricating ultrathin polymer films by the repetition of the adsorption/drying processes.* Journal of Polymer Science Part A: Polymer Chemistry, 1999. **37**(13): p. 1903-1906.

138. Lewandowska, K., D.U. Staszewska, and M. Bohdanecký, *The Huggins viscosity coefficient of aqueous solution of poly(vinyl alcohol).* European Polymer Journal, 2001. **37**(1): p. 25-32.

139. Kozlov, M., et al., *Adsorption of Poly(vinyl alcohol) onto Hydrophobic Substrates. A General Approach for Hydrophilizing and Chemically Activating Surfaces.* Macromolecules, 2003. **36**(16): p. 6054-6059.

140. Kozlov, M. and T.J. McCarthy, *Adsorption of Poly(Vinyl Alcohol) from Water to a Hydrophobic Surface: Effects of Molecular Weight, Degree of Hydrolysis, Salt, and Temperature.* Langmuir, 2004. **20**(21): p. 9170-9176.

141. K, J., S.L. Hsu, and T.J. McCarthy, *Versatile Multilayer Thin Film Preparation Using Hydrophobic Interactions, Crystallization, and Chemical Modification of Poly(vinyl alcohol).* Langmuir, 2007. **23**(6): p. 3260-3264.

142. Lojou, É. and P. Bianco, *Buildup of Polyelectrolyte−Protein Multilayer Assemblies on Gold Electrodes. Role of the Hydrophobic Effect.* Langmuir, 2004. **20**(3): p. 748-755.

143. Liu, Y., et al., *Multilayer Dendrimer–Polyanhydride Composite Films on Glass, Silicon, and Gold Wafers.* Angewandte Chemie International Edition in English, 1997. **36**(19):

p. 2114-2116.

144. Kohli, P. and G.J. Blanchard, *Applying Polymer Chemistry to Interfaces: Layer-by-Layer and Spontaneous Growth of Covalently Bound Multilayers.* Langmuir, 2000. **16**(10): p. 4655-4661.

145. Serizawa, T., et al., *Thermoresponsive Ultrathin Hydrogels Prepared by Sequential Chemical Reactions.* Macromolecules, 2002. **35**(6): p. 2184-2189.

146. Serizawa, T., et al., *Stepwise Preparation and Characterization of Ultrathin Hydrogels Composed of Thermoresponsive Polymers.* Macromolecules, 2004. **37**(17): p. 6531-6536.

147. Such, G.K., et al., *Assembly of Ultrathin Polymer Multilayer Films by Click Chemistry.* Journal of the American Chemical Society, 2006. **128**(29): p. 9318-9319.

148. Such, G.K., et al., *Ultrathin, Responsive Polymer Click Capsules.* Nano Letters, 2007. **7**(6): p. 1706-1710.

149. Zhang, Y., et al., *Fabrication of Stable Hollow Capsules by Covalent Layer-by-Layer Self-Assembly.* Macromolecules, 2003. **36**(11): p. 4238-4240.

150. Liang, Z., et al., *Covalent Layer-by-Layer Assembly of Conjugated Polymers and CdSe Nanoparticles: Multilayer Structure and Photovoltaic Properties.* Advanced Functional Materials, 2006. **16**(4): p. 542-548.

151. Amigoni, S., et al., *Covalent Layer-by-Layer Assembled Superhydrophobic Organic−Inorganic Hybrid Films.* Langmuir, 2009. **25**(18): p. 11073-11077.

152. Shimazaki, Y., et al., *Preparation of the Layer-by-Layer Deposited Ultrathin Film Based on the Charge-Transfer Interaction.* Langmuir, 1997. **13**(6): p. 1385-1387.

153. Shimazaki, Y., et al., *Preparation and Characterization of the Layer-by-Layer Deposited Ultrathin Film Based on the Charge-Transfer Interaction in Organic Solvents.* Langmuir, 1998. **14**(10): p. 2768-2773.

154. Shimazaki, Y., et al., *Alternate Adsorption of Polymers on a Gold Surface through the Charge-Transfer Interaction.* Macromolecules, 1999. **32**(24): p. 8220-8223.

155. Shimazaki, Y., S. Ito, and N. Tsutsumi, *Adsorption-Induced Second Harmonic Generation from the Layer-by-Layer Deposited Ultrathin Film Based on the Charge-Transfer Interaction.* Langmuir, 2000. **16**(24): p. 9478-9482.

156. Shimazaki, Y., et al., *Molecular Weight Dependence of Alternate Adsorption through Charge-Transfer Interaction.* Langmuir, 2001. **17**(3): p. 953-956.

157. Shiratori, S.S. and M.F. Rubner, *pH-Dependent Thickness Behavior of Sequentially*

Adsorbed Layers of Weak Polyelectrolytes. Macromolecules, 2000. **33**(11): p. 4213-4219.

158. Bieker, P. and M. Schönhoff, *Linear and Exponential Growth Regimes of Multilayers of Weak Polyelectrolytes in Dependence on pH.* Macromolecules, 2010. **43**(11): p. 5052-5059.

159. Picart, C., et al., *Molecular basis for the explanation of the exponential growth of polyelectrolyte multilayers.* Proceedings of the National Academy of Sciences, 2002. **99**(20): p. 12531-12535.

160. Tan, H.L., et al., *Temperature Dependence of Polyelectrolyte Multilayer Assembly.* Langmuir, 2003. **19**(22): p. 9311-9314.

161. Dubas, S.T. and J.B. Schlenoff, *Swelling and Smoothing of Polyelectrolyte Multilayers by Salt.* Langmuir, 2001. **17**(25): p. 7725-7727.

162. Dubas, S.T. and J.B. Schlenoff, *Polyelectrolyte Multilayers Containing a Weak Polyacid: Construction and Deconstruction.* Macromolecules, 2001. **34**(11): p. 3736-3740.

163. Liu, G., et al., *Role of Chain Interpenetration in Layer-by-Layer Deposition of Polyelectrolytes.* The Journal of Physical Chemistry B, 2008. **112**(11): p. 3333-3338.

164. Liu, G., et al., *Roles of Chain Conformation and Interpenetration in the Growth of a Polyelectrolyte Multilayer.* The Journal of Physical Chemistry B, 2008. **112**(14): p. 4167-4171.

165. Fery, A., et al., *Nanoporous Thin Films Formed by Salt-Induced Structural Changes in Multilayers of Poly(acrylic acid) and Poly(allylamine).* Langmuir, 2001. **17**(13): p. 3779-3783.

166. Georgieva, R., et al., *Influence of different salts on micro-sized polyelectrolyte hollow capsules.* Journal of Materials Chemistry, 2005. **15**(40): p. 4301-4310.

167. Milkova, V. and T. Radeva, *Effect of ionic strength and molecular weight on electrical properties and thickness of polyelectrolyte bi-layers.* Colloids and Surfaces A: Physicochemical and Engineering Aspects, 2013. **424**: p. 52-58.

168. McAloney, R.A., et al., *Atomic Force Microscopy Studies of Salt Effects on Polyelectrolyte Multilayer Film Morphology.* Langmuir, 2001. **17**(21): p. 6655-6663.

169. El Haitami, A.E., et al., *Effect of the Supporting Electrolyte Anion on the Thickness of PSS/PAH Multilayer Films and on Their Permeability to an Electroactive Probe.* Langmuir, 2009. **25**(4): p. 2282-2289.

170. Dragan, E.S., S. Schwarz, and K.-J. Eichhorn, *Specific effects of the counterion type and concentration on the construction and morphology of polycation/azo dye multilayers.* Colloids and Surfaces A: Physicochemical and Engineering Aspects, 2010. **372**(1): p. 210-216.

171. Dodoo, S., et al., *Effect of ionic strength and type of ions on the structure of water swollen polyelectrolyte multilayers.* Physical Chemistry Chemical Physics, 2011. **13**(21): p. 10318-10325.

172. Sun, B., et al., *Assembly of Multilayered Films Using Well-Defined, End-Labeled Poly(acrylic acid): Influence of Molecular Weight on Exponential Growth in a Synthetic Weak Polyelectrolyte System.* Langmuir, 2007. **23**(16): p. 8452-8459.

173. Porcel, C., et al., *Influence of the Polyelectrolyte Molecular Weight on Exponentially Growing Multilayer Films in the Linear Regime.* Langmuir, 2007. **23**(4): p. 1898-1904.

174. Sui, Z., D. Salloum, and J.B. Schlenoff, *Effect of Molecular Weight on the Construction of Polyelectrolyte Multilayers: Stripping versus Sticking.* Langmuir, 2003. **19**(6): p. 2491-2495.

175. Houska, M., E. Brynda, and K. Bohatá, *The effect of polyelectrolyte chain length on layer-by-layer protein/polyelectrolyte assembly—an experimental study.* Journal of Colloid and Interface Science, 2004. **273**(1): p. 140-147.

176. Kujawa, P., et al., *Effect of Molecular Weight on the Exponential Growth and Morphology of Hyaluronan/Chitosan Multilayers: A Surface Plasmon Resonance Spectroscopy and Atomic Force Microscopy Investigation.* Journal of the American Chemical Society, 2005. **127**(25): p. 9224-9234.

177. Mermut, O. and C.J. Barrett, *Effects of Charge Density and Counterions on the Assembly of Polyelectrolyte Multilayers.* The Journal of Physical Chemistry B, 2003. **107**(11): p. 2525-2530.

178. Koetse, M., et al., *Influence of Charge Density and Distribution on the Internal Structure of Electrostatically Self-assembled Polyelectrolyte Films.* Langmuir, 2002. **18**(5): p. 1655-1660.

179. Schoeler, B., G. Kumaraswamy, and F. Caruso, *Investigation of the Influence of Polyelectrolyte Charge Density on the Growth of Multilayer Thin Films Prepared by the Layer-by-Layer Technique.* Macromolecules, 2002. **35**(3): p. 889-897.

180. Voigt, U., et al., *Charge Effects on the Formation of Multilayers Containing Strong Polyelectrolytes.* The Journal of Physical Chemistry B, 2003. **107**(22): p. 5273-5280.

181. Steitz, R., W. Jaeger, and R.v. Klitzing, *Influence of Charge Density and Ionic Strength on the Multilayer Formation of Strong Polyelectrolytes.* Langmuir, 2001. **17**(15): p. 4471-4474.
182. D'Souza, S.F., *Immobilization and stabilization of biomaterials for biosensor applications.* Applied Biochemistry and Biotechnology, 2001. **96**(1): p. 225-238.
183. Katchalski, E., I. Silman, and R. Goldman, *Effect of the microenvironment on the mode of action of immobilized enzymes.* Advances in enzymology and related areas of molecular biology, 1971. **34**: p. 445-536.
184. Silva, R.A., et al., *Protein Adsorption onto Polyelectrolyte Layers: Effects of Protein Hydrophobicity and Charge Anisotropy.* Langmuir, 2010. **26**(17): p. 14032-14038.
185. Sukhishvili, S.A., E. Kharlampieva, and V. Izumrudov, *Where Polyelectrolyte Multilayers and Polyelectrolyte Complexes Meet.* Macromolecules, 2006. **39**(26): p. 8873-8881.
186. Kayitmazer, A.B., et al., *Protein–polyelectrolyte interactions.* Soft Matter, 2013. **9**(9): p. 2553-2583.
187. Izumrudov, V.A., E. Kharlampieva, and S.A. Sukhishvili, *Multilayers of a Globular Protein and a Weak Polyacid: Role of Polyacid Ionization in Growth and Decomposition in Salt Solutions.* Biomacromolecules, 2005. **6**(3): p. 1782-1788.
188. Wang, B., et al., *Utilization of parameters developed in layer-by-layer fabrication of protein-containing films for enzyme immobilization.* Journal of Biomaterials Science, Polymer Edition, 2015. **26**(17): p. 1312-1326.
189. Kumar, M.R., E.F. Merschrod S, and K.M. Poduska, *Collagen-Membrane-Induced Calcium Phosphate Electrocrystallization.* Crystal Growth & Design, 2011. **11**(1): p. 26-28.
190. Li, Y., et al., *pH effects on collagen fibrillogenesis in vitro: Electrostatic interactions and phosphate binding.* Materials Science and Engineering: C, 2009. **29**(5): p. 1643-1649.
191. Landoulsi, J., S. Demoustier-Champagne, and C. Dupont-Gillain, *Self-assembled multilayers based on native or denatured collagen: mechanism and synthesis of size-controlled nanotubes.* Soft Matter, 2011. **7**(7): p. 3337-3347.
192. Chen, Y.-W., et al. *Physical Chemistry Study of Collagen-Based Multilayer Films*. Gels, 2023. **9**, DOI: 10.3390/gels9030192.
193. Colaço, E., et al., *Embedding Collagen in Multilayers for Enzyme-Assisted*

Mineralization: A Promising Way to Direct Crystallization in Confinement. Biomacromolecules, 2021. **22**(8): p. 3460-3473.

194. Grant, G.G.S., et al., *Layer-By-Layer Assembly of Collagen Thin Films: Controlled Thickness and Biocompatibility.* Biomedical Microdevices, 2001. **3**(4): p. 301-306.
195. Sinani, V.A., et al., *Collagen Coating Promotes Biocompatibility of Semiconductor Nanoparticles in Stratified LBL Films.* Nano Letters, 2003. **3**(9): p. 1177-1182.
196. Zhang, J., et al., *Natural polyelectrolyte films based on layer-by layer deposition of collagen and hyaluronic acid.* Biomaterials, 2005. **26**(16): p. 3353-3361.
197. Mhanna, R.F., J. Vörös, and M. Zenobi-Wong, *Layer-by-Layer Films Made from Extracellular Matrix Macromolecules on Silicone Substrates.* Biomacromolecules, 2011. **12**(3): p. 609-616.
198. Chen, J.L., et al., *Improving blood-compatibility of titanium by coating collagen–heparin multilayers.* Applied Surface Science, 2009. **255**(15): p. 6894-6900.
199. Iqbal, M.H., et al., *Effect of the Buffer on the Buildup and Stability of Tannic Acid/Collagen Multilayer Films Applied as Antibacterial Coatings.* ACS Applied Materials & Interfaces, 2020. **12**(20): p. 22601-22612.
200. Heijmen, F.H., et al., *Cross-linking of dermal sheep collagen with tannic acid.* Biomaterials, 1997. **18**(10): p. 749-754.
201. Johansson, J.Å., et al., *Build-up of Collagen and Hyaluronic Acid Polyelectrolyte Multilayers.* Biomacromolecules, 2005. **6**(3): p. 1353-1359.

Chapter 2. Materials & Methods

1 Materials

1.1 Chemical products

Polyethylenimine(PEI, branced average M_w ~800, M_n ~600), poly(sodium 4-styrenesulfonate)(PSS, M_w ~70000 powder), poly(allylamine hydrochloride)(PAH, M_w ~17.5 kDa), calcium chloride ($CaCl_2$, ≥ 99%), α-glycerol phosphate magnesium salt hydrate (Sub-Mg, ~ 85%), rac-Glycerol-1-phosphate sodium salt hydrate (Sub-Na, ≥ 95%), para-nitrophenyl phosphate disodium salt hexahydrate (pnpp, ≥ 99%) and para-nitrophenol (pnp, ≥ 99%), N-(3-dimethylaminopropyl)-N′-ethylcarbodiimide hydrochloride (EDC, crystalline), N-hydroxysuccinimide (NHS, 98%), 11-mercaptoundecanoic acid (MUDA, 95 %), and 11-mercapto-1-undecanol (MUD, 97 %), chloroform($CHCl_3$, ≥ 99.5%)), dimethylsulfoxyde (DMSO), ethanolamine hydrochloride (≥99%), triethylamine, citric acid, sodium cyanoborohydride ($NaCNBH_3$, 95 %) were purchased from Sigma-Aldrich (France). Hydrochloric acid (HCl, 37%) and sodium hydroxide (NaOH) were purchased from VWR (France). Magnesium chloride hexahydrate ($MgCl_2 \cdot 6H_2O$, hexahydrate, ≥ 99%) was purchased from ProLabo (France).

1.2 Biological products

Alkaline phosphatase from bovine intestinal mucosa (ALP, lyophilized powder, ≥10 DEA units/mg) was purchased from Sigma-Aldrich (France). Collagen G from bovine calf skin (Col, Type I collagen, 0.4% solution in 15 mmol/L HCl, 4 mg/mL) was purchased from Biochrom GmbH (Germany). Sodium hyaluronate (HA, Mw ~ 151-300 kDa) was purchased from Sigma-Aldrich and Lifecore Biomedical (U.S.A.).

All solutions were prepared in ultrapure water (MilliQ, resistivity 18.2 MΩ) which was produced through by a Millipore device (Millipore, France).

1.3 Surfaces

Round glass coverslips (d = 1 cm) used as substrate for imaging and calibration of AFM tip were purchased from VWR (France). Silicon wafer ((100), Si) for layer-by-layer assemblies were purchased from Sigma-Aldrich (France).

2 Real-time monitoring of enzyme-assisted mineralization in a homogeneous phase

2.1 Enzyme-assisted mineralization

The procedure is adapted from a previous work [1]. Four different solutions were freshly

prepared; $CaCl_2$ (0.1 M), $MgCl_2$ (0.1 M), Sub-Na (8.4~9.5 mM), ALP (1 mg/mL, aliquot, stored in freezer -20 ℃). The aliquot was thawed in the fridge (4 ℃) to preserve their activities and consumed in 3 days (Figure 2.1E). The solutions were mixed at 37 ℃ to reach the final concentration as shown in the table. Then, 100 μL of ALP solution was added in to the mixture to initiate the mineralization.

Table 1. Different conditions for enzyme-induced mineralization

	Variable [Substate]				Variable [$MgCl_2$]			
	$[Sub]_0$, mM	$CaCl_2$, mM	ALP, mg/mL		[Sub], mM	$CaCl_2$, mM	$[MgCl_2]_0$, mM	ALP, mg/mL
1*	3	11.4	0.1	1	7	11.4	0	0.1
2	4			2			1	
3	5			3			3	
4	6			4*			5	
5*	7			5			7	

* Subscript 0 means initial concentration
** the mark * indicating the conditions used for pH monitoring; section 2.3

2.2 Enzymatic activity in homogeneous solution

The catalytic activity of ALP in different conditions was explored using 4-nitrophenyl phosphate (pnpp) as a substrate of the enzyme according to the reaction in figure 2.1A. The production of pnp by hydrolysis reaction catalysed by ALP resulted in an increase of the absorbance of light at 410 nm (Figure 2.1B). So, the evolution of absorbance over time allows the monitoring of the enzymatic activity through the use of the Beer-Lamber law. The measurement of the ALP activity was performed in aqueous solutions at 37 ℃ using a UV-visible spectrophotometer (Biochrom Libra S60).

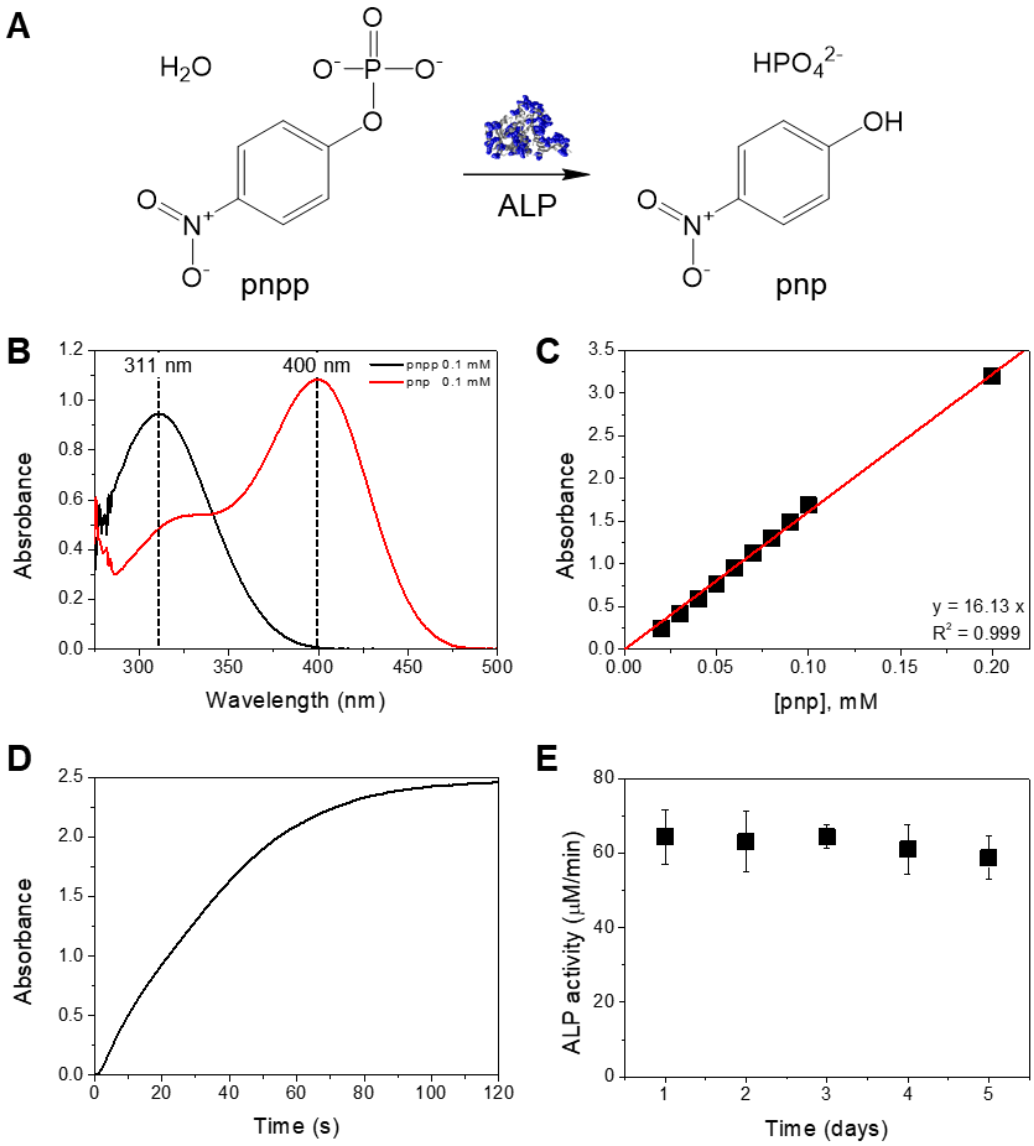

Figure 2. 1 Catalytic activity measurement of ALP using pnpp. (A) Hydrolysis reaction of pnpp by ALP. (B) Absorption spectra of pnpp and pnp. (C) Calibration curve by absorbances over various pnp concentrations. (D) Kinetics of pnp production over time at 7 mM of substrate with 11.4 mM of $CaCl_2$. (E) Stability of ALP stored at 4°C. Error bars correspond to the deviation of 5 measurements

Calibration curve

A calibration curve was obtained by diluting the 4-nitrophenol(pnp) solution (from 200 µM to 10 µM) around pH 8.4 to convert absorbances to produced pnp amount (Figure 2.1C). The pH of the freshly prepared solution is 5.8 so modified to 8.4 using 0.1 M NaOH. The absorbance of pnp was measured at the wavelength 410 nm using a 4 mL plastic cuvette (optical path length = 1 cm).

Catalytic activity of ALP

At least 30 min before measurements, a water bath connected to the spectrometer set the temperature as 37 °C. Ultrapure water was placed into the spectrometer and then measured as a blank. Three different solutions (pnpp, $CaCl_2$, $MgCl_2$) and ultrapure water were freshly prepared at pH 8.30~8.45 individually and placed in a water bath at 37 °C. It remained over 15 minutes to reach the temperature of the solution at 37 °C. Specifically, the pnpp solution is covered with aluminum foil because the substance is sensitive to light. 900 µL of the solution was prepared by mixing the three solutions in a 2 mL plastic cuvette (10 mm optical path length). The final concentration of pnpp and $MgCl_2$ and $CaCl_2$ is shown in *Table 1*. The cuvette was placed in the spectrometer and absorbance measurement started at wavelength 410 nm. After the first point (absorbance = 0) appeared, 100 µL of the ALP solution (1 mg/mL) was added into the cuvette and mixed very quickly then measured absorbances (Figure 2. 1D). The later addition of ALP after the initiation of the absorbance measurement is important to see the very initial activity of ALP.

2.3 pH monitoring in solutions

The pH evolution of mineralizing solution was monitored at 37 ± 0.2 °C using a double-walled flask equipped with a thermostatic bath and pH electrode (XC161, Hach Company, France). 18 mL of a solution containing substrate, $CaCl_2$, $MgCl_2$ was prepared. The experimental conditions are as below:

1 $[Sub]_0$ 3 mM

2 $[Sub]_0$ 7 mM

3 $[Sub]_0$ 7 mM + $[Mg^{2+}]_0$ 5 mM

The pH meter was introduced in the solution with a gentle stirring then added 2 mL of 1 mg/mL ALP solution (t = 0). The evolution of pH was recorded every 1 minute up to 3 hours.

2.4 Dynamic and static light scattering (DLS and SLS)

Light scattering techniques is a well-established to investigate properties of particles solution for example size, molecular weight, and diffusion. The principle is that a laser beam exposed into the sample and the scattered light intensity is measured at a certain angle by a detector (Figure 2.2A). In the thesis, we selected the measurement angle as 175 °. It gives a short path

length of laser within a sample so it minimizes multiple scattering by formation of minerals in the sample [2]. The first obtained result shows the intensity trace over a certain time which is known as SLS. It is the analysis of the absolute mean intensity which is influenced by several parameters such as molecular weight, concentration and the size of particles in solution. When the size and molecular weight are similar, the intensity depends on the concentration as shown in Figure 2.2B. DLS is the evaluation of the fluctuations of intensity. The correlation of intensity fluctuations (Figure 2.2C) is analyzed to calculate hydrodynamic size (d_H) of particles through the Stokes-Einstein equation [3, 4].

$$D = \frac{k_B T}{3\pi\eta d_H}$$

D: Diffusion coefficient (m^2/s)

k_B: Boltzmann constant (m^2kg/Ks^2)

T: Temperature (K)

η: viscosity (Pa.s)

d_H: Hydrodynamic diameter (m)

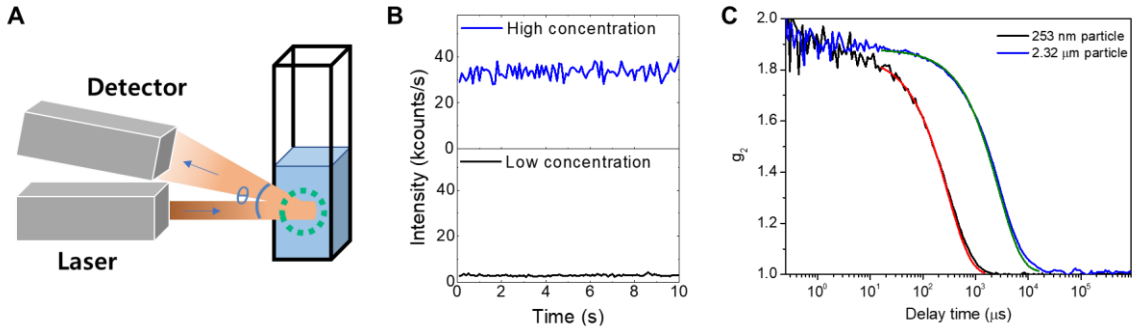

Figure 2. 2 Principle of light scattering. (A) Setup of light scattering measurement. A sample solution contained in a transparent cuvette and the scattering light is measured at 175° from incident laser. (B) Intensity fluctuation over time with different concentration of particles. (C) Correlogram and their fitting to determine the hydrodynamic sizes of particles.

DLS and SLS measurements were performed on an Anton Paar Litesizer 500. The scattered light was measured using the backscattering mode (175°), at 37.0 ± 0.2 °C, with the optical filter valued 4.50 and the focus position as 0.00 mm. Measurements proceeded over 5 runs of 10 seconds. 900 µL of a solution containing Sub-Na, $CaCl_2$ and $MgCl_2$ as *2.1* in 4 mL transparent plastic cuvette (optical path: 1 cm) was introduced into the instrument and

performed one measurement to make sure the solution is clean (indicating failed measurement in the instrument with flat correlation function, undefined hydrodynamic diameter and mean intensity close to 0). Then, 100 μL of ALP solution (1mg/mL) was introduced and started sequential measurements until it shows the hydrodynamic diameter above 1.8 μm to take into account the lesser degree of reliability for the big particles. Identical optical settings and procedures were adapted for each measurement. The monitoring was performed several times for each condition and remarkably identical evolutions were obtained for the different measurements.

2.5 Transmission electron microscopy (TEM)

TEM is a powerful imaging technique to observe the structure, morphology and composition of nanomaterials by transmitting an electron beam through a thin sample and collecting the resulting interactions. The concept of electron microscopy was firstly proposed by Max Knoll and Ernst Ruska in 1932 [5]. The basic setup of a TEM consists of an electron source, electromagnetic lenses, and a detector. The electron source, typically a tungsten filament, emits a beam of high-energy electrons. They are accelerated and focused by electromagnetic lenses and pass through the samples on a TEM support grid. When electrons penetrate samples, they undergo various interactions, such as elastic scattering, inelastic scattering, and diffraction, which bring information of composition, crystal structure and other properties. The detector collects and record transmitted electrons. One of the key advantages of TEM is its exceptional spatial resolution, allowing scientists to visualize details at the atomic level. The resolving power of TEM is determined by the wavelength of the electrons, which is much shorter than that of visible light. This enables the detection of individual atoms, lattice defects, and fine structural features. TEM also offers different imaging modes that provide additional information about the sample. Bright-field imaging, achieved by blocking the direct beam and collecting the transmitted electrons, provides contrast based on the different densities and thicknesses of the sample. Dark-field imaging, on the other hand, selectively collects electrons that have undergone specific scattering events, highlighting specific crystallographic features and defects. In addition to imaging, TEM enables the analysis of diffraction patterns produced by the interaction of electrons with the crystal lattice of the sample. Electron diffraction allows the determination of crystal structures, the identification of phases, and the measurement of lattice parameters. Selected-area electron diffraction (SAED) is a technique that utilizes a small aperture to limit the diffraction to a specific area, enabling the analysis of specific regions of the sample. Furthermore, TEM can be combined with other analytical techniques to provide

complementary information. Energy-dispersive X-ray spectroscopy (EDS) allows the identification and mapping of elements within the sample based on the characteristic X-rays emitted during electron-sample interactions.

In this thesis, TEM is used to investigate the morphology, phase and composition of CaP minerals formed by enzyme-assisted mineralization in homogeneous solutions in different stages.

Samples collected over 24 hours as final products

The mineralization was performed with a volume 20 mL with chemicals and their final concentrations shown in *2.1* at 37 °C with a gentle stirring for 24 hours. The entire solutions were then collected and centrifuged (3000 rpm for 10 min) three times and rinsed with water. Small amounts of precipitates were dispersed in 500 µL of water. Then 10 µL of the solution was deposited on Cu grids with carbon films (AGS160-3, Oxford instruments). After overnight drying, TEM micrographs were recorded using a JEOL-1011 instrument operating at an acceleration voltage of 100 kV and equipped with a CCD camera for micrograph acquisition. For each representative TEM micrograph, selected area electron diffraction (SAED) patterns were recorded to evaluate the crystallinity of the particles and possibly identify the crystal phase.

Samples collected within several hours as intermediates

1.0 mL of mineralisation solution was prepared as described in the section *2.1*. The mineralisation was then monitored by DLS at 37 °C with the same settings as shown *2.3*. At specific moments of the mineralisation, the solution was taken out and then immediately transferred into an ice bath and cooled for 5 minutes. 10 µL of the well-mixed solution was deposited immediately on a TEM grid. During the aliquot addition, the grid was placed on a dust-free paper towel in order to quickly withdraw the liquid. After five additions, the grid was dried overnight and then analysed by TEM. STEM/EDX characterisations were performed on a JEOL 2100 Plus microscope (LaB6 gun) operating at 200 kV. Mapping and EDX quantification of O, Ca, P and Mg elements were collected by combining HAADF-STEM (high angular annular dark field scanning transmission electron microscopy) and EDX Oxford detector (SDD 80 mm^2, Oxford Aztec software) using the Kα characteristic signals of these 4 elements.

3 Heterogeneous mineralization over layer-by-layer assemblies

3.1 Layer-by-Layer assembly

Layer-by-layer assemblies were constructed on silicon wafers (100) which were cut into 0.7 × 0.7 cm^2 using a diamond cutter then cleaned using a piranha solution (H_2SO_4 (96%)/H_2O_2 (30%): 1/3, v/v.). The surfaces were thoroughly washed with ultrapure water followed by drying under nitrogen flow. All solutions were freshly prepared in ultrapure water.

Build-up of (Col/HA) multilayers

The build-up of $(Col/HA)_n$ multilayers was performed with four different polyelectrolyte solutions at pH 4.5 at ambient conditions; PEI, PSS, HA (1 mg/mL) and Col (0.1 mg/mL). The subscript 'n' means the number of constructed bi-layers. The Si wafers were firstly dipped in solutions PEI and PSS for 10 minutes each to build anchoring layers (PEI/PSS). Then, the surfaces were immersed in Col and HA solution for 30 min and 15 min alternatively until the construction of three bilayers, $(Col/HA)_3$. After every immersion, the surfaces were rinsed by dipping three different water baths at pH 4.5 for 2 minutes each. After the formation of $(PEI/PSS)(Col/HA)_3$, the surfaces were moved into an aqueous crosslinking solution containing EDC (30 mM)/NHS (50 mM) at pH 4.5. The surfaces were maintained in the solution overnight on an agitator at room temperature. The surfaces were rinsed by immersing them in ultrapure water at pH 7.4 for 10 minutes, two times. Then $(PAH/ALP)_5$ multilayers were cumulated on $(PEI/PSS)(Col/HA)_3$ multilayers with a procedure below, 4.1.2.

Build-up of (PAH/ALP) multilayers

The build-up of $(PAH/ALP)_5$ multilayers on Si wafer or $(PEI/PSS)(Col/HA)_3$ multilayers were conducted with two solutions at pH 7.4 at 37 °C; PAH (1 mg/mL) and ALP (0.1 mg/mL, by dilution of 1 mg/mL aliquot stored in the freezer). The surfaces were immersed in PAH and ALP solution for 15 and 30 minutes by turns up to the construction of five bilayers. Between each solution, samples were rinsed by dipping them in three different water baths at pH 7.4 for 2 minutes.

3.2 Mineralization of multilayers

The surfaces with $(PAH/ALP)_5$ or $(Col/HA)_3(PAH/ALP)_5$ multilayers were immersed in a mineralization solution containing Sub-Mg (7 mM) and $CaCl_2$ (11.4 mM) at pH 7.4 at 37 °C. At different mineralization times (from 1 hour to 1 week), samples were collected and rinsed using three different water baths at pH 7.4 and 37 °C for 2 min each and dried under nitrogen gas flow.

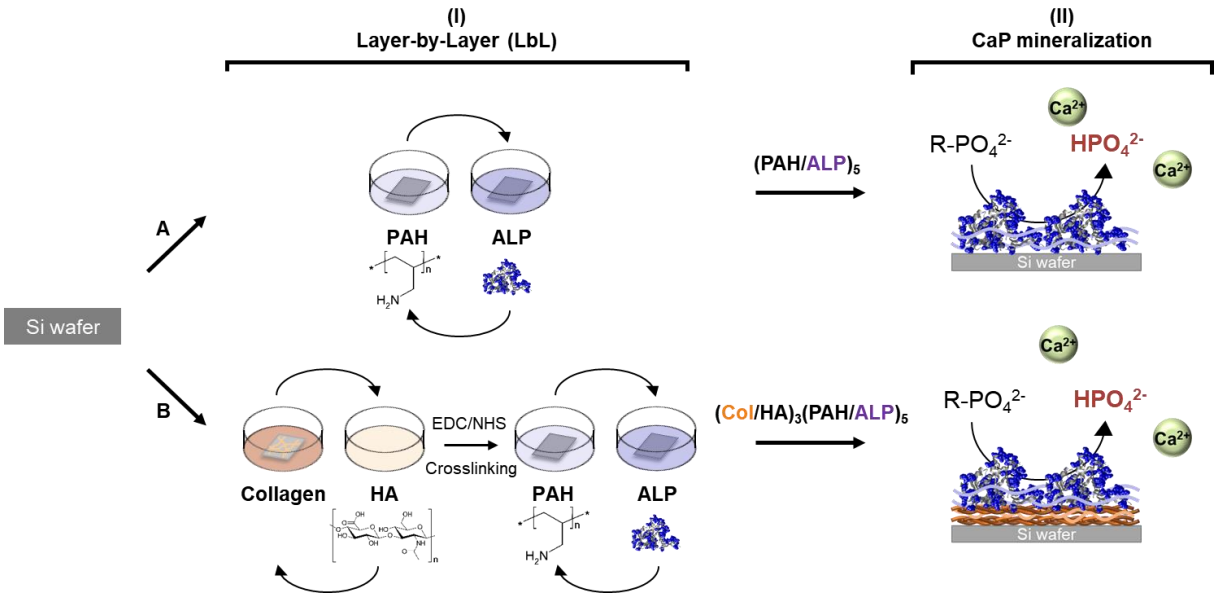

Scheme 2. 1 Procedure for the generation of multilayers. Step (I): build-up of multilayers of $(PAH/ALP)_5$ (pathway A) and $(Col/HA)_3(PAH/ALP)_5$ (pathway B) by alternative immersion in different polyelectrolyte solutions. Step (II): enzyme-assisted mineralization by put multilayers in the aqueous mineralization solution containing substrate for enzymes and Ca^{2+} ions.

3.3 Enzymatic activity of ALP within multilayers

The catalytic activity of ALP in different multilayers and in solution was explored using 4-nitrophenyl phosphate (pnpp) as shown previously 2.2.

Specific activity of free ALP

The catalytic activities of ALP in the presence of different polyelectrolytes (Col 0.1 mg/mL, HA 1 mg/mL, PAH 1 mg/mL) were investigated in aqueous solutions to discover their effects on ALP activities. A solution containing pnpp and polyelectrolytes was firstly prepared then added variable amount of ALP (5, 10, 50, 70, 100 µg/mL).

However, in this thesis, the result with the addition of PAH is not shown as it was unable to measure the progress of absorbances as it formed white solids by mixing pnpp and PAH.

Activity of immobilized ALP

The surface with multilayers was immersed in 2 mL of pnpp solution (7 mM, pH 7.4, 37 °C) in a 4 mL transparent plastic cuvette (optical path length: 1 cm). The progress of absorbance at 410 nm caused by the production of pnp by enzymes on the surface was measured by time for 30 minutes. A calibration curve was obtained by measuring absorbances at 410 nm of pnp

concentration from 200 µM to 10 µM (pH 7.4, 37 °C). The linear increase of pnp concentration by time is defined as the enzymatic activity with a unit $\mu M \cdot min^{-1}$.

Residual activity of ALP within multilayers

The operational stability of enzymes embedded within the LbL multilayers was evaluated by measuring the residual activities periodically at intervals of 30 min over a period of 3.5 h at 37 °C. Between measurements, samples were washed 3 times with ultrapure water.

3.4 Characterization of multilayers

3.4.1 Atomic force microscopy (AFM)

AFM is a scanning probe microscopy, firstly proposed by binning *et al.* in 1986 [6], which overcomes the resolution limits of the diffraction limit of light by adapting a sharp probe to scan the sample surface in a raster pattern. It enables precise and non-destructive measurements at the nanoscale, providing access to the topographic, electrical, magnetic, chemical, optical and mechanical properties of a surface with wide range of materials over a wide temperature range and in various environments, namely air, liquids or ultra-high vacuum. The ability to perform measurements in liquid and room temperature environments makes AFM a powerful tool for probing biological systems. AFM is performed using a tip (probe) attached to a lever microfabricated in silicon nitride (Si_3N_4) and whose radius of curvature can vary in nanometer scales. Thus, the lateral resolution (in x, y) depends on the radius of the tip (in the order of a nanometer), whereas the spatial resolution (in z) is of the order of a tenth of a nanometer. For the measurement, a sample is placed on a piezoelectric scanner which controls the lateral (x, y) and vertical (z) position of the prove over the sample (or the sample under the probe). A laser beam focused on the cantilever tracks the deflection of the cantilever relative to the surface morphology through the position of the laser in a photodiode (Figure 2.3 A). AFM can be used in imaging or force spectroscopy, depending on the specific application required.

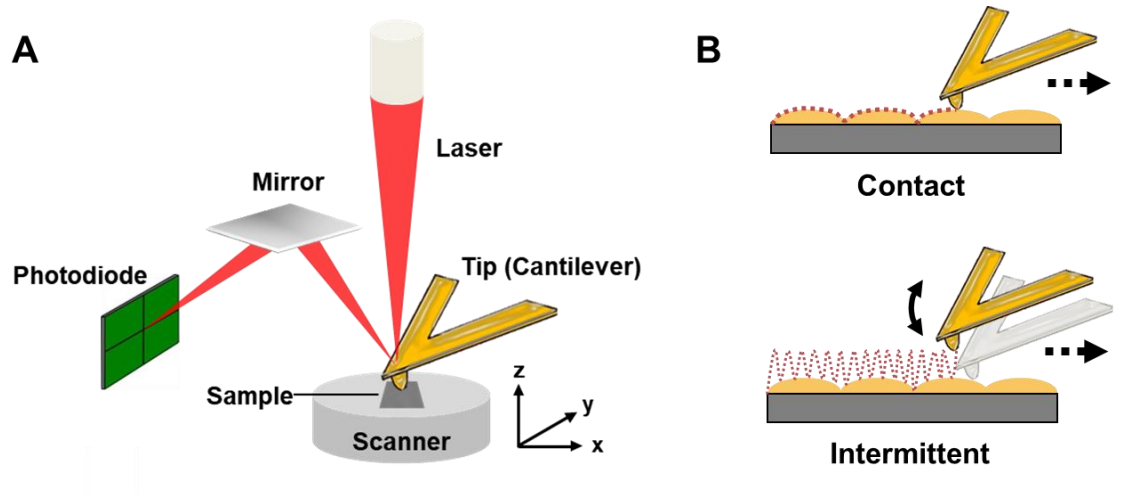

Figure 2. 3 Illustration of AFM analysis (A) instrumentation (B) imaging mode.

Principle of AFM Imaging

The imaging ways can be roughly divided into two modes (Figure 2.3 B):

(i) The contact mode in which the tip is brought into contact with the surface of the sample with a tracking force kept constant during the scan,

(ii) the intermittent mode, in which the cantilever oscillates at a given frequency, as, for example, in the Tapping ® mode (~ resonance frequency) or the peak force tapping ® mode (< resonance frequency).

It should be noted that the contact mode can lead to deterioration of the sample or distortion of the images (friction movement). Intermittent mode solves this problem since the tip is in intermittent contact with the sample surface.

In this thesis, AFM is used to investigate surface morphology of enzyme-assisted mineralization on multilayers. The peak force tapping mode is only used for imaging due to the precise control of forces which enables the high-resolution imaging.

AFM imaging in a certain mineralization time

The morphology of mineralized multilayers was imaged using a commercial AFM (NanoScope VIII MultiMode AFM) and a triangular silicon nitride cantilever (SNL-10). Before each measurement, the spring constants of the cantilevers were measured using the thermal noise method, yielding values ranging from 0.11 to 0.15 N/m. The images were recorded in different

scales (10×10, 5×5, 2×2 μm^2) in different zones. The root means square roughness (R_{rms}) was calculated on 2 × 2 μm^2 images and averaged from 3 different images.

Real-time imaging of mineralization

Real-time in situ monitoring of CaP mineralization on $(Col/HA)_3(PAH/ALP)_5$ multilayers was performed using the commercial AFM (NanoScope VIII MultiMode AFM) equipped with a fluid cell (MTFML-V2, Bruker Nano Inc., Nano Surfaces Division, Santa Barbara, CA.). The use of fluid cell allows to apply the mineralization solution on the surface without drying and to monitor mineralization from very early stages. Before each monitoring, the fluid cell was thoroughly cleaned using 2 % SDS solution and ultrapure water followed by drying using nitrogen gas flow. A commercial cantilever (SNL-10, position A) was prepared by immersing it in water overnight and measuring its spring constant using the thermal noise method showing values ranging from 0.32 to 0.66 N/m. A surface with $(Col/HA)_3(PAH/ALP)_5$ multilayers was fixed on a steel sample puck using adhesive tape. A small water drop (100 µL) was placed on the sample and around the cantilever then checked the surface morphology before mineralization. After the liquid on the surface was removed using a pipette then applied 100 µL of mineralization solution containing Sub-Mg (7 mM) and $CaCl_2$ (11.4 mM) at pH 7.4 at room temperature (t = 0). The removal of liquid and application of the mineralization solution was repeated two times very quickly to minimize the effect of dilution by MilliQ presented before. The fluid cell equipped with the cantilever was immediately reinstalled and maintained until voltage meters got stable (up to 10 minutes). The cantilever should be placed on the region with collagen fibrils but without any other noticeable objects then engaged on the surface. The monitoring started and was maintained for several hours in the same regions using offsets according to the drift of scans. The obtained images were flattened using the software Nanoscope analysis 1.9 (Bruker Nano Inc., Nano Surfaces Division, Santa Barbara, CA.) and generated as a movie by time.

3.4.2 XPS

X-ray photoelectron spectroscopy (XPS) is a quantitative technique that is commonly used to provide the elemental composition of a material's surface. Note that all elements can be detected except hydrogen and helium. This analysis technique is based on the principle of photoemission. XPS involves kinetic energy measurements of photoelectrons emitted from the near surface (1-10 nm) under irradiation. Indeed, the surface atoms irradiated by the X-rays eject core electrons, i.e. electrons from the K and L levels, with a certain kinetic energy. These

light-emitted electrons undergo inelastic collisions with the atoms of the sample as they move towards the surface. With each inelastic collision, their kinetic energy decreases. Only those coming from the near surface, i.e. < 10 nm, do not undergo an inelastic collision and therefore contribute to the peaks. The inelastic mean free path, λ, depends on the kinetic energy of the light-emitted electron and the density of the matrix. The contribution to the intensity decreases exponentially with depth: 63% of the signal comes from a layer of thickness equal to λcosθ, 86% from a layer of thickness 2λcosθ, 95% from a layer of thickness 3λcosθ, with θ the angle between the detector and the normal to the surface. Since the inelastic mean free path is generally between about 1.5 and 3.3 nm, XPS probes a surface layer whose thickness can reach 3λ cosθ, c.a. about 5-10 nm. Depending on the depth, some photoemitted electrons which undergo an inelastic collision also reach the detector but with a lower kinetic energy. They thus contribute to the bottom of the spectrum. Additionally, in the case of an insulating material, such as biological tissue, the photoemission of electrons from the sample surface creates a positive charge on the sample surface. The attraction of the charged surface therefore decreases the kinetic energy of the emitted electron, which leads to a broadening of the peaks. To overcome this charge effect, a low energy electron gun is used to neutralize the surface and maintain a relatively stable surface charge during the analysis. The emitted electrons are then collected by a hemispherical analyzer. The number of ejected electrons is plotted against their kinetic energy, yielding a photoelectron energy spectrum. In fact, electrons of different energies follow different paths through the detector, which makes it possible to differentiate them according to their kinetic energy. Each element thus presents characteristic peaks in the XPS spectrum which can be translated into binding energy. The latter is determined according to the energy conservation equation:

$$E_{\mathrm{B}} = E_{\mathrm{Al}} - (E_{\mathrm{k}} + \Phi_w)$$

E_{B}: Electron binding energy

$E_{\mathrm{Al}} = h\nu = 1486{,}6$ eV

E_{k}: Kinetic energy measured by the detector

Φ_w: Spectrometer work function

The latter corresponds to the minimum energy required to bring an electron from the zero level of attraction by the sample to the entrance of the hemispherical analyzer.

The elemental composition and identification and chemical environment of an element can be obtained from the exact measurement of the position of the peaks and their separations in binding energy, E_B. The intensity of the recorded peaks makes it possible to quantify the surface elements and the chemical environments. As photoelectron binding energy is influenced by electron density, shifts in peak position, E_B, reflect changes in the chemical environment of the element of interest. The decomposition of the peaks thus makes it possible to provide information on the chemical nature of the organic compounds and offers a certain selectivity in the analysis of biological tissues.

XPS analyses were performed using an ESCA+ spectrometer (Omicron Nano-Technology) with a monochromatic aluminum X-ray source (14 kV power, 20 mA current) and MCD 128 channeltron detector. The charge stabilization on these insulating samples was ensured using a CN10 device operating at 5.0 µA emission current (0.30 eV beam energy). Measurements were performed in the sweep mode, yielding an analyzed area with an average diameter of 1 mm. A pass energy of 20 eV was used for narrow scans. Under these conditions, the full width at half maximum (FWHM) of the Ag 3d5/2 peak of clean silver reference sample was about 0.9 eV. The pressure in the analysis chamber was around 10-10 Torr. The photoelectron collection angle, θ, between the normal to the sample surface and the analyzer axis was 45°. The following sequence of spectra was recorded: survey spectrum, C 1s, N 1s, O 1s, Mg 2p, P 2p, Ca 2p, Si 2p and C 1s again to check the charge stability during the analysis and the absence of sample degradation due to the exposure to X-rays. XPS peaks were referenced to the C 1s peak due to carbon bound to only carbon and hydrogen at 284.8 eV. The data treatment was performed with CasaXPS software (Casa Software Ltd, Teignmouth, U.K.). Molar fractions were calculated using peak areas normalized according to Scofield factors.

3.4.3 SEM

Mineralized multilayers were imaged using a scanning electron microscope (SEM, FEI Quanta FEG 250, voltage 20 KV) coupled with an energy dispersive X-ray spectrometer (EDS, XFlash 6130, Bruker). For a better image contrast, samples were metallized by platinum sputtering.

4 References

1. Colaço, E., et al., *Calcium phosphate mineralization through homogenous enzymatic catalysis: Investigation of the early stages.* Journal of Colloid and Interface Science, 2020. **565**: p. 43-54.
2. Xu, R., *Progress in nanoparticles characterization: Sizing and zeta potential measurement.* Particuology, 2008. **6**(2): p. 112-115.
3. Ford, N.C., *Light Scattering Apparatus*, in *Dynamic Light Scattering: Applications of Photon Correlation Spectroscopy*, R. Pecora, Editor. 1985, Springer US: Boston, MA. p. 7-58.
4. Berne, B.J. and R. Pecora, *Dynamic light scattering: with applications to chemistry, biology, and physics*. 2000: Courier Corporation.
5. Williams, D.B. and C.B. Carter, *The Transmission Electron Microscope*, in *Transmission Electron Microscopy: A Textbook for Materials Science*, D.B. Williams and C.B. Carter, Editors. 2009, Springer US: Boston, MA. p. 3-22.
6. Binnig, G., C.F. Quate, and C. Gerber, *Atomic force microscope.* Phys Rev Lett, 1986. **56**(9): p. 930-933.
7. Janshoff, A., et al., *Force Spectroscopy of Molecular Systems—Single Molecule Spectroscopy of Polymers and Biomolecules.* Angewandte Chemie International Edition, 2000. **39**(18): p. 3212-3237.
8. Zuo, J. and H. Li, *Two-Molecule Force Spectroscopy on Proteins.* ACS Nano, 2023. **17**(8): p. 7872-7880.
9. Ebner, A., et al., *A New, Simple Method for Linking of Antibodies to Atomic Force Microscopy Tips.* Bioconjugate Chemistry, 2007. **18**(4): p. 1176-1184.

Chapter 3.
Enzyme-assisted mineralization in the homogeneous phase

ALP is the most important enzyme which catalyzes the dephosphorylation of a phosphate ester group producing an inorganic phosphate in ECM. It is a key to mimicking homeostasis on the degree of mineralization and phosphate ions in situ. In this chapter, enzyme-assisted mineralization is performed in a homogeneous phase by introducing ALP in a solution containing calcium ions and substrates of enzymes. The mineralization in solution is monitored by light scattering techniques. Kinetic parameters regarding nucleation and growth are driven from the monitoring. Based on the result, it is illustrated how the modulation of enzymatic activity and the introduction of a divalent ion differ in the mineralization process.

This work is the subject of an article published on 3 April 2023 - Colloids and Surfaces B: Biointerfaces volume 226, 113290, https://doi.org/10.1016/j.colsurfb.2023.113290

1 Introduction

Biomineralization is a fascinating biological process involving sophisticated biochemical and physicochemical regulators, which provides to live organisms a remarkable ability to control the mineral deposition in time and in space as shown in Chapter 1. In this context, a particular interest has been dedicated to the mechanism of formation of CaP, the major constituent of mineralized tissues of vertebrates. Widespread studies have been conducted in abiotic supersaturated solutions containing CaP precursor ions at different supersaturations, providing insights into the thermodynamics and kinetics of phase transition processes [1-4]. While abiotic media do not take into account the intricacy of biological systems, these investigations showed a great interest particularly from the fundamental point of view, such as in the attempts to reconcile "classical" and "non-classical" mineralisation pathways [5]. The gap between abiotic and biotic features is essentially associated with the compartmentalisation of biological systems and the homeostatic balance involved in biomineralization, which both contribute to the regulation of the spatiotemporal mineral deposition.

In this chapter, it is to aimed to bring the homeostasis regulating the phosphate ions in situ by incorporating an enzyme which can generate phosphate ions in situ. In the previous research from our group, it showed the possibility to initiate CaP mineralization via a homogeneous enzymatic catalysis system, where calcium ions and an ALP substrate were introduced in an aqueous solution, simulating physiological conditions [6]. Primary observations have suggested the existence of an enzyme-assisted mineralization pathway that can be modulated through the catalytic activity of enzymes. Importantly, they highlighted the interest of biomimetic enzymatic systems, which offer an *in situ* time-controlled generation of CaP ion precursors. This is particularly important because mineral phase transformations are mostly kinetically-controlled processes [7]. A temporal control of the mineralization process is made possible by modulating factors influencing the enzyme-catalyzed reaction.

As we explained in a section *4.1*, chapter I, an enzymatic model approach allows the introduction of a supersaturation parameter, σ, the evolution of which is not monotonous as it would be the case in non-enzymatic systems. Indeed, it results here from the interplay between the enzyme activity and the kinetics of the mineralization process, as it is depicted in Scheme 3.1. When the evolution of the supersaturation does not depend only on the extent of the reaction of mineralization, a better control of the reaction conditions can be obtained, especially through the tuning of the enzyme activity.

Accordingly, a real-time monitoring is highly required for probing such a biomimetic system and unravel the mechanism by which CaP crystals nucleate and grow. The use of a limited number of techniques has been reported in the literature to study the temporal evolution of this kind of process, as probing 10 to 100 nm scale in solution is a thorny task. The main approach consists in monitoring the content of the solution by potentiometry (with a pH or a specific Ca^{2+} probe) [5, 8, 9]. Less frequent studies of the hydrodynamic diameter of the minerals by dynamic light scattering and zeta potential by electrophoretic measurements are also reported, but, in most articles, the measurements are performed at specific and discrete times, not continuously [5], or limited by experimental conditions [10]. Electron micrographs of samples collected at various times are also often presented, sometimes using cryoscopic method [11] or, more recently, liquid cell [12]. These studies brought numerous valuable inputs to the understanding of the CaP biomineralization processes, but they need to be guided by real-time *in situ* experiments to ensure the representativeness of the studied phenomena, as they introduce substantial experimental biases and an arbitrary temporal division. Also, they cannot bring quantitative information that are necessary for example to study the kinetics of the process.

In the present study, a real-time monitoring of CaP mineralization is investigated from a fresh perspective. For this purpose, we use the enzyme-assisted mineralization system and explore light scattering-based techniques to probe real-time events associated with CaP mineralization. We show here that the use of an original combination of static and dynamic light scattering techniques allows the novel possibility of extracting relevant kinetic parameters associated with the nucleation and growth of CaP particles, which provide new insights into the way by which enzymes direct the mineralization process. A particular attention is dedicated to (i) the role of the enzymatic activity in the mineralization process, (ii) the inhibitory role of magnesium ions in the crystallization process and (iii) the way to explore real-time characterisation through scattering techniques to identify key intermediates.

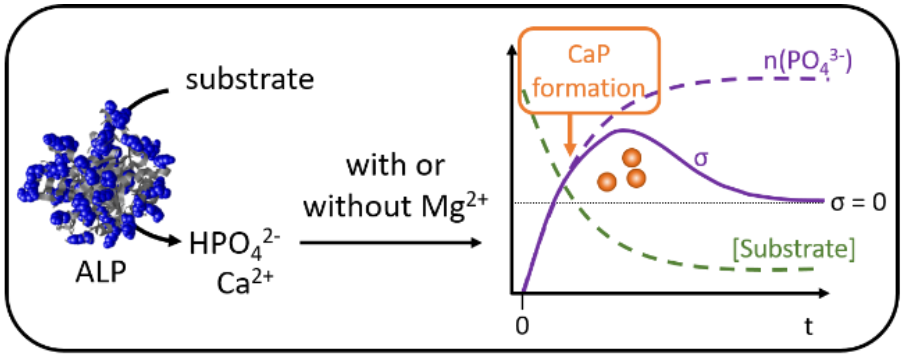

Scheme 3.1. Enzyme-assisted mineralization. The ALP enzyme catalyses the transformation of substrate molecules that leads to the release of HPO_4^{2-} ions in solution that can then react with calcium ions to form CaP minerals, when the supersaturation σ reaches a critical value.

2 Results and discussion

2.1 Monitoring the mineralization in real-time

A first mineralization experiment was performed on a system prepared with the initial substrate concentration $[Sub]_0$ = 3.0 mM and without Mg^{2+} ions according to the procedure described in section *2.1*. As soon as the three main components (Ca^{2+} ions, Sub and ALP) were mixed together, phosphate ions started to be released in solution and then calcium phosphate began to form. The evolution of the pH was recorded and the hydrodynamic diameter of the objects dispersed in solution was monitored in a separate duplicated experiment. The results are presented in Figure 3.1A. The plot of the hydrodynamic diameter *versus* time shows a very quick formation of scattering objects that exhibit a diameter around 210 nm. Complementary DLS measurements show that these objects cannot be found for dispersions of enzymes containing either Ca^{2+} ions or Sub molecules, i.e. when the mineralization does not take place. Then, after a slight evolution of the average size, a much steeper growth can be observed for the dispersed objects after approximately 40 min. Eventually, after a few minutes, the scattering of the solution is dominated by objects that are too big (above 1.00 µm) to be accurately characterised by DLS.

The evolution of the pH as a function of time displays, first, a rapid decrease down to pH = 6.8. This evolution is then followed by another drastic drop after 35 minutes down to pH = 6.1. These decreases of the pH are expected when calcium phosphate particles are formed or when particles are subjected to a phase transition, as this quantity measures the release of protons in solution [4].

The same trend was observed at a higher concentration of substrate, $[Sub]_0$ = 7.0 mM, and without Mg^{2+} ions, except that the sudden increase of the hydrodynamic diameter occurred earlier, after approximately 20 min (Figure 3.1B).

In the presence of Mg^{2+} ions ($[Sub]_0$ = 7.0 mM, $[Mg^{2+}]$ = 5.0 mM), the duration after which a plateau is observed by DLS, at about 250 nm, was significantly longer compared to the situation without Mg^{2+} (see Figure 3.1C). Moreover, even though the sudden increase of the hydrodynamic diameter was still associated to a drastic drop of pH, a noticeable gap was observed between the sudden increase of the hydrodynamic diameter (about 115 min) and the drop of pH (about 85 min).

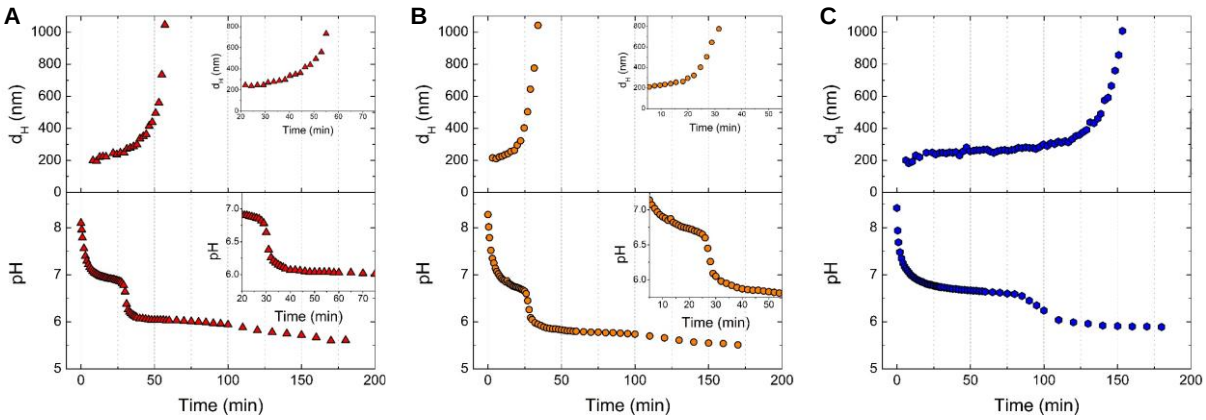

Figure 3.1. Hydrodynamic diameter and pH measured as a function of time during the enzyme-induced mineralization conducted at 37 °C, at (A) $[Sub]_0$ = 3.0 mM, (B) $[Sub]_0$ = 7.0 mM, and (C) as such with the addition of $MgCl_2$ at $[Mg^{2+}]_0$ = 5.0 mM. Inserts: zooms of the areas where the steep increase of the hydrodynamic diameter and the pH drop occur.

Thus, these measurements allowed to derive a correlation between the increase of the size of the particles dispersed in solution observed by DLS and the drop of the pH, but a delay can be observed between the two events, depending on the experimental conditions, particularly in presence of Mg^{2+} (Figure 3.1). As a matter of fact, one must note that the information recorded by both kinds of techniques, i.e. potentiometry *versus* light scattering, are significantly different. On the one hand, potentiometry measurements allow one to observe changes in the composition of the solution that give information about the chemical changes in play. On the other hand, DLS measurements are sensitive to the variation of size of the object dispersed in solution. According to the different nature of these techniques, the detection of the formation of bigger objects can then be expected to be detected by DLS at slightly different moments from their modification in chemical composition, which is, indeed, what can be observed in Figure 3.1A.

In a nutshell, these concurrent measurements allow to identify two main regimes in the studied mineralization process:

1) the formation of objects with a nearly constant size characterised by a hydrodynamic diameter of approximately 200 to 300 nm until pH = 7.0, during the first step of the process.

2) the drastic growth or the rapid formation of micron-sized particles objects, starting to appear quickly after the first step of the process as it can be seen by DLS, whereas the pH drops to 6.0, then continues to decrease progressively.

More direct evidences regarding the early stages of CaP mineralization are given by the observation of intermediate compounds taken at characteristic times that correspond to the different mineralization regimes indicated by DLS (Figure 3.2). At the substrate concentration $[Sub]_0$ = 3.0 mM and without Mg^{2+} ions, TEM micrographs showed the formation of amorphous globular particles, typical of ACP [12], after 30 min of mineralization, with a mean diameter of 88 ± 25 nm (Figure 3.2A). Their amorphous feature was confirmed by the diffuse diffraction observed in the SAED pattern (data not shown). These particles are wholly composed of CaP compounds, as confirmed by the elemental maps made with EDX for phosphorus, calcium, oxygen and magnesium (Figure 3.3A), with a molar concentration ratio Ca/P = 1.30 (Figure S3.3A and B, Supporting Information). The morphology of these particles changed noticeably after 60 min, showing a stacking of platelet-shaped particles typical of hydroxyapatite (Figure 3.2B). This is confirmed by their composition, as indicated by elemental maps (Figure 3.3B), and their crystallographic structure as indicated by SAED pattern (Figure 3.3C). Chemical maps showed the presence of the characteristic elements (Fig. 3.3B), with a molar concentration ratio Ca/P = 1.20 (Figures. S3.4A and B, Supporting Information).

In the presence of Mg^{2+} ions ($[Sub]_0$ = 7.0 mM, $[Mg^{2+}]$ = 5.0 mM), the situation was significantly different. First, the amorphous globular particles that form at early stage, observed here at about 90 min, showed a slightly higher mean diameter (149 ± 16 nm, see Figure 3.2A') and, more importantly, the presence of Mg in a significant amount (Figure 3.3D). The molar concentration ratios Ca/P and Mg/P were 1.27 and 0.35, respectively (Figures S3.3C and D, Supporting Information). After 162 min of mineralization, TEM micrographs showed the formation of poorly crystalline particles, sometimes with a discernible core-shell structure (Figure 3.2B'), with a mean diameter around 96 ± 17 nm, and exhibiting filamentous

nanostructures in the interparticle space. They are composed of CaP compounds but include a significant amount of Mg (Figure 3.3E).

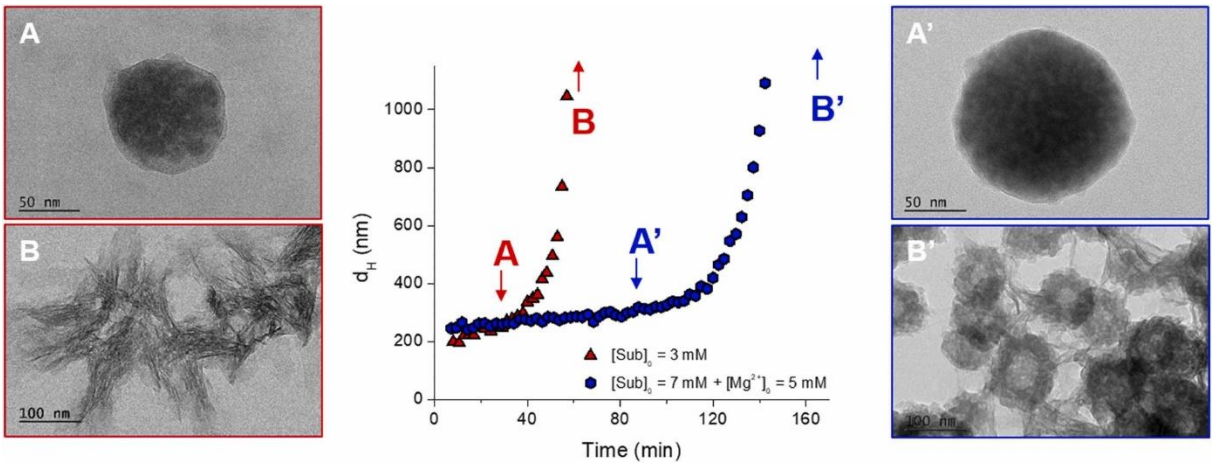

Figure 3.2. TEM micrographs of CaP intermediate compounds taken at characteristic times indicated by DLS data. CaP particles formed; (A, B): at $[Sub]_0$ = 3.0 mM without Mg^{2+} after (A) 30 and (B) 60 min (as indicated by arrows), or (A', B'): at $[Sub]_0$ = 7.0 mM with $[Mg^{2+}]_0$ = 5.0 mM after (A') 91 min and (B') 162 min (see arrows).

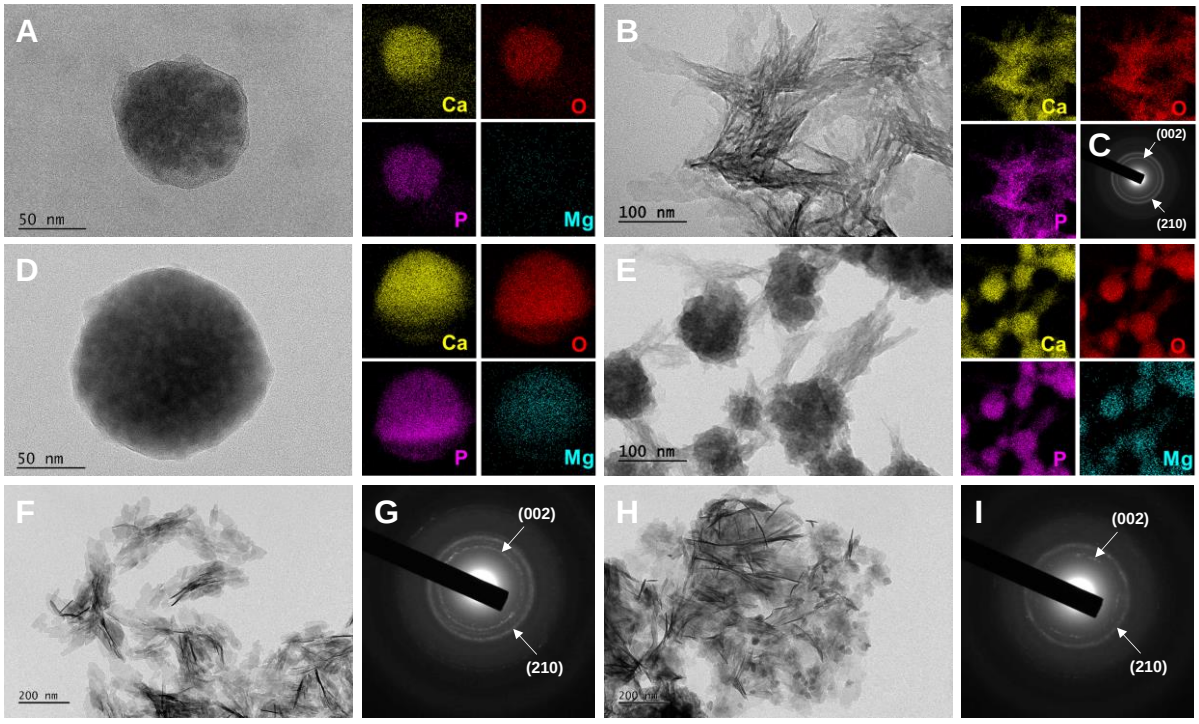

Figure 3.3. (A-E) TEM micrographs of CaP intermediate compounds and their corresponding elemental maps of phosphorus, calcium, oxygen and magnesium formed; (A, B, C): at $[Sub]_0$ = 3.0 mM without Mg^{2+}, after 30 min (A) and 60 min (B, SAED pattern of the compound is given in panel C), or (D, E): at $[Sub]_0$ = 7.0 mM with $[Mg^{2+}]_0$ = 5.0 mM, after 91 min (D) and 162 min (E). (F-I): TEM micrographs and SAED patterns of CaP particles obtained after 24 h of mineralization (F, G): at $[Sub]_0$ = 3.0 mM without Mg^{2+} or (H, I): at $[Sub]_0$ = 7.0 mM with $[Mg^{2+}]_0$ = 5.0 mM.

Further mineralization led after 24 h to the formation of well-defined platelet-shaped hydroxyapatite for the sample without Mg^{2+}, as shown by TEM micrographs and SAED pattern (Figures 3.3F and G). In the presence of Mg^{2+}, the particles obtained after 24 hours of mineralization also displayed the typical platelet shape and the diffraction pattern characteristic of hydroxyapatite (Figure 3.3H and I). However, TEM micrograph showed, in addition to platelets, the presence of smaller globular, and probably amorphous or poorly crystalline particles (Figure 3.3H).

The above observations revealed the strong link between the hydrodynamic size of the mineralized particles, probed during their formation, and the evolution of the pH of the solution. They also showed that DLS offers a straightforward way to identify characteristic times that correspond to key intermediates in the enzyme-assisted mineralization pathway. Accordingly, in the following, a particular attention will be devoted to thoroughly exploring light scattering data to investigate the role of two main components of the mineralization system: (i) the enzyme substrate that modulates the kinetics of the enzyme-catalyzed reaction, and (ii) the presence of Mg^{2+} ions, expected to impact the kinetic of the crystallization process.

2.2 Influence of the initial substrate concentration, $[Sub]_0$

The formation of CaP particles was studied with different initial concentrations of substrate, $[Sub]_0$ = 3.0, 4.0, 5.0, 6.0 and 7.0 mM. The main results are given in Figure 3.4A-C. The activity was found to depend on the initial concentration of substrate, $[pnpp]_0$, in the studied conditions and the range explored here (Figure 3.4A). Indeed, it can easily be observed that the enzyme activity increased noticeably when $[pnpp]_0$ increases, as expected.

The influence of $[Sub]_0$ on the CaP mineralization was monitored by DLS (Figure 3.4B) and by SLS (Figure 3.4C). The evolution of the hydrodynamic diameter as a function of time for different values of $[Sub]_0$ display all the same trend, where a first plateau around 210 nm is reached initially and then followed by a drastic increase after a certain delay (Figure 3.4B). Interestingly, the delay after which this sudden growth increases when $[Sub]_0$ decreases.

In order to compare more accurately the various curves, the evolution of the hydrodynamic diameter (d_H) was modelled by curves using the following generic equation (1):

$$d_H = d_0 + A \times e^{k_G(t-t_0)} \quad (1)$$

In this equation, d_0 corresponds to the size of objects rapidly formed that were found for all $[Sub]_0$. Accordingly, the same value of d_0 was used for the curves obtained for different values of $[Sub]_0$. A is a pre-exponential factor that reflects the amplitude of the exponential increase,

k_G, can be related to the rate of the size increase and t_0 corresponds to the retardation time after which the minerals start to grow exponentially. For this modelling, d_0 and A have been arbitrarily fixed to be equal for the different $[Sub]_0$, whereas the values of k_G and t_0 were determined through a least square fitting method.

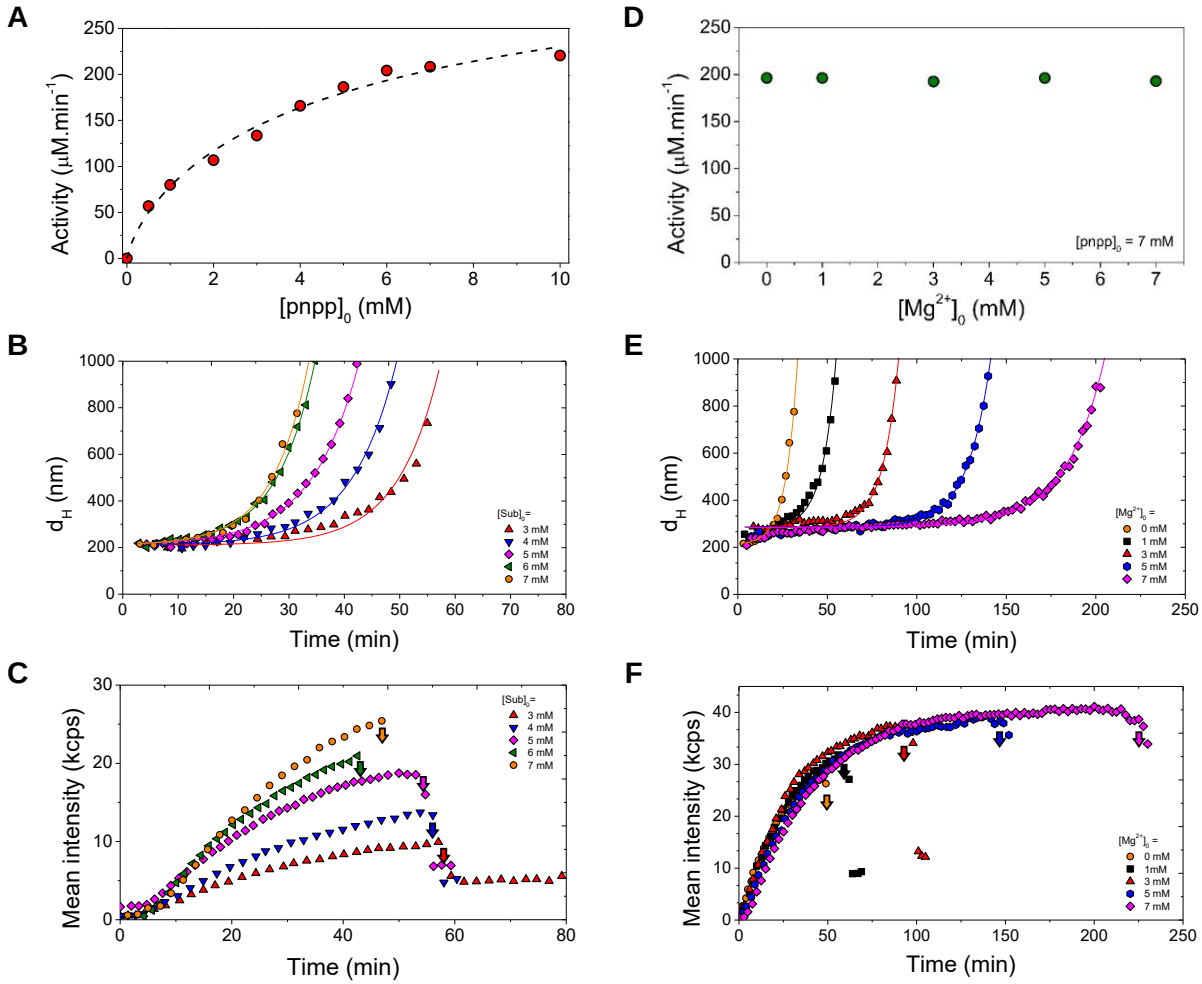

Figure 3.4. (A, D) Catalytic activity measurements of ALP in aqueous solution at 37°C determined from the kinetics of pnp production over time using pnpp as a substrate at different concentrations (see Figure S1, Supporting Information). Dashed line in panel A corresponds to fitting using the classical Michaelis-Menten equation. (B, E) DLS (hydrodynamic diameter versus time) and (C, F) SLS (mean intensity versus time) measurements performed (B, C) at different $[Sub]_0$ values, and (E, F) at $[Sub]_0$ = 7.0 mM, while varying $[Mg^{2+}]_0$, as indicated.

Table 3.1 displays the different set of parameters adjusted to plot the continuous lines in Figure 3.4B. The main observations extracted from these values can be summarised as follows.

- For all the $[Sub]_0$ values, a significant retardation time, t_0, can be observed, after which the size of the objects dispersed in solution starts to increase drastically. This characteristic

time increases when the $[Sub]_0$ value decreases (Table 3.1), corresponding to a decrease of the enzymatic activity (see Figure 3.4A).

- The growth rate, measured here through the value of k_G, does not seem to be significantly influenced by the phosphate ion rate of release (Table 3.1), reflected by the enzymatic activity: another limiting step seems, thus, to prevail at this stage of the mineralization.

- The value of d_0 corresponds to a colloidal object that is very rapidly formed (it is already present during the very first DLS measurement). Even if it is arbitrarily fixed in the model used according to equation (1), it appears that this size corresponds to a similar behaviour during the first stage of the mineralization that is observed for each $[Sub]_0$ value.

Table 3.1. Model corresponding to the mechanism of formation of CaP particles for different values of $[Sub]_0$ and $[Mg^{2+}]_0$. (*) Arbitrarily fixed parameters when fitting DLS curves using the equation: $d = d_0 + A \times \exp(k(t - t_0)$ and (**): slopes obtained when fitting SLS curves using a linear regression during the first 30 min.

$[Sub]_0$ (mM)	d_0 (nm)*	A (nm)*	k_G (min^{-1})	t_0 (min)	k_N (min^{-1})**
3			0.13	29.7	0.26
4			0.13	20.0	0.36
5	210	20	0.12	11.4	0.53
6			0.14	9.3	0.75
7			0.15	9.5	0.86
$[Mg^{2+}]_0$ (mM)	d_0 (nm)*	A (nm)*	k_G (min^{-1})	t_0 (min)	k_N (min^{-1})**
0	210	20	0.15	9.5	0.86
1			0.13	27.8	0.85
3	285	20	0.11	58.2	0.87
5			0.08	94.8	0.73
7			0.05	127.9	0.72

Complementary information regarding the enzyme-assisted mineralization process is provided by SLS measurements. The physical quantity reported in Figure 3.4C is the mean scattered intensity, which is directly linked to the amount of scattering materials in solution.

In this series of experiments, the scattered intensity displays the same trend as a function of time: a continuous increase is observed until the measured intensity drops suddenly (the drops

for each series are pinpointed by arrows in Figure 3.4C). This abrupt decrease is characteristic of a drastic change in the structure of the solid dispersion (aggregation leading to fast sedimentation, tremendous increase of multiple scattering, etc.), that can correlate with a sudden growth of the scattering objects in solution.

The plots of the mean intensity as a function of time follow a different evolution for each $[Sub]_0$ value: the higher the concentration, the faster the increase of the intensity. The rate of this increase can be characterised by the slope, k_N, of the initial evolution of the scattered intensity when it starts to increase, through a linear regression, and is reported in Table 3.1 for the different conditions. The scattered intensity being characteristic of the amount of mineral that is formed, one can then observe that the higher the enzymatic activity, the higher the rate of the mineral formation (see k_N values in Table 3.1).

2.3 Influence of the magnesium ion concentration: $[Mg^{2+}]_0$

The formation of CaP particles was also studied by maintaining stable the substrate concentration, $[Sub]_0$ = 7.0 mM, while varying the initial concentrations of magnesium ions, $[Mg^{2+}]_0$, which are known to be crystallisation inhibitors. Values of $[Mg^{2+}]_0$ = 0, 1.0, 3.0, 4.0, 5.0 and 7.0 mM were investigated, and the main results are given in Figure 3.4D-F. The enzyme activity was found to be independent of $[Mg^{2+}]_0$ in the studied conditions (Figure 3.4D), in contrast to previous studies, where Mg^{2+} ions were shown to stimulate ALP in different physicochemical conditions at concentrations ranging from 0.1 to 10 mM [13, 14]. This is due to the high concentration of substrate used in the present study, $[Sub]_0$ = 7.0 mM, at which the addition of Mg^{2+} appears to have a negligible effect on the catalytic activity.

These conditions allow, thus, the enzymatic activity to be kept fixed, while varying the concentration of magnesium ions. $[Mg^{2+}]_0$ is then expected to exclusively impact the crystallisation pathway. The influence of $[Mg^{2+}]_0$ on the mineralization was monitored by DLS (evolution of the hydrodynamic diameter with time, Figure 3.4E) and by SLS (evolution of the mean scattered intensity with time, Figure 3.4F). The evolutions of the hydrodynamic diameter as a function of time for different values of $[Mg^{2+}]_0$ display all the same trend, where a first plateau around 285 nm is reached initially and followed then by a drastic increase after a certain delay (Figure 3.4E). However, the delay after which this sudden growth happens increases when $[Mg^{2+}]_0$ increases. Following the approach described above, the evolution of the hydrodynamic diameter was modelled by curves derived from the generic equation (1). Table 3.1 displays the different sets of parameters adjusted to plot the continuous lines presented in Figure 3.4E. The main observations extracted from these values can be summarised as follows.

For all the $[Mg^{2+}]_0$ values, a significant retardation time, t_0, can be observed, after which the size of the objects dispersed in solution starts to increase drastically. This characteristic time increases when the $[Mg^{2+}]_0$ value increases.

- The growth rate, measured here through k_G, decreases significantly when $[Mg^{2+}]_0$ increases (Table 3.1).

- The value of d_0 = 285 nm corresponds to a solid that is very rapidly formed. Its size appears to be independent of $[Mg^{2+}]_0$ and is significantly higher than the one obtained for the $[Sub]_0$ series (ca. 210 nm).

- The plots of the mean intensity as a function of time follow remarkably the same master curve for each $[Mg^{2+}]_0$, even when no magnesium ions are introduced initially (Figure 3.4F). The only difference between these curves is the delay after which the intensity suddenly drops. As explained in 3.2, this can be related to the appearance of bigger minerals in the solution that precipitate and could modify drastically the scattering behaviour of the sample for example because of multiple scattering.

2.4 Mechanism of enzyme-assisted mineralization: Effect of $[Sub]_0$ versus $[Mg^{2+}]_0$

In this study, two different ways of tuning the process of enzyme-assisted mineralization were achieved by adjusting the initial concentration of either: (i) the enzyme substrate, $[Sub]_0$, which modulates the enzymatic activity, that is the phosphate ion rate of release, or (ii) magnesium ions, $[Mg^{2+}]_0$, known to stabilise the amorphous phase, thus delaying the CaP crystallisation process, as an inhibitor. The light scattering techniques, combing DLS and SLS measurements, showed a straightforward, yet powerful, way to extract relevant kinetic parameters, which quantifies the effect of these concentrations on the enzyme-assisted mineralization process:

- k_N, the rate at which the scattered intensity increases,

- t_0, the retardation time between the appearance of the first solids in solution and the growth of objects bigger than 210/285 nm.

- k_G, the rate at which the size of the objects in solution increases, after a delay of t_0.

2.4.1 Nucleation

The analysis of the overall scattered intensity (SLS measurements for the effect of $[Sub]_0$ and $[Mg^{2+}]_0$ (Figure 3.4C and F, respectively) as a function of time allows to characterise the appearance of colloidal particles in the solution. Indeed, the scattered intensity depends not only on the size of the scatterers, but also on their concentration in the dispersion. An increase

of the scattered intensity of a sample is then due to the increase either of the size of the objects that are dispersed or of their concentration. As the hydrodynamic diameter does not evolve much before t_0 (see Figure 3.4B and E), the intensity can then be correlated to the formation of CaP particles in the solution. The initial nuclei are too small to be directly measured by DLS, but the evolution of the scattered intensity shows that k_N is strongly correlated to the rate of the precipitation of CaP and hence the nucleation of the minerals, as the scattered intensity increases as the number of CaP particles of similar dimension increases in solution.

As described in *3.2* and *3.3* and shown in Figure 3.5A, k_N is modified only by the initial substrate concentration, $[Sub]_0$, that is linked to the enzyme activity (as shown in Figure 3.4A). On the contrary, the series with $[Sub]_0$ = 7.0 mM and various $[Mg^{2+}]_0$ displays remarkably the same scattered intensity as a function a time. These findings lead to the following interpretations. With this enzymatic model, tuning the enzymatic activity by adjusting $[Sub]_0$ (Figure 3.4A) and, thus, tuning the rate of phosphate ion release enables to modulate the nucleation rate of CaP particles (Figure 3.5A). Moreover, the inhibitory effect of magnesium ions plays a role only on the growth of CaP (Figure 3.5FB), not on its nucleation (Figure 3.5B). As already stated, magnesium ions do obviously not interfere with the enzymatic process, as suggested by the corresponding activity measurements (Figure 3.4D). During this nucleation stage, TEM micrographs showed the formation of ACP particles of limited size, which exhibited larger dimensions in presence of Mg^{2+} ions, in agreement with the DLS results. The values themselves differ between DLS and TEM, as both techniques do not measure the particle size through the same physical properties and with the same statistical weighting.

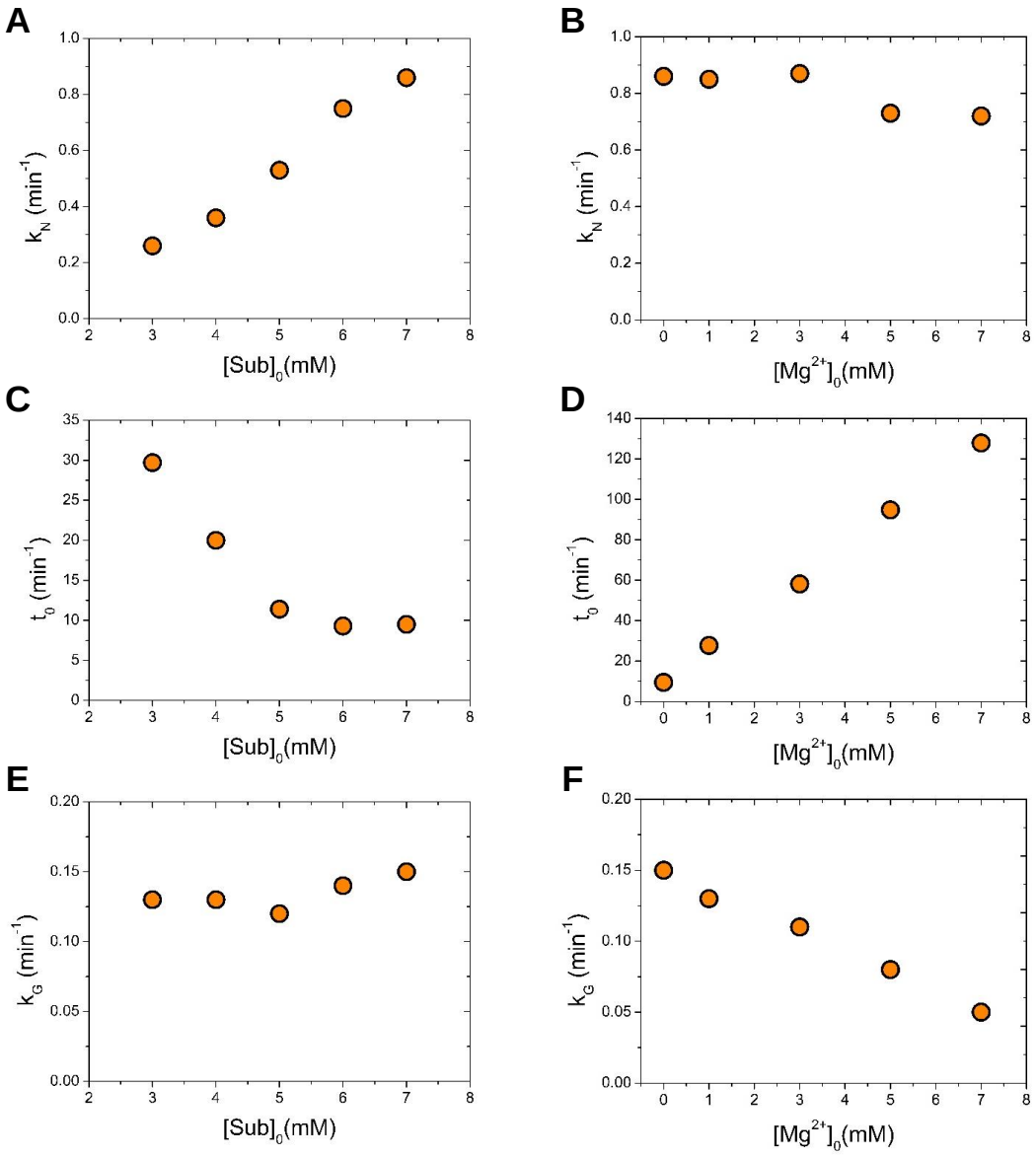

Figure 3.5. Plots of (A, B) the nucleation rate (k_N), (C, D) the retardation time (t_0) and (E, F) the growth rate (k_G) as a function of (A, C, E) the concentration of the substrate, $[Sub]_0$ or (B, D, F) the concentration of magnesium ion added in the medium, $[Mg^{2+}]_0$.

2.4.2 Retardation time

The analysis of the hydrodynamic diameter as a function of time (Figure 3.4B and E) allowed to characterise the retardation time t_0 after which the growth of the solid in the solution started. These characteristic times are given in Table 3.1 and their dependency on $[Sub]_0$ and $[Mg^{2+}]_0$ are plotted in Figure 3.5C and D. The retardation time can be attributed to the delay time that is commonly observed between the formation of a first amorphous calcium phosphate phase, often referred to as ACP, and the transformation of this solid into hydroxyapatite, HAP, or other crystallised phases, depending on the experimental conditions. Indeed, this transition has

already been reported since the work of Termine and Eanes [15] and then thoroughly studied in the literature for several decades [9, 12, 13, 16-20]. The amorphous-to-crystalline transition is associated with a pH plateau as observed in Figure 1 and broadly reported in numerous studies [3, 21, 22]. The pH value of this plateau depends on various parameters: the starting pH, the use of a buffer or not, etc. This delay is due to the difference between the surface energies of both solids: as ACP is more quickly formed but HAP is more thermodynamically stable, a transition from one phase to the other is expected to happen and, in this case, it has been shown experimentally that a characteristic retardation time elapses between the formation of the first ACP solids and the first HAP crystals. This value is often called *induction time* but this term is misleading as the induction time is the time during which a supersaturated solution maintains a metastable state [23]. Accordingly, it applies to the nucleation in solution of a solid phase and, in this case, the ACP, which is solid, is already formed before HAP appears: this is why it is called *retardation time* here.

In the case of the present work, t_0 depends on both $[Sub]_0$ and $[Mg^{2+}]_0$, but in different ways. Indeed, as shown in Figure 3.5C and D, t_0 appears to decrease progressively when increasing $[Sub]_0$ until reaching a minimum and becoming constant between 5.0 and 7.0 mM, whereas it increases proportionally with $[Mg^{2+}]_0$.

The trends shown in Figure 3.5C and D can be rationalised as follows. First, the effect of $[Sub]_0$ is necessarily linked to the enzyme activity and, thus, to the rate of phosphate ion release in solution. Then, since t_0 seems to reach a limit value when $[Sub]_0$ is increased from 5.0 to 6.0 mM, it suggests that the system reaches then a composition above which t_0 does not change anymore. Below $[Sub]_0$ = 5.0 mM, the phosphate concentration in solution must be the time limiting parameter towards the CaP phase transition. Above 5.0 mM, t_0 only depends on thermodynamic and kinetic parameters influencing the CaP mineralization, similarly to what is commonly observed for supersaturated solutions, i.e. not involving enzymes.

Second, the effect of $[Mg^{2+}]_0$ is in good agreement with descriptions that have already been proposed in the literature, for example in [17, 20, 24]. Indeed, the incorporation of magnesium ions in amorphous calcium phosphate during the mineralization, presumably through adsorption on the mineral surface [12], stabilises the amorphous phase and increases the retardation time [20]. When more magnesium ions are added, more ions can adsorb at the surface of more particles, delaying then more the transition towards the crystalline phases. Thus, when more Mg^{2+} ions are added, more ACP particles can be formed. This would then explain

why the scattered intensity increases up to a higher value before the transition that is characterised by the drastic drop indicated by the arrows in Figure 3.4F.

2.4.3 Growth

The analysis of the overall hydrodynamic diameter as a function of time (Figure 3.4B and E) allowed to characterise the rate constants, k_G, of the growth of the solid in the solution, after the retardation time t_0. These rate constants are given in Table 3.1 and their dependency on $[Sub]_0$ and $[Mg^{2+}]_0$ are plotted in Figure 3.5E and F.

The variations of k_G for both series are remarkably different. Indeed, k_G is not significantly affected by $[Sub]_0$. It shows then that neither the enzyme activity nor the overall phosphate concentration seems to modify the growth rate of ACP particles: in these experimental conditions, k_G could be due to the difference of kinetic rates between the disappearance of ACP and the formation of HAP, where ACP particles seem to turn directly into HAP platelets without a noticeable transition through an intermediate phase (see Figures 2A, B and Scheme 3.2). By contrast, k_G decreases steeply when $[Mg^{2+}]_0$ increases. As already discussed when considering the effect of $[Mg^{2+}]_0$ on t_0, this result is coherent with the inhibitory role of these ions in the crystallisation process. Indeed, when magnesium ions stabilise the ACP phase, they slow down the amorphous-to-crystalline transition [17] that yields HAP crystals, this effect being probably proportionate to the amount of magnesium ions adsorbed at the surface of the mineral upon its formation. This transition is shown to occur through the formation of intermediate phases (see Figures 2A', B' and Scheme 2), sometimes exhibiting a core-shell structure (Figure 3.2B'). We hypothesise that the formation of this structure is due to the presence of magnesium in the ACP particles formed during this process. Support of this hypothesis is given by the elementary analysis performed by STEM-EDX, that shows the homogeneous presence of magnesium in the ACP particles obtained in these conditions (Figure 3.3D). The presence of magnesium in the growth intermediate was also observed after 162 min, only when Mg^{2+} ions are added (Figure 3.3E). Ca/P and Mg/P ratios respectively equal to 1.08 and 0.13 were found in this case, in the area of interest (Figures S3.4A, B, Supporting Information). Importantly, the formation of these core-shell structures is accompanied by the formation of elongated platelets, clearly visible in the interparticle space (Figures 3.2B' and 3.3D). This supports the idea that HAP grows on the surface of the poorly crystalline core-shell CaP intermediates, following the pathway depicted in Scheme 3.2. Accordingly, the sudden increase of the hydrodynamic diameter observed by DLS is most probably due to the formation of the first

elongated platelets, which turn, subsequently, into platelet-shaped hydroxyapatite, while the core-shell structure dissolve.

In order to shine a new light on the comparison between the influences of $[Sub]_0$ without Mg^{2+} ions, in one hand, and $[Mg^{2+}]_0$ at $[Sub]_0$ = 7.0 mM, on the other hand, the evolution of the mean scattered intensity obtained by SLS was plotted as a function of the hydrodynamic diameter obtained by DLS, as presented in Figure 3.6. Indeed, these plots allow to get a complementary description of the processes at stake when studying the concomitant evolution of these physical quantities. On these plots, a first observation allows to distinguish for all the experiments ($[Sub]_0$ and $[Mg^{2+}]_0$ series alike) a first *nucleation phase*, characterised by an increase of the scattered intensity without an increase of the hydrodynamic diameter, followed by a *growth phase*, were mainly the increase of the hydrodynamic diameter can be observed.

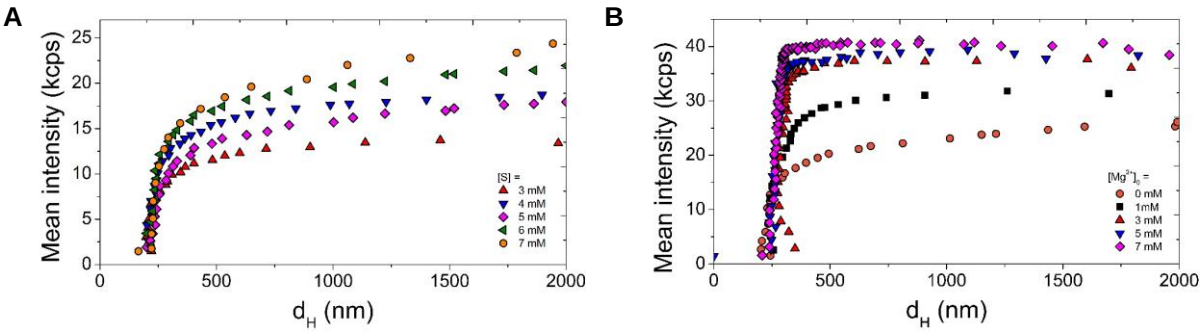

Figure 3.6. Plots of the mean intensity (data from SLS) versus hydrodynamic diameter (data from DLS). Measurements were performed (A) at different $[Sub]_0$ values, and (B) at $[Sub]_0$ = 7.0 mM, while varying $[Mg^{2+}]_0$, as indicated.

However, these two mineralization phases seem to be remarkably decoupled, in particular when the magnesium concentration was equal to 3.0 mM and above. Indeed, as shown in Figure 6B, the scattered intensity displays a nearly right-angle shape, the plots for the $[Mg^{2+}]_0$ concentrations 3.0, 5.0 and 7.0 mM being nearly superimposed. This highlights further the specific role of Mg^{2+} ions in the mineralization process and allows to illustrate their specific role in the prevention of the growth of the calcium phosphate particles during the first nucleation stage.

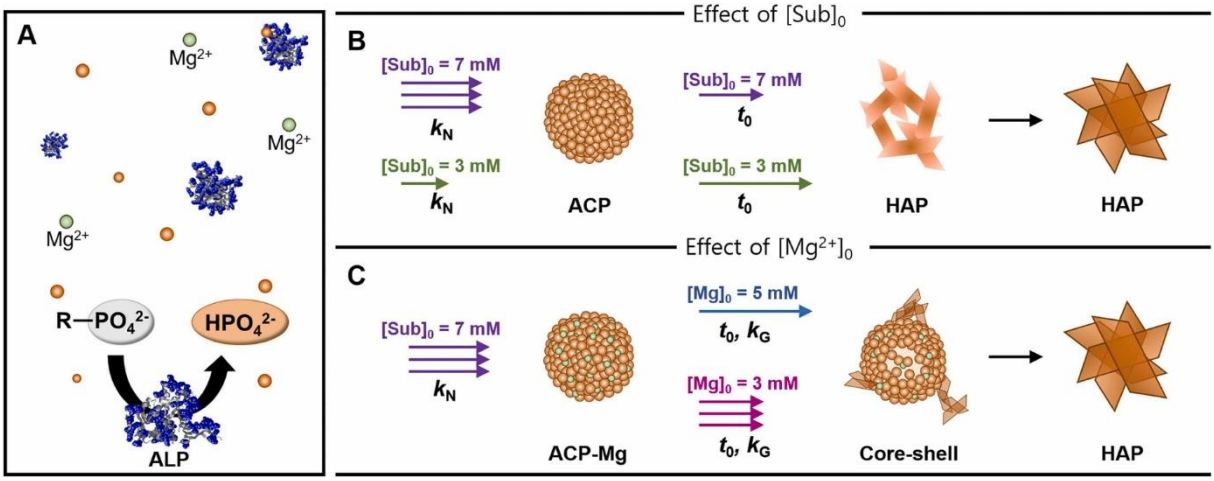

Scheme 3.2. A simplified view depicting the enzyme-assisted mineralization pathways. (A) Calcium phosphate (CaP) mineralization through homogeneous enzymatic catalysis: alkaline phosphatase (ALP) is present in the same phase as its substrate ($R\text{-}PO_4^{2-}$) and CaP ion precursors (i.e. calcium ions presented as uniform spheres for sake of clarity). (B, C) Mineralization pathways as a result of the variation of (B) the enzymatic activity, modulated by the concentration of its substrate ($[Sub]_0$), or (C) the addition of magnesium ions, a crystallisation inhibitor, at different concentrations ($[Mg^{2+}]_0$). The addition of more substrate increases the nucleation rate constant, k_N, as indicated by the increasing number of arrows on the scheme. The addition of more magnesium ions reduces the growth rate constant, k_G (number of arrows), and increases the retardation time observed during the mineralization (indicated by longer arrows).

3 Conclusion

The study detailed in this work investigates the utility of a model approach of the enzyme-assisted biomineralization of CaP, that involves the enzymatic release of the phosphate ions that trigger the mineralization. Indeed, as thoroughly developed in our recent review[16], this way of controlling the mineralization processes seems to be relevant to address the apparent contradiction between MV and intrafibrillar calcium phosphate mineralization, as it allows to control when and where this process occurs. Moreover, in the present work, we showed that the study of the enzyme-assisted mineralization allowed to identify fine parameters that play an important role in mineralization processes. Indeed, it enabled to introduce new ways to decouple the study of biomimetic nucleation and growth of CaP thanks to the progressive *in situ* release of phosphate mediated by the enzymes.

These processes were monitored in this study by light scattering measurements performed in real-time during the early stages of the mineralization. The relevance of the use of light scattering measurements was validated by preliminary experiments, where the mineralization was followed by pH measurements and, in the same conditions, by DLS and SLS. The use of light scattering techniques to monitor in real-time the process of mineralization of calcium

phosphate was surprisingly very scarce to our knowledge and this study shows that it is beneficial to characterise efficiently this kind of systems, particularly when combining DLS and SLS measurements.

4 References

1. Johnsson, M.S.A. and G.H. Nancollas, *The Role of Brushite and Octacalcium Phosphate in Apatite Formation.* Critical Reviews in Oral Biology & Medicine, 1992. **3**(1): p. 61-82.
2. Pan, H., et al., *Mystery of the transformation from amorphous calcium phosphate to hydroxyapatite.* Chemical Communications, 2010. **46**(39): p. 7415-7417.
3. Jiang, S., et al., *Amorphous calcium phosphate phase-mediated crystal nucleation kinetics and pathway.* Faraday Discussions, 2015. **179**(0): p. 451-461.
4. Carino, A., et al., *Formation and transformation of calcium phosphate phases under biologically relevant conditions: Experiments and modelling.* Acta Biomaterialia, 2018. **74**: p. 478-488.
5. Habraken, W.J.E.M., et al., *Ion-association complexes unite classical and non-classical theories for the biomimetic nucleation of calcium phosphate.* Nature Communications, 2013. **4**(1): p. 1507.
6. Colaço, E., et al., *Calcium phosphate mineralization through homogenous enzymatic catalysis: Investigation of the early stages.* Journal of Colloid and Interface Science, 2020. **565**: p. 43-54.
7. Wang, L. and G.H. Nancollas, *Calcium Orthophosphates: Crystallization and Dissolution.* Chemical Reviews, 2008. **108**(11): p. 4628-4669.
8. Salimi, M.H., J.C. Heughebaert, and G.H. Nancollas, *Crystal growth of calcium phosphates in the presence of magnesium ions.* Langmuir, 1985. **1**(1): p. 119-122.
9. Yun, J., et al., *A Kinetic Model for Hydroxyapatite Precipitation in Mineralizing Solutions.* Crystal Growth & Design, 2018. **18**(5): p. 2717-2725.
10. Onuma, K., et al., *Precipitation Kinetics of Hydroxyapatite Revealed by the Continuous-Angle Laser Light-Scattering Technique.* The Journal of Physical Chemistry B, 2000. **104**(45): p. 10563-10568.
11. Lotsari, A., et al., *Transformation of amorphous calcium phosphate to bone-like apatite.* Nature Communications, 2018. **9**(1): p. 4170.
12. Jin, B., et al., *Phase Transformation Mechanism of Amorphous Calcium Phosphate to Hydroxyapatite Investigated by Liquid-Cell Transmission Electron Microscopy.* Crystal Growth & Design, 2021. **21**(9): p. 5126-5134.

13. Cathala, G. and C. Brunel, *Bovine kidney alkaline phosphatase. Catalytic properties, subunit interactions in the catalytic process, and mechanism of Mg2+ stimulation.* Journal of Biological Chemistry, 1975. **250**(15): p. 6046-6053.
14. Linden, G., D. Chappelet-Tordo, and M. Lazdunski, *Milk alkaline phosphatase. Stimulation by Mg2+ and properties of the Mg2+ site.* Biochimica et Biophysica Acta (BBA) - Enzymology, 1977. **483**(1): p. 100-106.
15. Termine, J.D. and E.D. Eanes, *Comparative chemistry of amorphous and apatitic calcium phosphate preparations.* Calcified Tissue Research, 1972. **10**(1): p. 171-197.
16. Eanes, E.D., I.H. Gillessen, and A.S. Posner, *Intermediate States in the Precipitation of Hydroxyapatite.* Nature, 1965. **208**(5008): p. 365-367.
17. Boskey, A.L. and A.S. Posner, *Magnesium stabilization of amorphous calcium phosphate: A kinetic study.* Materials Research Bulletin, 1974. **9**(7): p. 907-916.
18. Christoffersen, J., et al., *A contribution to the understanding of the formation of calcium phosphates.* Journal of Crystal Growth, 1989. **94**(3): p. 767-777.
19. Yang, X., et al., *Influence of magnesium ions and amino acids on the nucleation and growth of hydroxyapatite.* CrystEngComm, 2011. **13**(4): p. 1153-1158.
20. Jin, W., et al., *Synergic Effect of Sr2+ and Mg2+ on the Stabilization of Amorphous Calcium Phosphate.* Crystal Growth & Design, 2018. **18**(10): p. 6054-6060.
21. Jiang, S., et al., *Faster nucleation at lower pH: amorphous phase mediated nucleation kinetics.* Physical Chemistry Chemical Physics, 2013. **15**(30): p. 12530-12533.
22. Jiang, S., et al., *Effect of the aggregation state of amorphous calcium phosphate on hydroxyapatite nucleation kinetics.* RSC Advances, 2017. **7**(41): p. 25497-25503.
23. Kashchiev, D., *Nucleation*. 2000: Elsevier.
24. Gelli, R., et al., *Exploring the effect of Mg2+ substitution on amorphous calcium phosphate nanoparticles.* Journal of Colloid and Interface Science, 2022. **606**: p. 444-453.

5 Supplementary Information

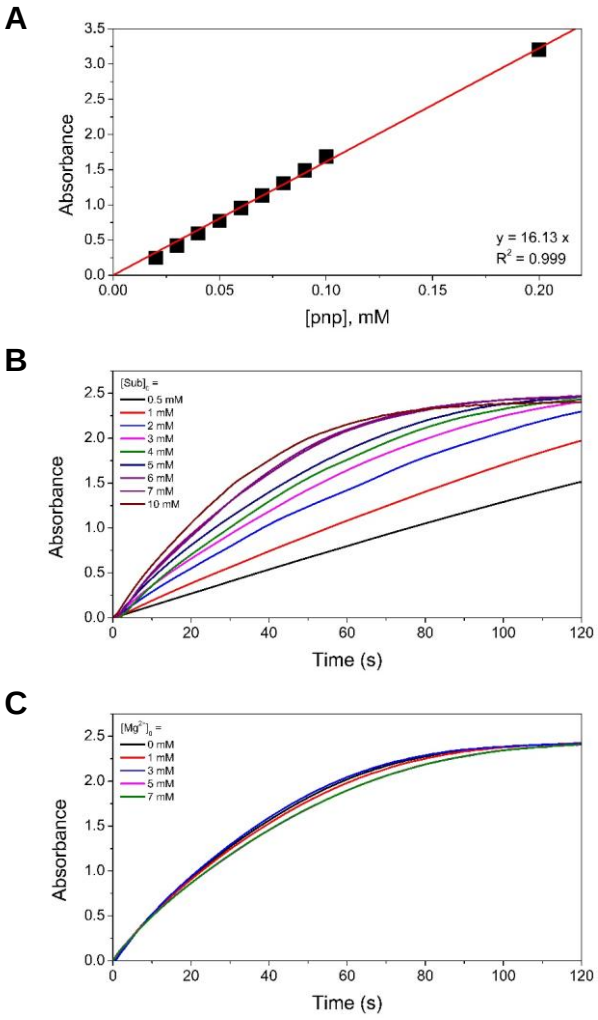

Figure S3.1. Measurements of ALP catalytic activity in aqueous solution ($CaCl_2$ at 11.4 mM; pH = 8.2; 37 °C). (A) Calibration curve relating the absorbance (λ = 410 nm) to pnp concentration. (B, C) Evolution of the absorbance (λ = 410 nm) vs time due to the enzymatic production of pnp (B) at different concentrations of the substrate ($[Sub]_0$), and (C) at $[Sub]_0$ = 7.0 mM, while varying $[Mg^{2+}]_0$, as indicated.

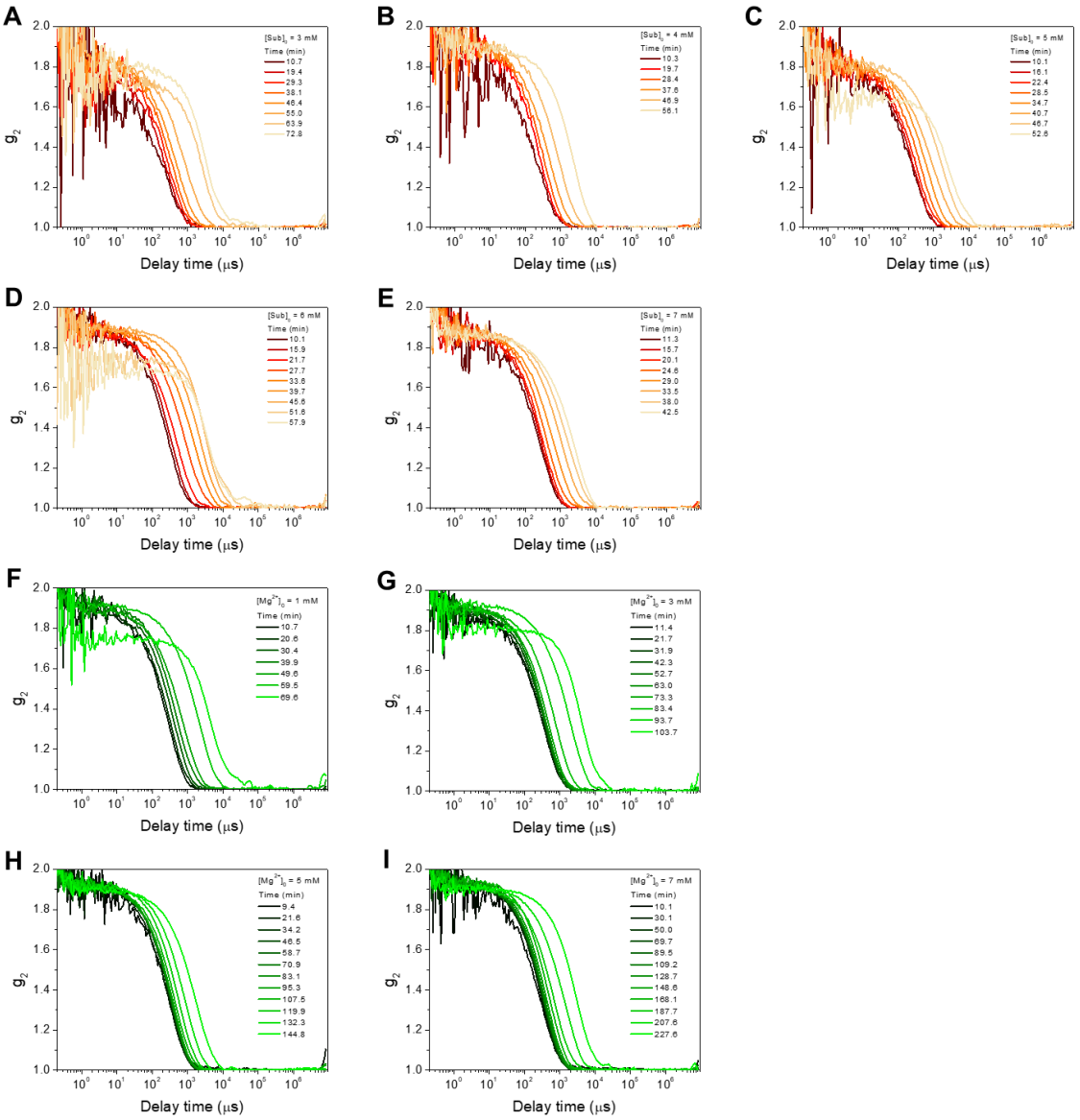

Figure S3.2. Representative evolutions of DLS correlograms during the enzyme-assisted mineralization at 37 °C, at different $[Sub]_0$ and $[Mg^{2+}]_0$.
(A-E) At $[Mg^{2+}]_0$ = 0 and $[Sub]_0$ = (A) 3.0 mM, (B) 4.0 mM, (C) 5.0 mM, (D) 6.0 mM and (E) 7.0 mM.
(F-I) At $[Sub]_0$ = 7.0 mM and $[Mg^{2+}]_0$ = (F) 1.0 mM, (G) 3.0 mM, (H) 5.0 mM and (I) 7.0 mM.

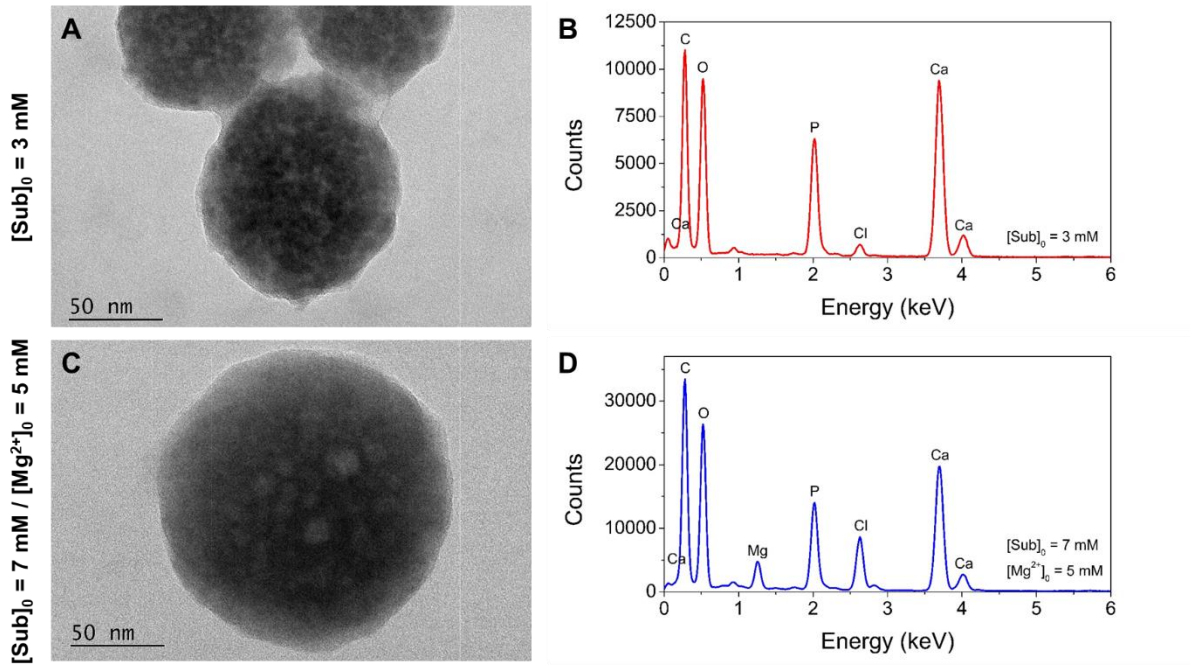

Figure S3.3. (A, C) TEM micrographs and (B, D) the associated EDX spectra of CaP particles obtained (A, B) at $[Sub]_0$ = 3.0 mM, without $MgCl_2$ after 30 min of mineralization, and (C, D) at $[Sub]_0$ = 7.0 mM and $[Mg^{2+}]_0$ = 5.0 mM after 91 min of mineralization. EDX spectra shown in panels B and D yield a Ca/P ratio equal respectively to 1.30 and 1.27. The Mg/P ratio for the spectrum D is equal to 0.35.

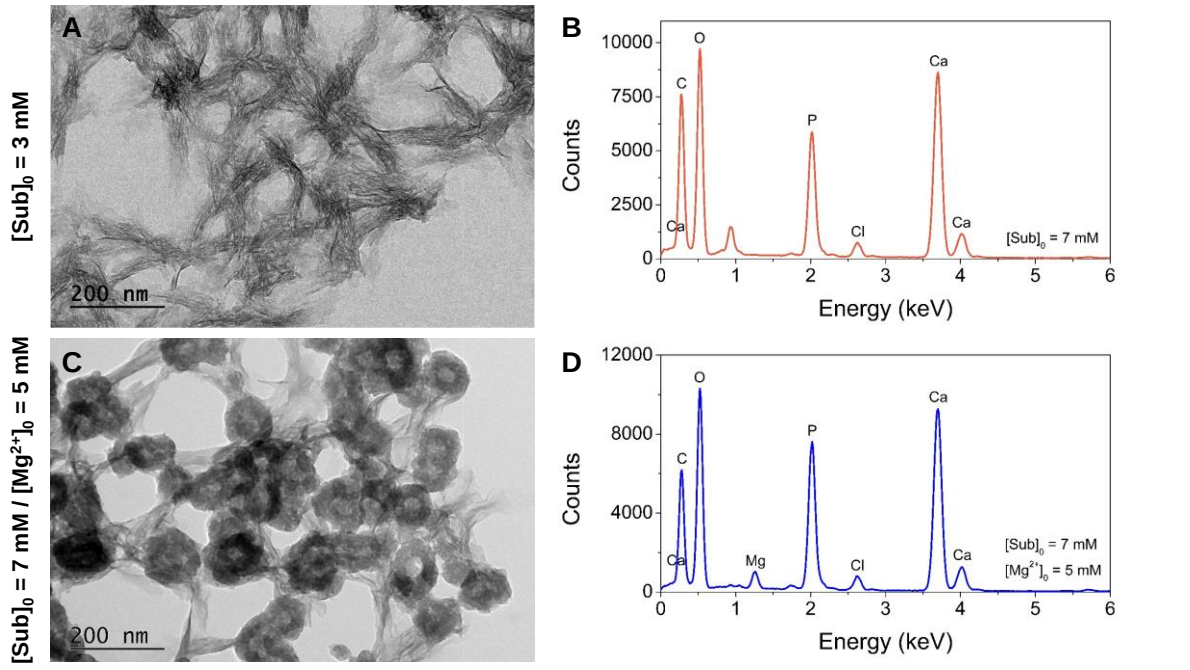

Figure S3.4. (A, C) TEM micrographs and (B, D) the associated EDX spectra of CaP particles obtained (A, B) at $[Sub]_0$ = 3.0 mM, without $MgCl_2$ after 37 min of mineralization, and (C, D) at $[Sub]_0$ = 7.0 mM and $[Mg^{2+}]_0$ = 5.0 mM after 142 min of mineralization. EDX spectra shown in panels A and B yield a Ca/P ratio equal to 1.30 and 1.08, respectively. The Mg/P ratio for the spectrum D is equal to 0.13.

Chapter 4.
Enzyme-assisted mineralization over multilayers: role of collagen

The two features of biomineralization are homeostasis and compartmentalization. Homeostasis is achieved by enzyme-assisted mineralization as shown in the last chapter. In this chapter, the system is developed to indicate compartmenalization. It is to organize the segregation of specific biomolecules, enzymes and ions within distinct microenvironments often localized in matrix vesicles or organic matrices. This spatial organization enhances control over mineral deposition, ensuring the precise and controlled formation of mineralized structures. To realize the system, enzyme-assisted mineralization is carried out in a heterogeneous phase in which ALP is immobilized on the surface with or without collagens while calcium ions and substrate of enzymes are present in a solution. The CaP mineralization in the heterogeneous phase is studied using AFM, XPS and SEM over 7 days.

Some parts of this work is the subject of an article published on 11 July 2023 - Surfaces and Interfaces volume 40, 103059, https://doi.org/10.1016/j.surfin.2023.103059

1 Introduction

In the previous chapter, ALP successfully initiated CaP mineralization in solution followed by regulation of mineralization through modulation of its activities. It motivates further development of biomimetic systems of CaP mineralization not only to incorporate an additional incorporation of proteins existing in the mineralizing matrix but also bring another biological feature, compartmentalization. In this chapter, type I collagens, which are one of the major constituents in the matrix, are comprised as an additional protein. In the developed system with two different proteins, it is critical to preserve their own structure and biological activities which is a challenge. The realization of compartmentalization can be achieved by transferring the system on the surface. The solid surface based soft-matter structure as well as heterogeneous phases in aqueous solutions can play as pseudo-compartments by fostering the formation of molecular concentration gradients needed to initiate catalysis. For this purpose, we used the sequential layer-by-layer (LbL) assembly on solid surfaces to co-immobilize type-I collagen and ALP within polyelectrolyte multilayers, aiming to mimic the *in vivo* spatiotemporal control of CaP mineralization at the solid/liquid interface. LbL is a powerful method for the elaboration of nanostructured films, which may control the adsorption behavior of proteins and, thus, the subsequent interaction with cells, aiming to coherently interface materials and biological systems [1, 2]. In addition to the high versatility of the technique, two important advantages of LbL in the context of biomaterials lie into the ability of polyelectrolyte multilayers to adhere on a wide range of substrates with diverse natures and shapes, and the possibility to incorporate various biomacromolecules [3-6].

While the enzyme allows an *in situ*-controlled generation of CaP ion precursor, the incorporation of type I collagen within the film offers a suitable chemical environment for mineralization. This hypothesis is suggested on the basis of in vivo observations, since type I collagen fibrils are found to be highly mineralized in bone tissues, both in the extra- and the intra-fibrillar spaces [7]. In vitro studies of collagen mineralization are mostly performed in colloidal media, where collagen and CaP ion precursors, sometimes in the presence of other molecules, are mixed together [8]. Yet, mineralizing collagen fibrils immobilized on solid supports is more relevant when mimicking the extracellular matrix environment, and offers more levers to control of the self-assembly of collagen molecules and their supramolecular organization [9].

The biomimetic strategy based on the initiation of CaP mineralization by enzymes in the vicinity of collagen fibrils showed, interestingly, the possibility to form mineral on planar

surfaces and even within nanopores with mean diameters ranging from about 200 to 500 nm [10]. However, the mechanism by which CaP mineral forms on the solid surface (heterogeneous nucleation and growth) remains unclear, particularly when directed by enzyme-catalyzed reactions. Moreover, if, in this strategy, both enzymes and collagen are embedded within the nanostructured film, the influence of their proximity in the mineralization process.

Herein, we investigate the mechanism of the formation of a CaP mineral layer over LbL assemblies containing type I collagen and ALP enzymes. For this purpose, multilayers embedding either ALP enzymes or both type I collagen and enzymes are built up. A particular attention is dedicated to the catalytic activity of enzymes when embedded in multilayers in the presence or absence of collagen fibrils. Moreover, the subsequent mineralization processes is probed in-depth by means of atomic force microscopy (AFM), particularly at early stages (few hours), and X-ray photoelectron spectroscopy (XPS). Complementary scanning electron microscopy (SEM) characterizations are also performed at late stages of mineralization (several days).

2 Results and discussion

2.1 LbL assembly and catalytic activity of enzymes

The build-ups of $(PAH/ALP)_5$ and $(Col/HA)_3(PAH/ALP)_5$ multilayers were performed following the procedure depicted in Scheme 2.1 in Chapter 2. The successful assembly of the different (bio)macromolecules, using this LbL method, was demonstrated in a recent paper using *in situ* QCMD monitoring [10]. In the present study, the morphology of the different multilayered films was probed by AFM on a flat silicon wafer (Figure 4.1A, $R_{rms} = 0.37 \pm 0.01$ nm) in the dried state, i.e. after their build-up, rinsing and subsequent drying. After the build-up of $(PAH/ALP)_5$ multilayers, AFM images showed the presence of particles uniformly distributed on the surface, resulting in a significant increase of the roughness (Figure 4.1B, R_{rms} = 4.28 nm). Scan line revealed that isolated particles exhibit fairly uniform heights of 17.1 ± 4.4 nm (data from size distribution, n = 50). This value is close to the hydrodynamic diameter (17.9 ± 7.8 nm) measured by dynamic light scattering (DLS) on ALP solution in the same conditions (pH = 7.4, 37 °C) [11], and is consistent with the dimeric form of the enzyme. They may also correspond to aggregates of enzymes or polyelectrolyte-protein complexes.

When collagen was incorporated within the multilayers, the build-up was performed following two main steps, as described in section *3.1* in Chapter 2. AFM images showed that crosslinked $(Col/HA)_3$ multilayers organize into a regular net-like structure (Figure 4.1C), showing well-

defined fibrils with heights around 11.3 ± 4.4 nm (data from size distribution, n = 50). The buildup of collagen-based multilayers is particularly tricky, owing to the anisotropic feature of the protein 3D-structure and the resulting charge distribution along the biomacromolecule. As the LbL assembly was performed at pH 4.5, collagen solution is expected to be mainly composed of monomers (triple-helix), which exhibit an overall positive charge, and may include a small fraction of aggregates. Upon adsorption on the hydrophilic HA layer, collagen monomers adopt a lying position, as suggested by QCMD data [10], and their self-assembly is driven by the interplay of molecule-surface and molecule-molecule interactions [12]. Further collagen adsorption favors the formation of fibrils the diameter of which increases with increasing the number of bilayers [13]. In the present study, the typical D-period was not observed on individual fibrils, probably due to their small diameter, which corresponds to the adjacent association of only a few monomers (Figure 4.1C).

After the build-up of $(Col/HA)_3(PAH/ALP)_5$ multilayers, these fibrils are no longer observed, suggesting they are covered by the $(PAH/ALP)_5$ multilayers (Figure 4.1D). However, the obtained morphology does not allow to make a clear distinction between collagen fibrils and individual enzymes.

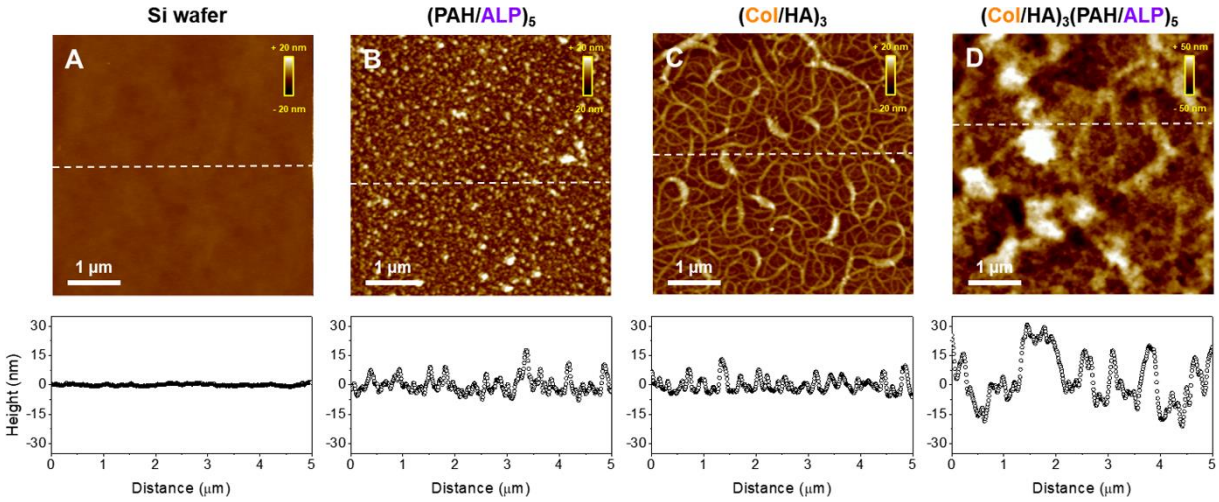

Figure 4.1 AFM height images recorded on silicon wafers (A) prior to and after the buildup of (B) $(PAH/ALP)_5$; (C) crosslinked $(Col/HA)_3$ or (D) $(Col/HA)_3(PAH/ALP)_5$ multilayers. Line scans were taken at the locations indicated by dashed lines.

The catalytic properties of ALP embedded within the multilayers were investigated using pnpp as a substrate, following the procedure described in section *3.3* in Chapter 2. Typical evolutions of the absorbance measured at 410 nm over time are shown in Figure 4.2A (see inset), reflecting the progressive production of pnp through the catalytic activity of ALP. The effective activities

measured for the systems obtained on $(PAH/ALP)_5$ and on $(Col/HA)_3(PAH/ALP)_5$ multilayers yield values of 0.98 ± 0.21 and 4.88 ± 0.39 μM $min^{-1} \cdot cm^{-2}$, respectively (Figure 4.2A) corresponding to an activity about 5 times higher when collagen was incorporated within the multilayers.

This difference may be explained by three main reasons: (i) a deactivation of the enzyme in the adsorbed state due to an unfavorable orientation or a distortion of its 3D-structure, (ii) a stimulating effect due to the biomacromolecules embedded with enzymes in the multilayers, or (iii) a variable amount of immobilized enzymes. These hypotheses are further examined below.

(i) In both $(PAH/ALP)_5$ and $(Col/HA)_3(PAH/ALP)_5$ systems, enzymes are embedded in multilayers via PAH as a polycation, which allows their immobilization mainly through electrostatic interaction and in random orientations. Indeed, ALP exhibits a non-localized distribution of negatively charged residues at its macromolecular surface [11], which allows its adsorption onto positively charged groups of PAH without a preferential orientation. Accordingly, an unfavorable orientation, which may considerably impact the enzyme-substrate interaction, is unlikely. Moreover, as shown by AFM, the dimensions of the adsorbed enzymes are close to that measured by DLS in the same conditions. Thus, a possible effect on its 3D-structure (e.g. distortion or disassembling of the multimeric forms) can also be reasonably ruled out.

(ii) A possible effect of the biomacromolecules present in the multilayers was investigated by evaluating the specific activity of free ALP enzymes in the presence of either Col or HA in the aqueous solution. For this purpose, the progressive production of pnp by ALP was monitored at different ALP concentrations (0, 5, 10, 50, and 100 $\mu g \cdot mL^{-1}$) without any additional components or with the addition of Col (0.1 $mg \cdot mL^{-1}$) or HA (1 $mg \cdot mL^{-1}$). Specific activities in each condition were obtained by plotting the enzyme activity vs. the concentration of enzymes (Figure S4.1, Supporting Information). Results showed that the specific activity of ALP (655 ± 3.51 $U \cdot g^{-1}$) increases only slightly when adding collagen (769 ± 9.26 $U \cdot g^{-1}$) or HA (727 ± 4.04 $U \cdot g^{-1}$) in the solution. This enhancement of the ALP activity is relatively weak (about 17 % and 11 % of increase with Col and HA, respectively) and could not explain the enhancement of the activity observed in Figure 4.2A.

(iii) An increase of the adsorbed amount of enzymes within $(Col/HA)_3(PAH/ALP)_5$ compared to $(PAH/ALP)_5$ multilayers could, thus, be considered by examining two

factors. First, the incorporation of collagen molecules in the multilayers and their supramolecular organization into fibrils, as shown by AFM (Figure 4.1C), increases appreciably the surface roughness (R_{rms} increases from 0.37 ± 0.01 nm to 4.27 ± 0.46 nm, Figure 4.1A and C). However, this leads to a ratio between the developed and projected areas of the surface equal to 1.01, indicating that the specific surface, that is the surface available to host adsorbed enzymes, did not increase significantly in the presence of collagen fibrils. Second, ALP exhibits a high affinity toward type I collagen [14], which may favor the interaction of these entities, resulting in a more extensive adsorption of enzymes in the presence of collagen fibrils and then the significant increase of the enzymatic activity observed in $(Col/HA)_3(PAH/ALP)_5$ relatively to $(PAH/ALP)_5$ multilayers.

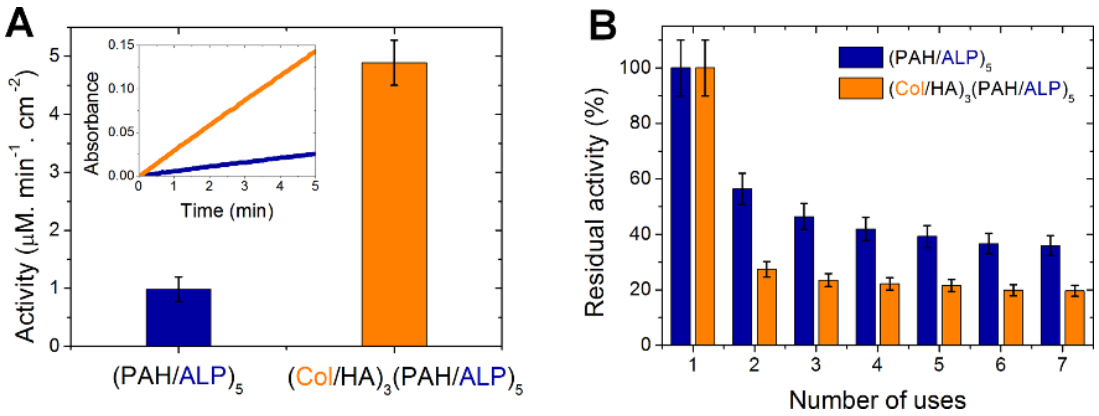

Figure 4.2 Catalytic activity of enzymes in multilayers (A) Initial enzymatic activity of ALP embedded within $(PAH/ALP)_5$ or $(Col/HA)_3(PAH/ALP)_5$ multilayers, as indicated (inset: typical evolution of the absorbance at 410 nm due to the production of pnp vs time). (B) Residual activity of ALP embedded within the different multilayers, as indicated, calculated as the percentage of initial activity after repeated use and rinsing cycles.

A further evaluation of the catalytic properties of enzymes embedded in the multilayers is given in Figure 4.2B. It shows the operational stability of immobilized enzymes, i.e. their ability to preserve their activity after repeated use cycles. For this purpose, seven successive use cycles were performed on the two studied multilayer systems, $(PAH/ALP)_5$ and $(Col/HA)_3(PAH/ALP)_5$. During each use cycle, the enzymatic activity is monitored in real-time over a period of 30 min, then stopped by collecting the supernatant and performing several rinsing with ultrapure water. For both systems, a significant decrease of the catalytic activity was observed after the second use: residual activities were equal to 56 % and 27 % of the initial value for $(PAH/ALP)_5$ and $(Col/HA)_3(PAH/ALP)_5$, respectively (Figure 4.2B). A slight

decrease of the activity can then be observed along the following successive uses. The first decrease of residual activity was more pronounced on $(Col/HA)_3(PAH/ALP)_5$ multilayers, but remains almost unchanged after the successive uses (residual activity equal to 27, 23 and 20 % of the initial value after two, three and seven uses, respectively) compared to $(PAH/ALP)_5$ multilayers (residual activity equal to 56, 46 and 35 % of the initial value after two, three and seven uses, respectively).

The significant activity loss observed after the first use cycle for both systems may be due to the desorption of enzymes in the solution where operational activities are performed. This hypothesis was investigated by measuring the enzymatic activity in the supernatant, i.e. in the pnpp solution in which the enzymes embedded in the multilayers had been incubated for 30 min. Results showed that the activity in the supernatant was significant after the first use (Figure S4.2, Supporting Information). By contrast, after additional successive uses, the enzymatic activities were below the detection limit. These results suggest that the significant activity loss observed, for both multilayer systems, is mainly due to the desorption of enzymes, while, upon further multiple uses, the mechanism of activity loss seems not to be due to the same mechanism, but probably to a typical enzyme deactivation mechanism.

To sum up, catalytic activity measurements revealed that the presence of $(Col/HA)_3$ multilayers enhances the enzymatic activity owing to a noticeable increase of the amount of adsorbed enzymes. Although a significant drop of activity was observed after the first use due to a significant desorption of enzymes, the outstanding ability of the embedded enzymes to maintain their catalytic activity was shown after several use cycles.

2.2 Surface evolution

Evolution of the surface topography

The formation of CaP minerals on $(PAH/ALP)_5$ and $(Col/HA)_3(PAH/ALP)_5$ multilayers was investigated by AFM after a given mineralization time ranging from 1 to 96 h. As detailed in section *3.2* in Chapter 2, the mineralization was initiated by immersing the surfaces in an aqueous solution (pH 7.4, 37 °C) containing Ca^{2+} ions and α-glycerol phosphate, the enzyme substrate. After a given time, samples were placed in three successive rinsing baths, dried under nitrogen gas flow and immediately characterized by AFM in ambient conditions. The immersion of the $(PAH/ALP)_5$ multilayers (Figure 4.3A) in the mineralization solution for 1 h showed a decrease of the surface density of the globular colloidal particles initially present (Figure 4.3B), which became significantly more pronounced after 6 and 16 h (Figure 4.3C and D), resulting in a significant decrease of the surface roughness (R_{rms} = 2.72, 0.85 and 0.92 nm

after 1, 6 and 16 h, respectively). After 24 h of mineralization, the AFM image showed the appearance of some new colloidal particles (Figure 4.3E), displaying an average height of 11.1 ± 5.5 nm (data from height distribution, n = 50). The topography of the $(PAH/ALP)_5$ multilayers after 48 h of mineralization became then radically different, showing particles present on the whole surface and at a high surface density (Figure 4.3F). The growth of these new particles, presumably CaP minerals, became more obvious after 96 h (Figure 4.3G), as bigger particles were observed, densely packed at the surface, reaching a full surface coverage, as it is shown by the scan lines in Figure 4.3H.

The evolution of $(Col/HA)_3(PAH/ALP)_5$ multilayers was different. The immersion of the sample (Figure 4.3I) in the mineralization solution for 1 h showed the typical fibrillar assemblies of collagen (Figure 4.3J). Interestingly, globular colloidal particles appeared seemingly preferentially located onto the fibrils (Figure 4.3J). After 6 h of mineralization, the AFM images showed colloidal particles accumulated along the collagen fibrils (Figure 4.3K). The morphology of these particles appeared slightly different from the globular ones observed after 1 h with more particles close to each other, being presumably grown CaP minerals.

The appearance of these particles along collagen fibrils, after 6 h of mineralization, is followed by a more obvious growth into bigger particles, which came then to more visible close contact with each other (Figure 4.3L). This results in a complete coverage of collagen fibrils with the presumable mineral particles, but the typical morphology of the fibrils remains visible (see arrows in Figure 4.3L). In this case, the actual particle height could not be evaluated properly because the AFM tip was too large to penetrate into the interstices between particles. After 24 h of incubation, the AFM image showed a surface fully coated with a presumable mineral layer, fibrils being no longer discernable (Figure 4.3M).

Interestingly, the extensive mineralization observed from 6 to 24 h seems to continue when increasing the incubation time to 48 h and 96 h, as bigger particles can be clearly observed (Figure 4.3N and O). This trend is supported by the evolution of the surface roughness (R_{rms}) calculated from three 2 × 2 μm^2 AFM images for each sample (Figure 4.3P). It showed that R_{rms} increased from 1 h to 96 h as a result of the growth of the mineral layer on $(Col/HA)_3(PAH/ALP)_5$ multilayers to reach a value around 50 nm, while R_{rms} values remained significantly lower for the $(PAH/ALP)_5$ multilayers around 2.6 nm (except the singular data point measured after 48 h).

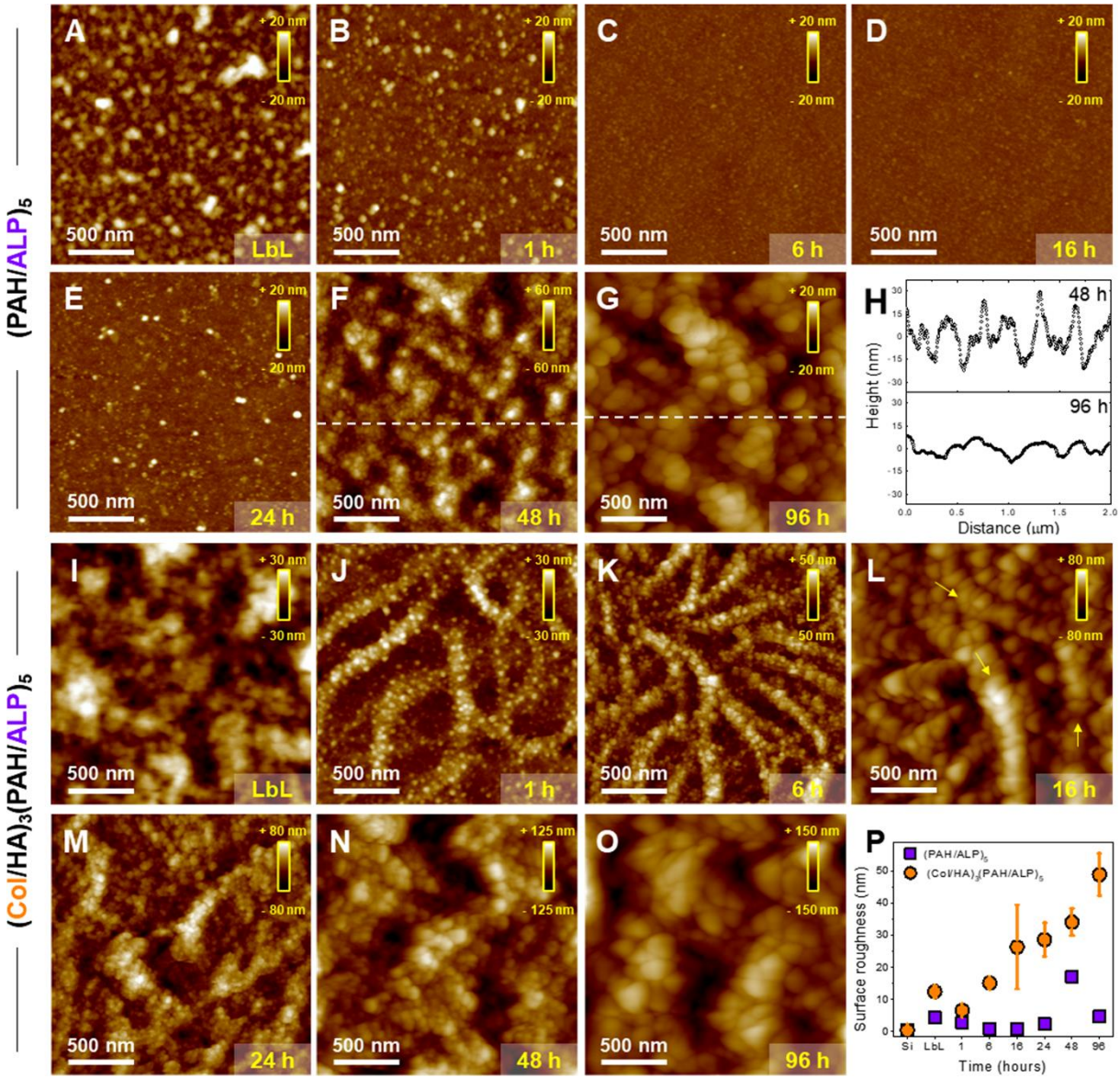

Figure 4.3 CaP mineralization on multilayers over time. (A-G, I-O) Representative AFM height images recorded on (A-G) $(PAH/ALP)_5$ and (I-O) $(Col/HA)_3(PAH/ALP)_5$ multilayers (A, I) prior to (labelled "LbL") and after immersion in the mineralization solution (pH 7.4, 37 °C) during (B, J) 1 h, (C, K) 6 h, (D, L) 16 h, (E, M) 24 h, (F, N) 48 h and (G, O) 96 h (see labels at the bottom left corner of images indicating the immersion time). Arrows indicate the location of collagen fibrils in image L. (H) Line scans taken at the locations indicated by dashed lines in the height images F (48 h) and G (96 h), as indicated. (P) Evolution of surface roughness (R_{rms} values computed from three different 2 µm × 2 µm images for each condition) for silicon wafer (labelled "Si"), non-mineralized layers (labelled "LbL") and mineralized layers formed on $(PAH/ALP)_5$ (squares) and $(Col/HA)_3(PAH/ALP)_5$ (circles) multilayers at different mineralization times.

Evolution of the surface composition

The evolution of the surface composition of the multilayers at early stages was investigated by XPS. Figure 4.4A shows typical C 1s peak recorded on multilayers prior to immersion in the

mineralization solution. It can be confidently decomposed into three components at the same FWHM: a component at 284.8 eV, due to carbon bound to carbon and/or hydrogen, **C**–(C,H), a component at ~286.3 eV due to carbon singly bound to oxygen or nitrogen, **C**–(O,N) and a component at ~288.0 eV, which may be mainly attributed to carbon involved in amide groups, N–**C**=O. No additional component at higher binding energies was considered in this case owing to the absence of a clear broadening (around 289.0 eV), and the relatively low FWHM of the three other components (1.2 to 1.4 eV), which does not justify the addition of a fourth component. In any case, the presence or absence of a contribution due to carboxyl/ ester groups (around 289.0 eV) should be taken with caution owing to its very low intensity, compared to the other components, that may influence the reliability of peak decomposition in this region. The immersion of the $(PAH/ALP)_5$ and $(Col/HA)_3(PAH/ALP)_5$ multilayers in the mineralization solution led to two main evolutions (Figure 4.4B). First, the contributions attributed to **C**–(O, N) and N–**C**=O groups in the C 1s decreased markedly with increasing the mineralization time. This is concomitant with the evolution of the N 1s peaks, which exhibit a main contribution at ~399.8 eV due to amine and amide groups, **N**–C, and a broadening at higher binding energy, ~401.5 eV, due to protonated amines, C–**N**H_3^+; the contribution attributed to amine/amide groups, mainly peptide bonds in proteins, decreased compared to the one attributed to protonated amine groups, mainly present in PAH. This suggests a change in the chemical nature of the adsorbed (bio)organic compounds. Second, the intensities of C 1s and N 1s peaks decreased progressively with the mineralization time. It could be due to a loss of adsorbed species or to a screening effect that may be caused by the formation of the mineral layer. In order to tell these two phenomena apart, the relevance of the surface molar concentrations of oxidized carbon ($C_{ox} = C_{286.3} + C_{288.0}$) as a protein marker is first examined. Figure 4.4C presents the plots of C_{ox} vs the concentration of nitrogen mainly due to peptidic links ($N_{399.8}$), showing that both $(PAH/ALP)_5$ (squares) and $(Col/HA)_3(PAH/ALP)_5$ (circles) samples follow a clear linear trend. The regression line, computed in the C_{ox} vs $N_{399.8}$ plot by considering all the samples, yields a slope of 2.25, which is close to the value expected for ALP (2.01) and type I collagen (2.08). This trend supports the consistency of the data extracted from peak decomposition and indicate that C_{ox} can be used as a relevant marker for proteins.

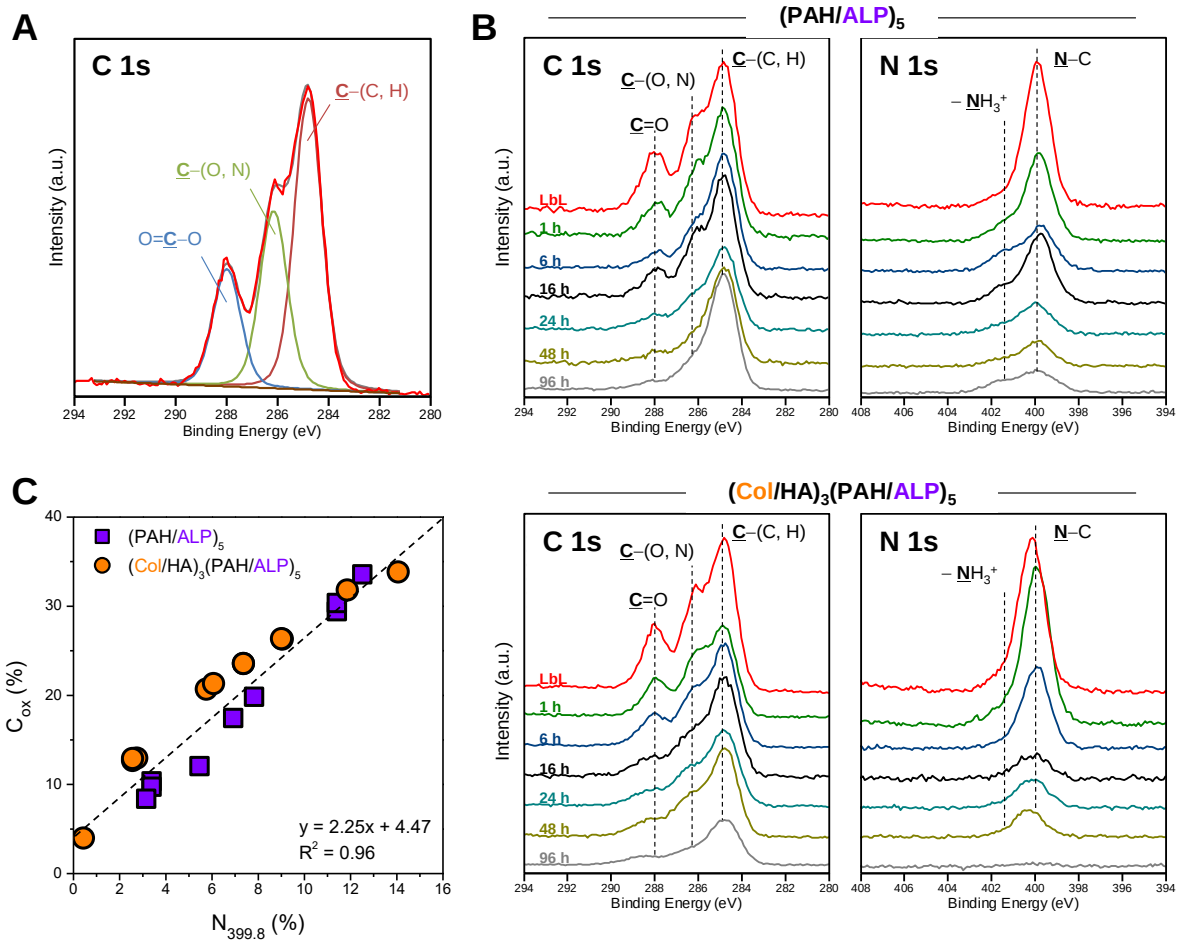

Figure 4.4 XPS measurements (A) Decomposition of C 1s peak recorded after the build-up of $(Col/HA)_3(PAH/ALP)_5$ multilayers. (B) Typical C 1s and N 1s peaks recorded by XPS on (top) $(PAH/ALP)_5$ and (bottom) $(Col/HA)_3(PAH/ALP)_5$ multilayers prior to (see label "LbL") and after immersion in the mineralization solution (pH 7.4, 37 °C) during 1, 6, 16, 24, 48 and 96 h, as indicated. (C) C_{ox} vs $N_{399.8}$ measured by XPS on (■) $(PAH/ALP)_5$ and (●) $(Col/HA)_3(PAH/ALP)_5$ multilayers prior to and after mineralization.

The concentration of C_{ox}, characteristic of the protein adlayer, and Si, characteristic of the underlying support (silicon wafer), were then plotted together (Figure 4.5A and C) and compared to the evolution of the molar concentrations of calcium and phosphorus, characteristic of CaP compounds (see Figure 4.5B and D). For $(PAH/ALP)_5$ multilayers, the measurements show that the surface molar concentration of C_{ox} decreased markedly and that of silicon increased until 24 h of immersion (Figure 4.5A). The plateau observed in the C_{ox} *vs* time plot after 24 h was accompanied by a slight decrease of Si surface molar concentration (Figure 4.5A), most probably due to a weak screening effect because of the formation of the CaP mineral layer, as observed by AFM after 48 and 96 h of mineralization (see Figure 4.3F

and G). This relatively low effect may suggest the formation of a thin and/or discontinuous mineral layer.

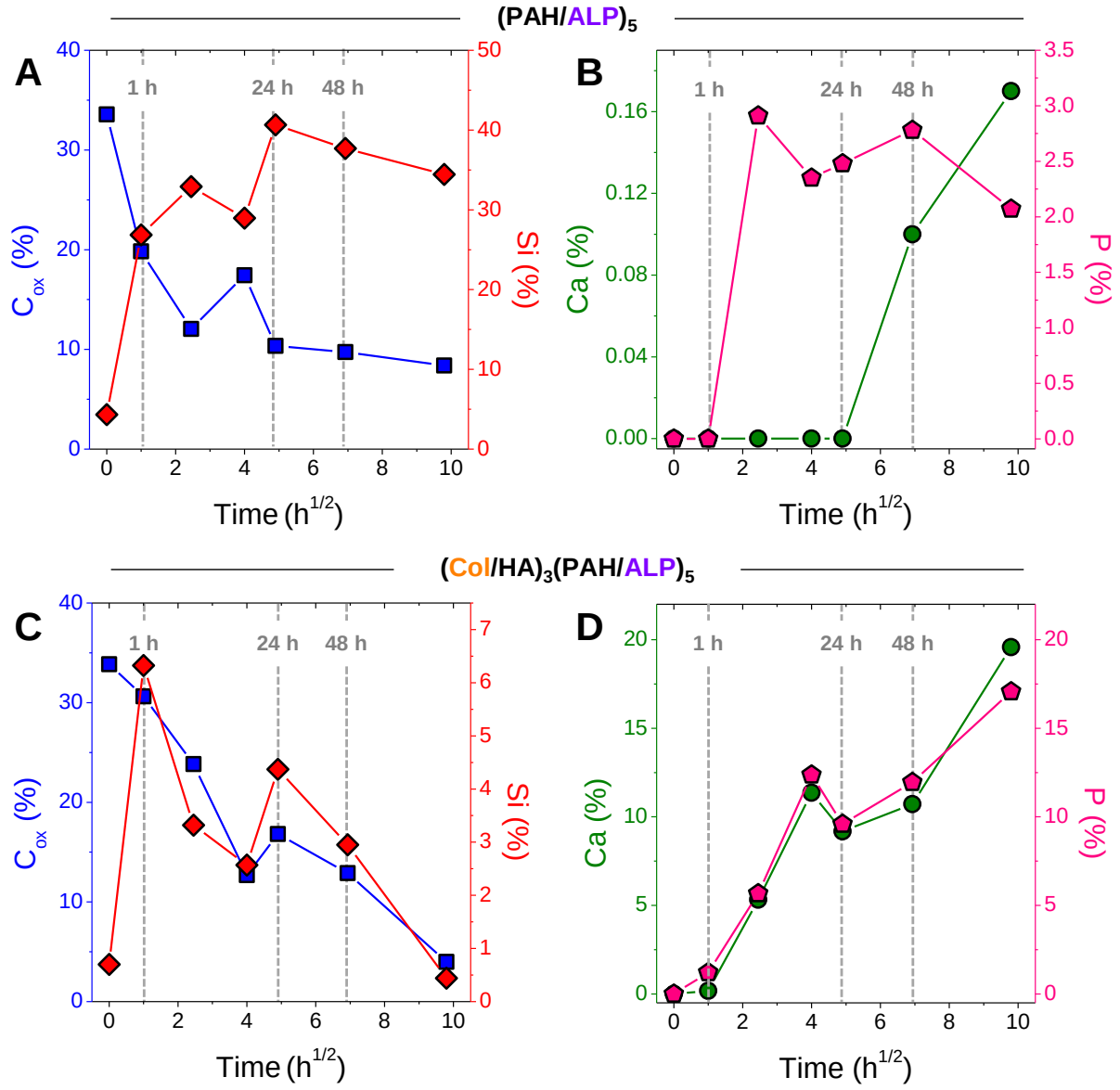

Figure 4.5 Evolution of the surface concentrations (mole fraction (%) computed over the sum of all elements except hydrogen), measured by XPS, of oxidized carbon (C_{ox}, ■), silicon (Si, ◆), Calcium (Ca, ●) and phosphorus (P, ⬟) recorded on (A, B) $(PAH/ALP)_5$ and (C, D) $(Col/HA)_3(PAH/ALP)_5$ multilayers as a function of the immersion time in the mineralization solution (pH 7.4, 37 °C).

XPS data recorded on $(Col/HA)_3(PAH/ALP)_5$ multilayers after immersion in the mineralization solution provided different trends (Figure 4.5C and D). Results showed, after 1 h, a weak decrease of C_{ox} and a noteworthy increase of the concentration of silicon. These opposite trends,

observed at early-stage immersion, may be associated with a reorganization of the multilayers, a loss of adsorbed species or a combination of both phenomena. Further immersion in the mineralization solution led to a decrease of the surface molar concentration of both C_{ox} and silicon up to 16 h (Figure 4.5C). This evolution is consistent with the formation of a mineral layer and is supported by the noticeable increase of both calcium and phosphorus concentrations at the same time (Figure 4.5D). Between 24 h and 96 h of immersion, the molar concentrations of elements show a drop for C_{ox} and silicon and a clear increase for calcium and phosphorus.

2.3 Growth mechanism of the mineral layer

Early stages

The origin of the activity loss that was evidenced on the $(PAH/ALP)_5$ multilayer, after the first use cycle, can be attributed to the desorption of enzymes during the immersion in the media where operational activities were performed (see section *2.1*). This desorption of enzymes during the immersion of the $(PAH/ALP)_5$ multilayer in the mineralization solution was also supported by the XPS measurements. Indeed, as detailed in section *2.2.2*, for $(PAH/ALP)_5$ multilayers, the surface molar concentration of C_{ox} decreased markedly (Figure 4.5A) and that of silicon increased during the first 24 h after the immersion of the multilayer. This evidences the loss of bio-organic materials, particularly adsorbed proteins, thus enhancing the signal originating from the underlined silicon wafer. This is consistent with the AFM images showing the progressive disappearance of globular particles, most likely enzymes from 1 to 16 h of mineralization (Figure 4.3B-D).

Regarding the $(Col/HA)_3(PAH/ALP)_5$ system, even though the desorption phenomenon was confirmed by activity measurements and XPS data, similarly to $(PAH/ALP)_5$ multilayers, the evolution of the surface topography, at early stages, deserves a particular attention. It revealed, after 1 h of immersion, typical collagen fibrils (Figure 4.3J), probably hidden, on the non-immersed sample, by the subsequent $(PAH/ALP)_5$ multilayers (Figure 4.3I), and the appearance of mineral particles, particularly located onto the fibrils (Figure 4.3J).

To look deeper into the origin of the desorption phenomenon observed up to 24 h of immersion for $(PAH/ALP)_5$ and 1 h for $(Col/HA)_3(PAH/ALP)_5$) multilayers, further experiments were performed by AFM (Figure 4.6). For this purpose, multilayers were incubated in different aqueous solutions for 24 h, while maintaining the pH and temperature as in the mineralization solution. These solutions consisted of ultrapure water (with a pH adjusted to 7.4), a solution containing $CaCl_2$ (11.4 mM) and a solution containing the enzyme substrate, α-glycerol

phosphate (Sub-Mg, 7 mM). Results show that the immersion of $(PAH/ALP)_5$ or $(Col/HA)_3(PAH/ALP)_5$ multilayers (Figure 4.6A and B) in water (Figure 4.6C and D) or in the solution containing Ca^{2+} (Figure 4.6E and 6F) did not induce any clear change of their morphologies compared to the initial surfaces (Figure 4.6A and B). By contrast, the incubation in α-glycerol phosphate solution led to noticeable changes in the morphology of the studied multilayers. On $(PAH/ALP)_5$ multilayers, AFM image shows a significant decrease of the surface density of the colloidal particles (Figure 4.6G), similarly to what is observed at early stages of incubation (see Figure 4.3B). On the $(Col/HA)_3(PAH/ALP)_5$ multilayers, the incubation in α-glycerol phosphate solution led to significant changes of the surface topography, revealing fibrillar nanostructures typical of collagen assemblies (Figure 4.6H). The presence of colloidal particles with comparatively low and high surface coverage was also observed on $(PAH/ALP)_5$ and $(Col/HA)_3(PAH/ALP)_5$ multilayers, respectively, after their incubation in the α-glycerol phosphate solution. Their average heights are 17.0 ± 3.6 nm (Figure 4.6G, n = 50) and 16.9 ± 4.01 nm (Figure 4.6H, n = 50), which are close to the hydrodynamic diameter of ALP in solution (17.9 ± 7.8 nm [11]). These observations suggest that the colloidal particles observed in Figure 4.6G and H correspond to ALP enzymes, most probably in the form of dimer, and support the fact that a higher amount of enzymes remains retained in $(Col/HA)_3(PAH/ALP)_5$ compared to $(PAH/ALP)_5$ multilayers.

Based on these results, the phenomenon mainly responsible for the desorption of the enzymes becomes clearer: it seems to be due to the release of phosphate ions through the enzymatic conversion of the glycerol phosphate within the multilayers, leading then to the screening of the electrostatic interactions originally involved in the LbL assembly. Indeed, the enzymes seem to be bound strongly enough, so that they do not desorb when immersed in water (Figure 4.6C and 6D) nor in presence of divalent ions such as Ca^{2+} (Figure 4.6E and 6F) but the local enzymatic release and accumulation of phosphate ions may exceed a critical ionic strength threshold above which electrostatic interaction between enzymes and positively charged polyelectrolyte are screened enough by ions to lead to their disassembling.

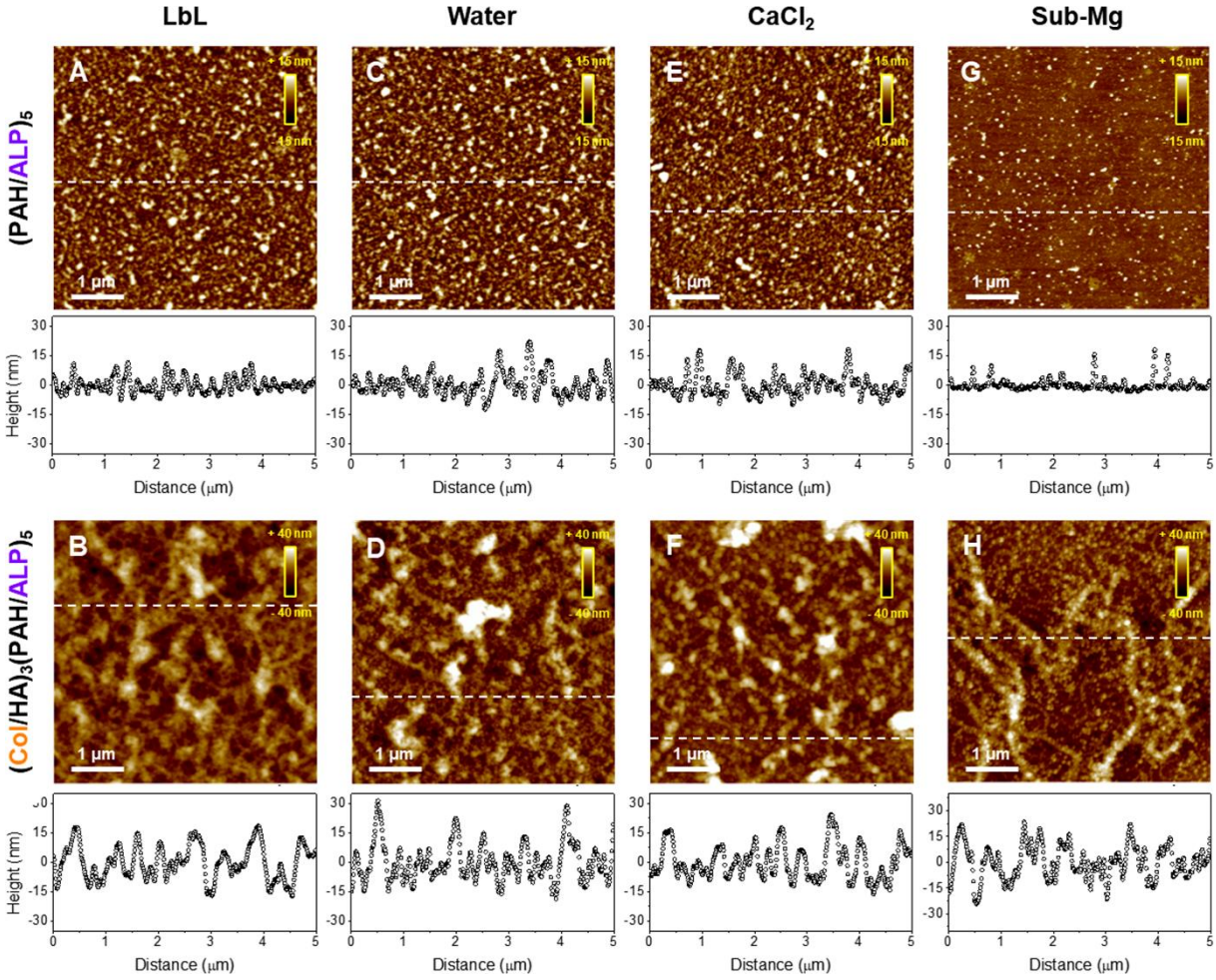

Figure 4.6 Multilayers immersed in different solutions. Representative AFM height images recorded on (A, C, E, G) $(PAH/ALP)_5$ and (B, D, F, H) $(Col/HA)_3(PAH/ALP)_5$ multilayers (A, B) prior to and after the immersion in (C, D) ultrapure water (pH adjusted to 7.4), (E, F) a solution containing $CaCl_2$ (11.4 mM) and (G, H) a solution containing the enzyme substrate, α-glycerol phosphate (Sub-Mg, 7 mM). Line scans were taken at the locations indicated by dashed lines.

Mineral layer morphology at the nanoscale

The activity of embedded enzymes leads to the release of phosphate ions within the multilayers. When the saturation of calcium phosphate is reached at the interface, the generation of more phosphate ions lead there to the formation of CaP by reaction with the free Ca^{2+} ions, as it can be observed by AFM in Figure 4.3E for the $(PAH/ALP)_5$ system. This mineralization is also responsible for the increase of the calcium and phosphorus concentrations at the surface, as measured by XPS (Figure 4.5B). However, a significant delay time is observed between the generation of phosphate ions and the formation of CaP compounds (see molar concentrations of P and Ca between 1 and 24 h, Figure 4.5B), probably due to the chemical environment at the solid/liquid interface that does not favor CaP nucleation. However, this delay time seems

to be significantly reduced when collagen fibrils are present within the multilayers. Indeed, the formation of CaP particles was noticeably faster: they appear between 1 and 6 h for $(Col/HA)_3(PAH/ALP)_5$ multilayers, whereas they were observed only after 24 h for$(PAH/ALP)_5$ multilayers. In particular, it can be noted that the increase of the molar concentration of P, observed after 1 h of mineralization, is concomitant with the increase of Ca in the case of $(Col/HA)_3(PAH/ALP)_5$ multilayers (Fig. 4.5D, Table S4.1, Supporting Information).

This difference of mineral formation between the studied multilayer systems could be explained by two main reasons. First, the enzymatic activity of the $(Col/HA)_3(PAH/ALP)_5$ system is significantly higher compared to $(PAH/ALP)_5$ (Figure 4.2A), which could be explained, in particular, by the fact that a higher amount of enzymes remains at the surface, most probably due to the high affinity of ALP and collagen. Second, CaP mineralization can be favored due to the presence collagen, as already hypothesized in many articles in the literature, which is supposed to be due to surface energy considerations [15]. Indeed, the AFM images show a preferable formation of CaP particles onto the collagen fibrils (Figure 4.3J and K).

This latter hypothesis was scrutinized by investigating by AFM the very first moments of the mineralization, i.e. when CaP particles start to appear on the $(Col/HA)_3(PAH/ALP)_5$ multilayers. A close look at the changes of the mineral layer morphology between 1 and 6 h of mineralization is presented in Figure 4.7. AFM images were recorded at different magnifications to get more precise information regarding the CaP particle features, their distribution on the surface and their localization to the regard of collagen fibrils. These images showed, first, the typical supramolecular organization of collagen fibrils, which remain visible during the mineralization period, i.e. over 6 h of incubation (Figure 4.7A-D). Moreover, the presence of CaP particles, more obvious at higher magnification (Figure 4.7E-H) is confirmed over the studied period, and the images show a clear increase of the surface coverage between 1 and 6 h of mineralization. Interestingly, at the earliest stage of mineralization, CaP particles are shown to be preferentially located onto the collagen fibrils (Figure 4.7E). Their heights can be measured in a reliable way as many particles remained isolated (see scan line in Figure 4.7I), yielding bimodal distributions with average heights equal to 14.2 ± 5.2 and 22.0 ± 2.1 nm (see histograms in Figure 4.7I and J). Results showed that the height of the CaP particles did not change significantly between 1 and 3 h of mineralization. By contrast, after 5 h, two main features can be noticed. First, the surface coverage increased significantly, and particles

appeared both onto and in-between the fibrils (Figure 4.7G). Second, the mean height of these particles increased markedly around 22.5 nm ± 6.5 nm and the particles came in close contact with each other, while preserving their spheroid shape (Figure 4.7K). The extensive presence of CaP particles totally covering collagen fibrils and present in-between the fibrils was concomitant with an abrupt increase of the molar concentration of calcium and phosphorus (Table S4.1, Supporting Information). After 6 h of mineralization, an evolution of the morphology of individual CaP particles can be observed (Figure 4.7L), but this evolution does not provide further clue on their crystal structure.

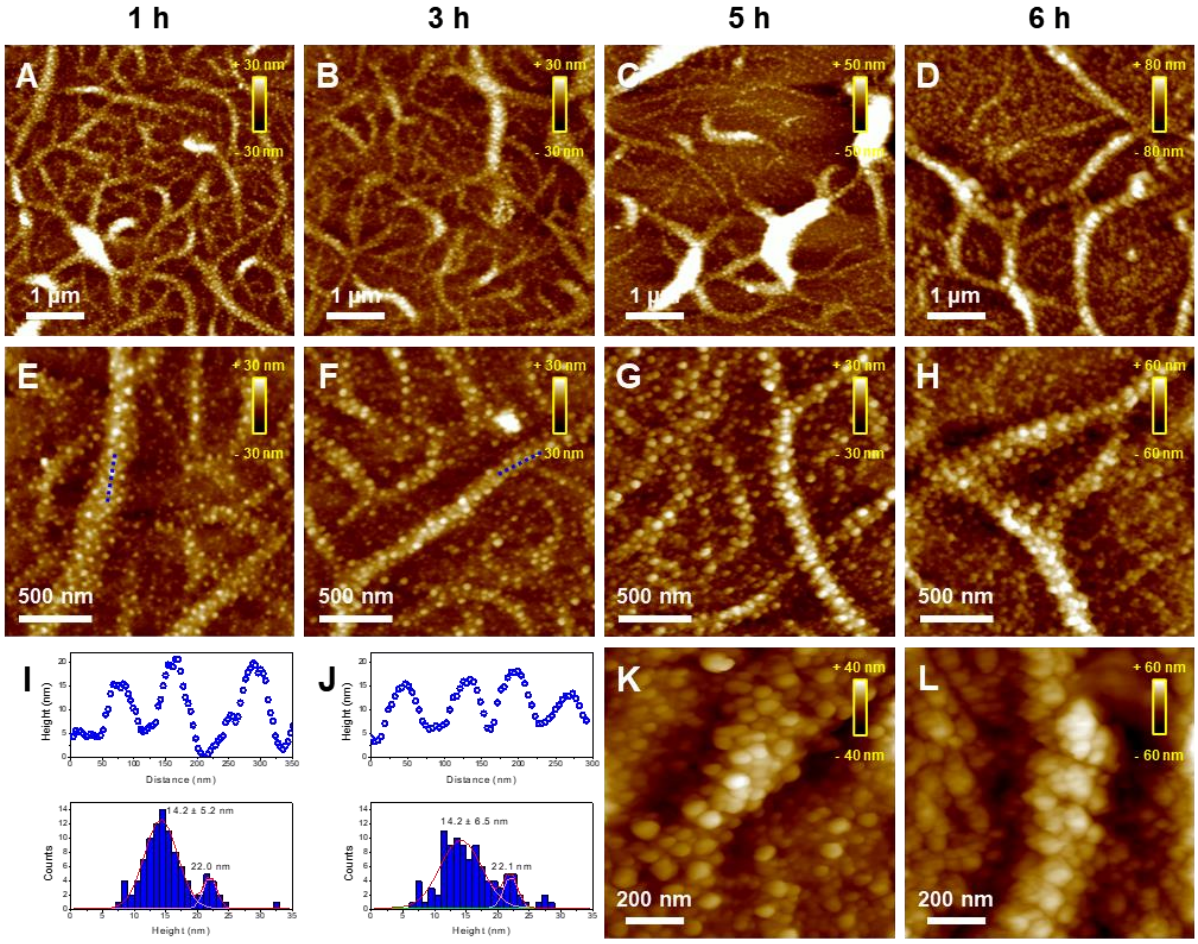

Figure 4.7 Early stage of CaP mineralization on $(Col/HA)_3(PAH/ALP)_5$ multilayers. Representative AFM height images recorded on $(Col/HA)_3(PAH/ALP)_5$ multilayers after immersion in the mineralization solution (pH 7.4, 37 °C) during (A, E) 1 h, (B, F) 3 h, (C, G, K) 5 h and (D, H, L) 6 h. (I, J) Line scans taken at the locations indicated by dashed lines in the height images E and F, respectively, and histograms of particle heights (n = 50) corresponding to the samples showed in images E and F, respectively.

The above observations clearly indicate then that the growth mechanism of the CaP layer is strongly modified by the presence of the $(Col/HA)_3$ multilayers, and their presence within the multilayers leads to an extensive mineralization of the surface (Figure 4.3L-O). Specifically, collagen fibrils play a pivotal role in the growth mechanism of the biomimetic mineral layer (Figure 4.7), and its role seems to consist, in particular, in improving the retention of enzymes and providing a favorable environment for CaP nucleation and growth. It is noteworthy that the partial desorption of enzymes, which occurs at early stage, can be considered in the mineralization process, as the enzymes remain active in the solution (Figure S4.2, Supporting Information). This suggests that minerals could be formed in the solution because of the activity of the free enzymes, following a homogenous catalysis mechanism studied elsewhere [16], then deposit on the solid surface. However, this scenario seems to be unlikely, because in the studied conditions, the enzyme-assisted mineralization in homogenous phase has been shown to lead to the rapid formation of amorphous globular particles with a mean diameter around 280 nm [17], that were not observed by AFM. Instead, the progressive uniform formation and growth of mineral particles were observed by AFM, preferentially located on collagen fibrils (Figure 4.7).

Mineral layer morphology at the microscale

The role of collagen fibrils to induce more extensive mineralization on the surface is also confirmed by SEM images, which provide a relevant view on the layer morphology at the microscale. For $(Col/HA)_3(PAH/ALP)_5$ systems, results showed the presence of collagen fibrils organized into a network, where mineral particles are clearly trapped (Figure 4.8A). Moreover, the presence of isolated spheroid-shaped microparticles is observed (Figure 4.8B), and confirmed on several images recorded at different locations at the surface (data not shown). Their mean diameter was ranging from 2.8 µm to 8.2 µm, and their composition was determined by EDS analysis (Figure 4.8C), revealing a Ca/P ratio of 1.28 ± 0.08, which remains close to the value expected for amorphous calcium phosphate. After 96 h of mineralization, SEM images indicate that an extensive mineralization occurred, revealing fully mineralized collagen fibrils (Figure 4.8D). The isolated microparticles remained, also, visible and their mean diameter showed lower polydispersity (11.5 ± 2.5 µm). Interestingly, after first displaying a smooth surface after 48 h (Figure 4.8B), the surface topography of these microparticles became rough after 96 h, due to the presence of a platelet-like nanometric substructure (Figure 4.8E). Furthermore, the composition of these particles, as deduced from EDS analysis (Figure 4.8F), yielded a Ca/P ratio equal to 1.87 ± 0.19, which is close to the

value expected for carbonated-hydroxyapatite. The intensity of the Si signal, originating from the silicon wafer, is surprisingly higher after 96 h of mineralization (Figure 4.8F) compared to the sample obtained after 48 h (Figure 4.8C). This may be explained by the hollow structure of the microparticles, as observed in several SEM images (see Figure S4.3, Supporting Information). Comparable apparent hollow structure was obtained on CaP particles through homogeneous approaches involving a variety of complexing agents (see [18, 19] and references therein). In the present study, the situation is different as the mineralization process is driven on the solid surface, where enzymes generate phosphate ions locally and collagen fibrils provide a favorable environment for the nucleation and growth of CaP particles. The growth of such large microstructures with hollow feature is, indeed, unexpected, and the question clearly deserves further investigations.

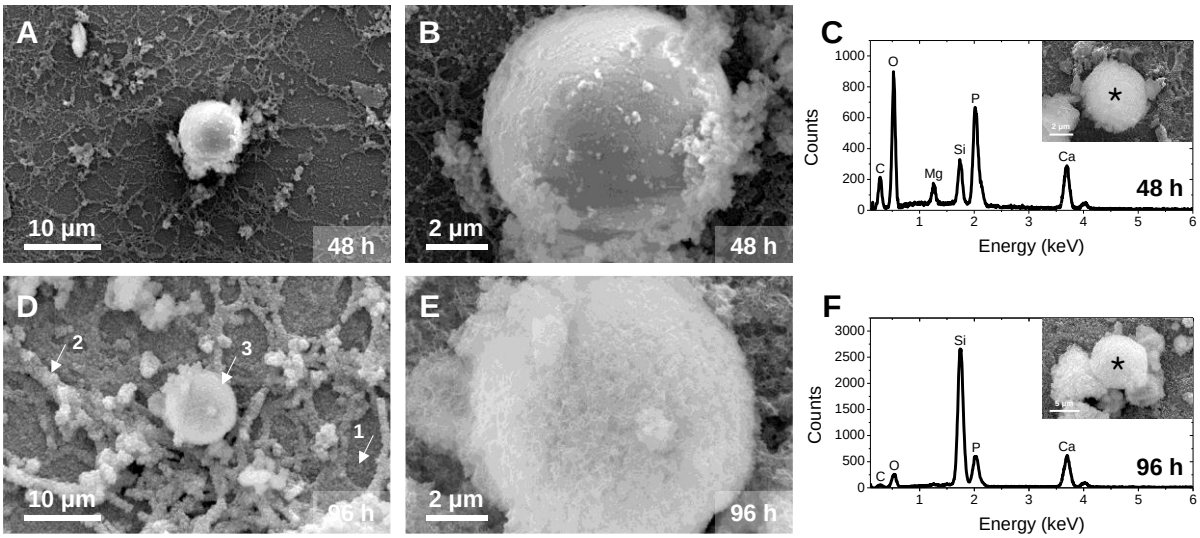

Figure 4.8 SEM images recorded after the build-up of $(Col/HA)_3(PAH/ALP)_5$ multilayers and subsequent immersion in the mineralization solution (pH 7.4, 37 °C) during (A, B) 48 h and (D, E) 96 h. (C, F) EDS spectra recorded on the location indicated in the SEM image (inset, *) on $(Col/HA)_3(PAH/ALP)_5$ multilayers after (C) 48 h and (F) 96 h of mineralization.

The global view provided by SEM images of the $(Col/HA)_3(PAH/ALP)_5$ multilayers, mineralized for 96 h, reveal the presence of a coating fully covering the underlined silicon support and exhibiting different morphologies (see arrows in Figure 4.8D): (i) flat and continuous layer (label 1), which is expected to be the layer probed by AFM, (ii) mineralized collagen fibrils organized into a network-like structure (label 2) and (iii) mineralized microparticles with hollow structure (label 3).

The mineral layer grown over $(Col/HA)_3(PAH/ALP)_5$ multilayers provides a hybrid coating, which is particularly promising, in terms of composition and morphology, for the creation of environments mimicking the extracellular matrices of hard biomineralized tissues. Because the approach is based on the LbL method, the coatings may be applied to various types of materials regardless of their surface composition and morphology. Moreover, owing to the versatility of LbL, the procedure may be extended to embed other natural polyelectrolytes with specific properties (e.g. to promote cell adhesion), or to incorporate bioactive molecules, such as non-collagenous proteins, bone morphogenic proteins, or drugs to be delivered.

2.4 Probing intra- and extrafibrillar mineralization

Mineralization at room temperature

As described above, the enzyme-assisted mineralization process in the presence of collagen was characterized in the dried state after a given mineralization time. This provided relevant information in the selected time to probe the role of collagen in the formation of the mineral on the surface. However, based on the findings, we can't conclude about any possible mineralization in the intrafibrillar space. This motivated the monitoring of CaP mineralization in situ real-time by AFM in liquid. This method allows to study biological sample in the native state and to monitor the dynamic process such as conformational change in real-time at a high temporal resolution. In this study, the CaP mineralization was monitored by AFM in liquid phase at ambient conditions based on the instrumental setup. Accordingly, the mineralization of $(Col/HA)_3(PAH/ALP)_5$ multilayers was firstly investigated in the dried state for comparison with the previous result obtained at 37 °C. The catalytic activity of $(Col/HA)_3(PAH/ALP)_5$ multilayers was investigated based on the conversion of pnpp to pnp by the action of enzymes at RT (Figure S4.4, Supporting Information). The effective activities obtained at RT yield values of 1.20 ± 0.08 μM $min^{-1} \cdot cm^{-2}$ corresponding to an activity about 4 times lower when the activity measured at 37 °C in the section *2.1* in this chapter. The loss of catalytic activity was also observed at RT after the first use. The residual activities were about 23 % of initial values (Figure S4.4B, Supporting Information) as similar as the value obtained at 37 °C at the third uses. After, the formation of CaP minerals on $(Col/HA)_3(PAH/ALP)_5$ multilayers was investigated by AFM after a given mineralization time ranging from 30 min to 3 h (Figure 4.9) in a similar way as performed at 37 °C (Figure 4.7). The immersion of the $(Col/HA)_3$ $(PAH/ALP)_5$ multilayers (Figure 4.9A and E) in the mineralization solution for 30 min showed the typical fibrillar assemblies of collagen with D-period (66.4 ± 5.5 nm) as indicated with dashed lines (Figure 5.2F). Interestingly, globular colloidal particles (height 4.88 ± 2.25 nm,

n=50) appeared seemingly preferentially located near the fibrils (Figure 4.9B and F) as shown in the section *2.2* and *2.3* in this chapter. After 1 h of mineralization, the AFM images showed the disappearance of d-spacing and lower differences of heights on collagen fibrils (Figure 4.9G and line scans). After 3 h of mineralization, the AFM images showed clear colloidal particles (height: 11.90 nm ± 4.21 nm, n=50) accumulated along the collagen fibrils (Figure 5.2 D and H). The location of these particles appeared slightly different from the globular ones observed after 30 min, because the particles were closer to each other, specifically located on the collagen fibrils.

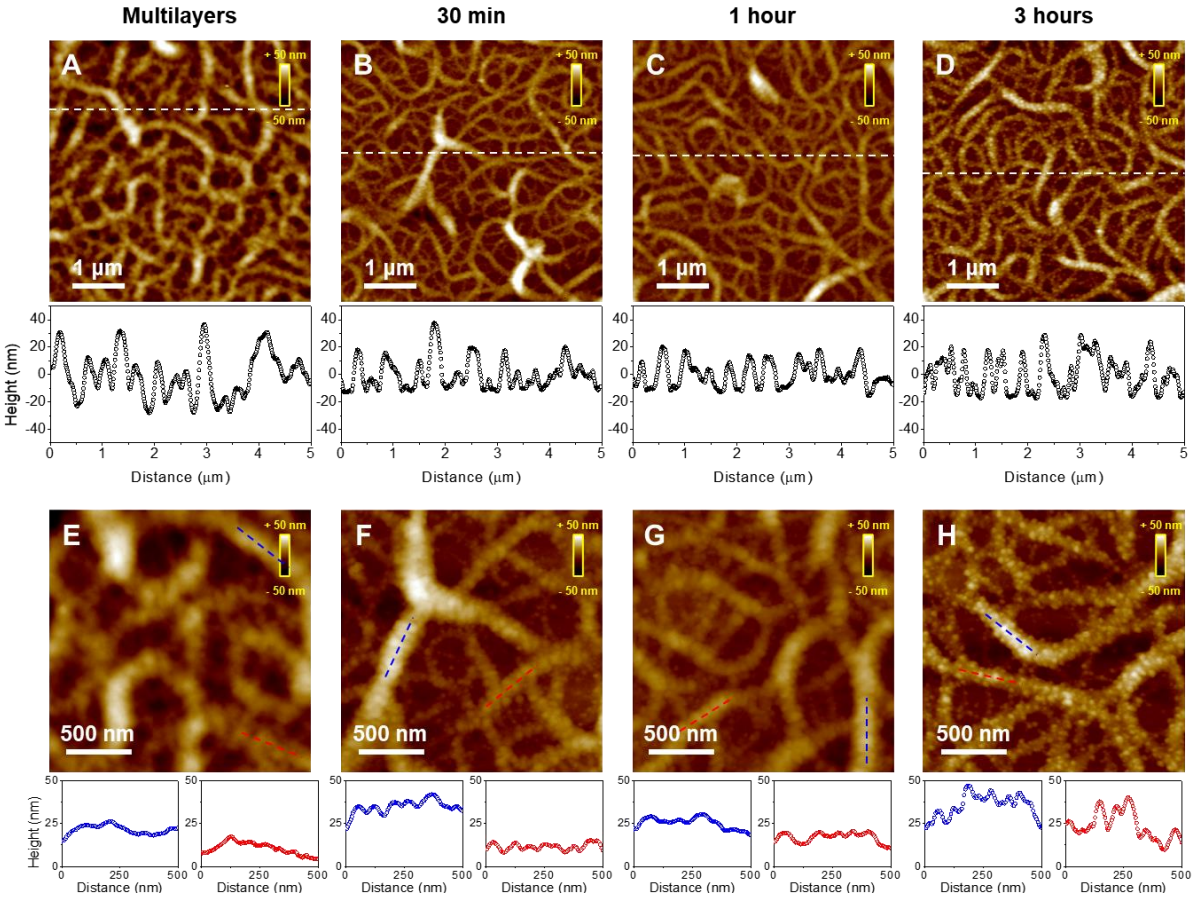

Figure 4.9 CaP mineralization on $(Col/HA)_3(PAH/ALP)_5$ multilayers at RT. AFM height images recorded in the dried state on $(Col/HA)_3(PAH/ALP)_5$ multilayers (A, E) prior to (as multilayers) and after immersion in the mineralization solution (pH 7.4) during (B, F) 30 min, (C, G) 1 hour and (D, H) 3 hours. Line scans were taken at the locations indicated by dashed lines.

The comparison of CaP mineralization on $(Col/HA)_3(PAH/ALP)_5$ multilayers at RT and 37 °C showed similar trend regarding (i) the structure and organization of the multilayers, specifically collagen fibrils and (ii) the appearance of colloidal CaP particles on the collagen fibrils. From

this point of view, it can be concluded that the temperature did not influence noticebly the mineralization process.

Real-time monitoring of the mineralization

The CaP mineralization on $(Col/HA)_3(PAH/ALP)_5$ multilayers at RT was monitored in real-time by AFM in the liquid phase (Figure 4.10). The monitoring is performed by replacing the water drop deposited on the multilayer with a drop of mineralization solution containing substrate (7 mM) and $CaCl_2$ (11.4 mM) at pH 7.4 at RT (t = 0) as described in section *3.4.1* in Chapter 2. The first measurements were few minutes later, a time required for the stabilization of the signal. Results show the appearance of particles (Figure 4.10A, 36 min) with a clear evolution of their surface density and size. From the initial stage, the number of particles was counted from 2 x 2 μm^2 images over time (Figure 4.10 C). Based on the evolution of their number, the CaP mineralization process seems to be divided into three stages: (I) the time interval between t =0 and the induction time which is the time required before the initiation of the mineralization, (II) a linear evolution of particles number is observed up to 36 min of mineralization and (III) saturation of the number of particles. In the last stage, the growth of particles is more dominant than the generation of new particles. However, it must be kept in mind that the growth of particles also occurs during the second stage. During the mineralization, the change the size of collagen filaments and fibrils is also an interesting point. The evolution observed on filaments was significant as shown in Figure 4.10D (marked as a dashed line in Figure 4.10A). The height and diameter of the filament were dramatically enlarged by mineralization each from 23 nm and 79 nm to 82 nm and 141 nm. The relative evolution of the height and width of the selected filament may appear more clearly if it is expressed using the following equation:

$$\Delta_h = \frac{h - h_0}{h_0} \times 100$$

h: the height of the fibril at a given time (t)

h_0: the initial height of the fibril

This increase occurs over a mineralization time of about 90 min until the filaments of collagen are covered by minerals. Results show a huge increase of Δ_h after a delay time (~ 30 min). Following the same logical, the width of collagen filament is probed during the mineralization using Δ_w parameter defined as:

$$\Delta_w = \frac{w - w_0}{w_0} \times 100$$

where w is the width of the filament at a given time (t) and w_0 is the initial width of the filament. At these dimensions (Figure 4.10D) a convolution effect due to the AFM tip (radius ~ 10 nm) can be reasonably ruled out.

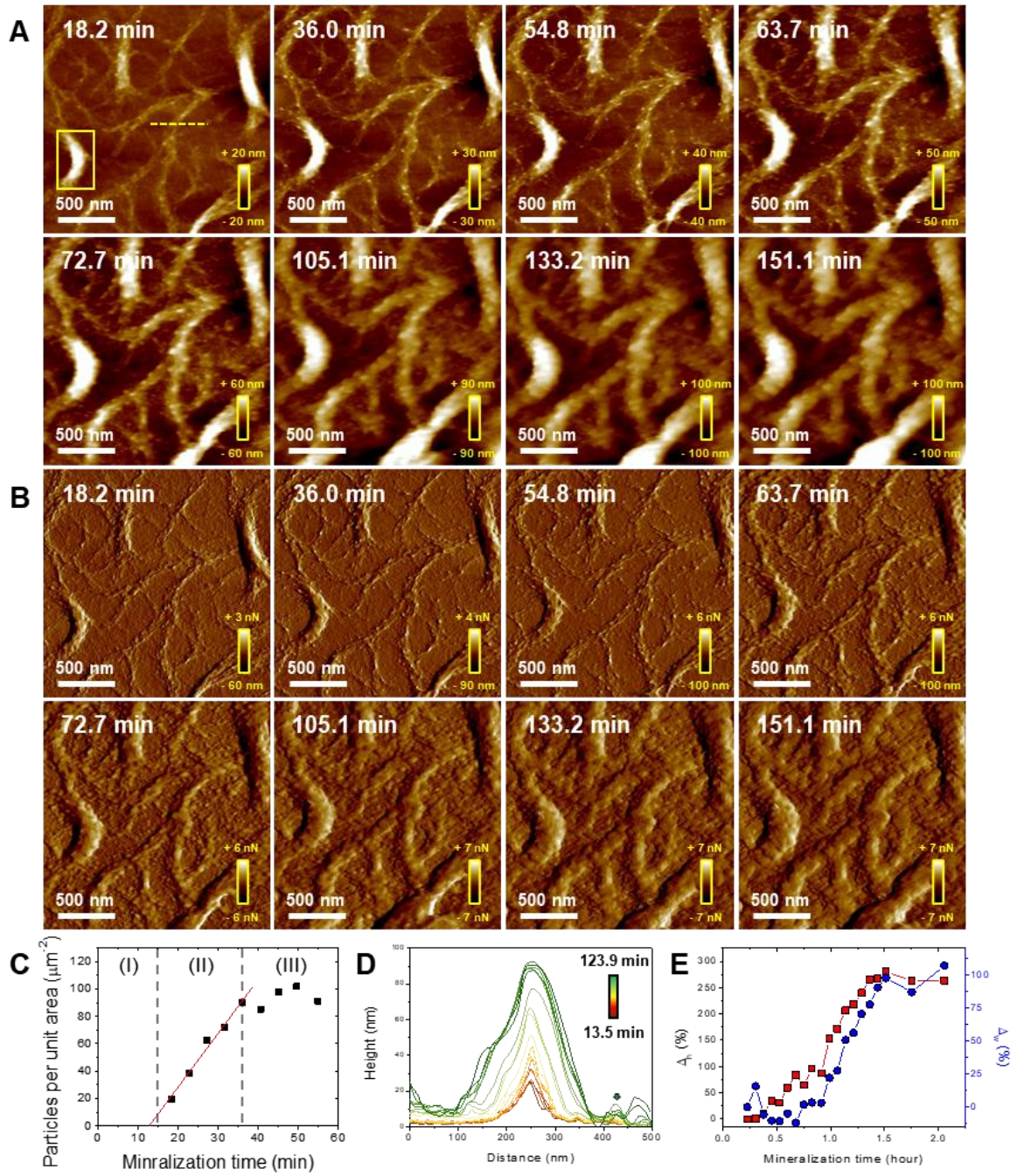

Figure 4.10 Real-time monitoring of CaP mineralization over $(Col/HA)_3(PAH/ALP)_5$ multilayers (A) height images (B) deflection error images (C) plot of particle numbers per unit area vs. mineralization time (D) accumulation of scanlines marked as dashed line in A (E) relative evolution of height and width of a fibril.

These findings showed, for the first time, real-time monitoring of CaP mineralization over multilayers with diverse collagen assemblies, filaments and fibrils (Figure 4.10, width: 50~150 nm, height: 5~55 nm). Further investigations were conducted by selecting the area locating larger fibrils (Figure 4.11, width: 95~800 nm, height: 20~212 nm). The mineralization with larger fibrils showed similar trends from the particle appearance and growth until the full coverage of fibrils. However, the particles on fibrils were observed after a delayed time compared to the previous monitoring. The enlargements of fibrils were well-observed as shown with accumulations of scanlines (Figure 4.11C and D). The relative evolution of the height and width of selected fibrils is also presented in Figure 4.11E which shows the height and width of fibrils increase roughly linearly during the mineralization. In this case, the enlargement of fibrils deserves particular attention. First, it appears that it is not due to swelling in liquid, as confirmed by a control experiment (Figure S4.5, Supporting Information). Indeed, the $(Col/HA)_3(PAH/ALP)_5$ multilayer placed under the substrate (7 mM) solution without $CaCl_2$ showed no significant changes in the size and shape of collagen fibrils. Second, during the enlargement of fibrils in the early stage, mineral particles were not observed, in contrast to what is shown in the dried state (Figure 4.9). This is confirmed by the evolution of the surface roughness, whether it is measured on collagen fibrils or around the fibrils (Figure 4.12). The values were obtained using the same formula as shown above for the calculation of Δ_h. The surface roughness increased prominently when it was measured around the fibrils, owing to the formation of CaP particles as expected. By contrast, the roughness suggests that collagen fibrils remained relatively stable throughout the mineralization process, indicating the mineralization occurs in the intrafibrillar space. If mineralization were to occur primarily on the fibril surfaces (extrafibrillar mineralization), it is expected to change the surface roughness of the collagen fibrils.

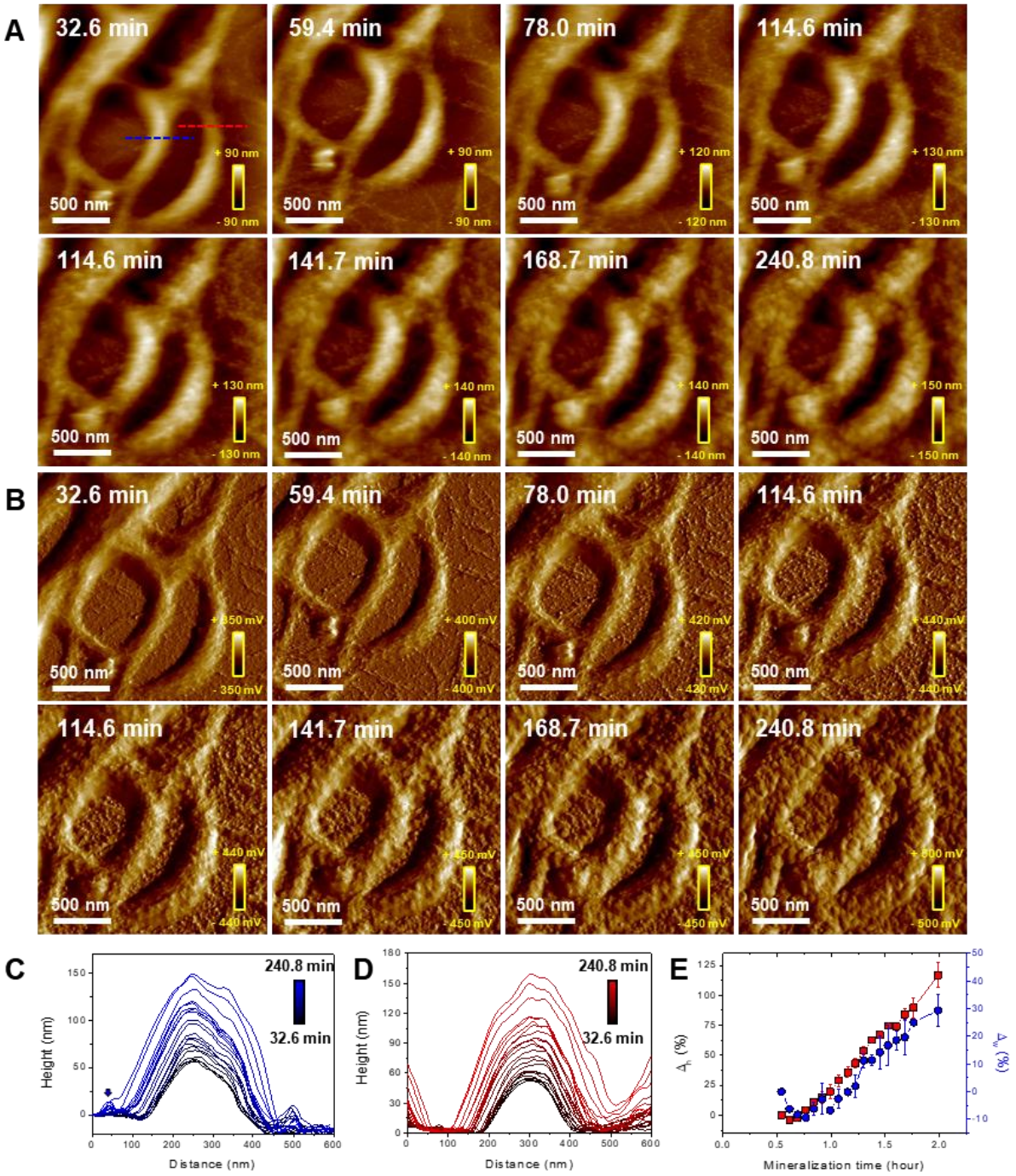

Figure 4.11 Real-time monitoring of CaP mineralization over $(Col/HA)_3(PAH/ALP)_5$ multilayers (A) height images (B) deflection error images (C, D) accumulation of scanlines marked as dashed line in A (E) relative evolution of height and width of a fibril.

These findings suggest that the mineralization occurs, first, within the fibrils (intrafibrillar) and then outside of the fibrils (extrafibrillar) following the mechanisms by which organisms form hard mineralized tissues. At early stages, and during the intrafibrillar mineralization, it appears that drying causes the shrinking of collagen fibrils and probably enhances the formation of CaP

particles, leading to their appearance after 30 min (Figure 4.9). This may explain the discrepancy observed between the dried and the hydrated state.

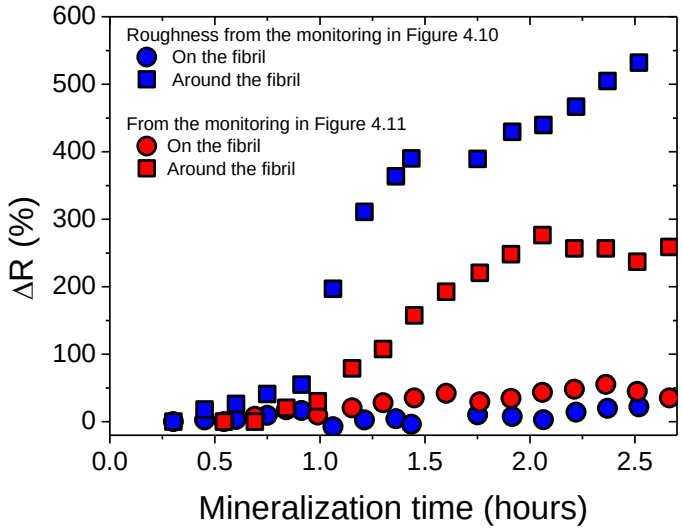

Figure 4. 12 The relative evolutions of roughness of multilayers and collagen fibrils.

3 Conclusion

In this work, a biomimetic system involving two proteins, an enzyme, the ALP, and type I collagen, was used to control the location and the kinetics of the CaP mineralization process. In order to confer on this system a high versatility regarding the kind of surface on which the mineral layer formation could occur, both proteins were embedded in a thin film by means of LbL assembly. Thereby, localized mineralization could occur at the surface, controlled in time and space by the enzymatic conversion of a substrate, α-glycerol phosphate, into phosphate ion, and directed by self-assembled collagen fibrils.

Through AFM and XPS measurements, the collagen fibrils were shown to play a pivotal role in the mineralization process. The enzymatic activity of the system and, thus, the rate of generated phosphate ions, increased in the presence of collagen, most probably due to the high affinity of enzymes with collagen fibrils, as observed in vivo. Results also showed the occurrence of initial desorption of some embedded enzymes that was more limited when collagen fibrils were present. Moreover, early-stage AFM measurements revealed the formation of colloidal CaP particles preferentially located onto the collagen fibrils. Then, the surface coverage increased significantly with mineral particles, which appeared both onto and in between the fibrils. Further mineralization led to a coating fully covering the support and

showing a flat and continuous layer covered with a dense network of mineralized collagen fibrils in addition to some mineralized microparticles. Real-time monitoring of the mineralization, performed by AFM in the liquid phase, suggests the occurrence of intrafibrillar mineralization followed by an extrafibrillar mineralization, both yields fully mineralized collagen fibrils.

4 References

1. Boudou, T., et al., *Multiple Functionalities of Polyelectrolyte Multilayer Films: New Biomedical Applications.* Advanced Materials, 2010. **22**(4): p. 441-467.
2. Osypova, A., et al., *Dual stimuli-responsive coating designed through layer-by-layer assembly of PAA-b-PNIPAM block copolymers for the control of protein adsorption.* Soft Matter, 2015. **11**(41): p. 8154-8164.
3. Zhang, S., et al., *Layer-by-layer assembly in nanochannels: assembly mechanism and applications.* Nanoscale, 2021. **13**(16): p. 7471-7497.
4. Alkekhia, D., P.T. Hammond, and A. Shukla, *Layer-by-Layer Biomaterials for Drug Delivery.* Annual Review of Biomedical Engineering, 2020. **22**(1): p. 1-24.
5. Zhang, Z., et al., *Layer-by-layer assembly methods and their biomedical applications.* Biomaterials Science, 2022. **10**(15): p. 4077-4094.
6. Richardson, J.J., et al., *Innovation in Layer-by-Layer Assembly.* Chemical Reviews, 2016. **116**(23): p. 14828-14867.
7. Zou, Z., et al., *Three-dimensional structural interrelations between cells, extracellular matrix, and mineral in normally mineralizing avian leg tendon.* Proceedings of the National Academy of Sciences, 2020. **117**(25): p. 14102-14109.
8. Oosterlaken, B.M., M.P. Vena, and G. de With, *In Vitro Mineralization of Collagen.* Advanced Materials, 2021. **33**(16): p. 2004418.
9. Dupont-Gillain, C.C., *Understanding and controlling type I collagen adsorption and assembly at interfaces, and application to cell engineering.* Colloids and Surfaces B: Biointerfaces, 2014. **124**: p. 87-96.
10. Colaço, E., et al., *Embedding Collagen in Multilayers for Enzyme-Assisted Mineralization: A Promising Way to Direct Crystallization in Confinement.* Biomacromolecules, 2021. **22**(8): p. 3460-3473.
11. Colaço, E., et al., *Enzyme-assisted mineralization of calcium phosphate: exploring confinement for the design of highly crystalline nano-objects.* Nanoscale, 2020. **12**(18): p. 10051-10064.
12. Narayanan, B., et al., *Self-Assembly of Collagen on Flat Surfaces: The Interplay of Collagen–Collagen and Collagen–Substrate Interactions.* Langmuir, 2014. **30**(5): p. 1343-1350.
13. Zhang, J., et al., *Natural polyelectrolyte films based on layer-by layer deposition of collagen and hyaluronic acid.* Biomaterials, 2005. **26**(16): p. 3353-3361.
14. Vittur, F., et al., *Alkaline phosphatase binds to collagen; a hypothesis on the mechanism of extravesicular mineralization in epiphyseal cartilage.* Experientia, 1984. **40**(8): p. 836-837.
15. Habraken, W.J.E.M., et al., *Ion-association complexes unite classical and non-classical theories for the biomimetic nucleation of calcium phosphate.* Nature Communications, 2013. **4**(1): p. 1507.
16. Colaço, E., et al., *Calcium phosphate mineralization through homogenous enzymatic catalysis: Investigation of the early stages.* Journal of Colloid and Interface Science, 2020. **565**: p. 43-54.

17. Lee, J., et al., *Kinetic study of calcium phosphate mineralisation in biomimetic conditions: An enzymatic model approach.* Colloids and Surfaces B: Biointerfaces, 2023. **226**: p. 113290.
18. Qi, C., et al., *Calcium-based biomaterials for diagnosis, treatment, and theranostics.* Chemical Society Reviews, 2018. **47**(2): p. 357-403.
19. Qi, C., et al., *Biomolecule-assisted green synthesis of nanostructured calcium phosphates and their biomedical applications.* Chemical Society Reviews, 2019. **48**(10): p. 2698-2737.

5 Supporting Information

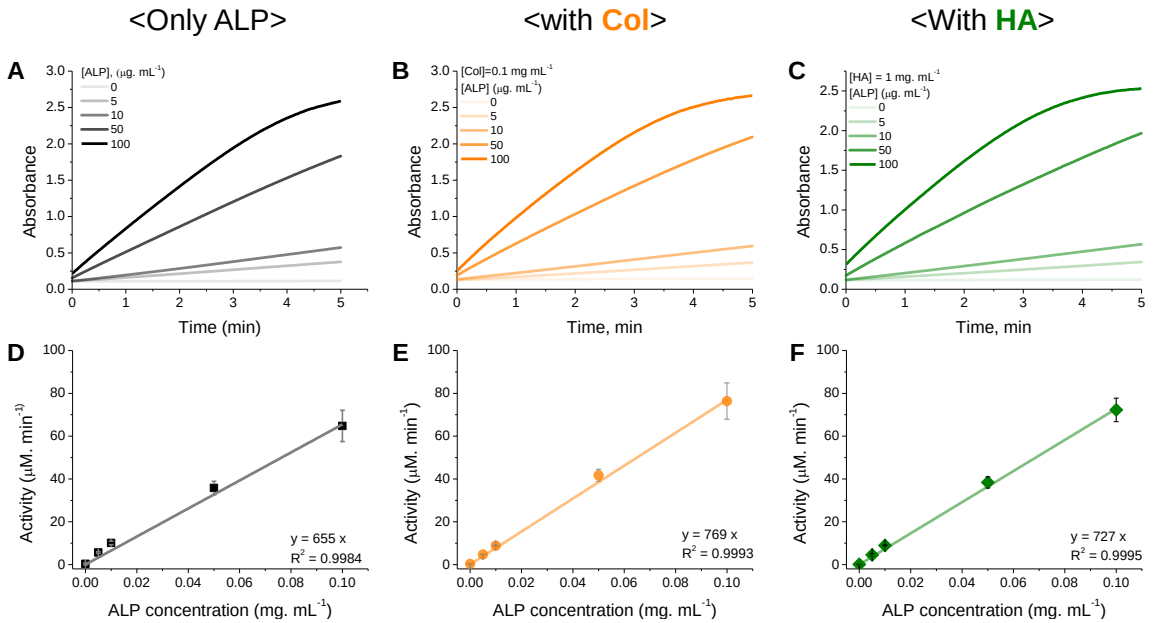

Figure S4.1. Measurements of the catalytic activity of ALP in aqueous solution ($CaCl_2$ = 11.4 mM, pH = 7.4, 37 °C) in the different conditions, as indicated. (A-B) Evolution of the absorbance as a function of time at different enzyme concentration (0, 5, 10, 50 and 100 = µg·mL^{-1}), (A) as such, or in the presence of (B) collagen (0.1 mg·mL^{-1}) or (C) hyaluronic acid (1 mg·mL^{-1}). (D-F) Specific activity of ALP in these different conditions.

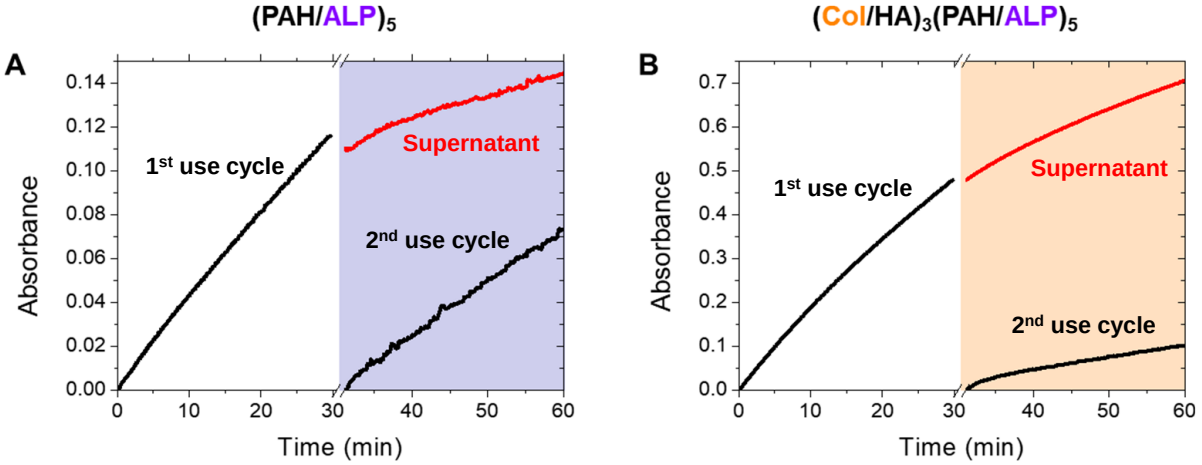

Figure S4.2. Evolution of the absorbance at 410 nm vs time due to the activity of ALP embedded within $(PAH/ALP)_5$ or $(Col/HA)_3(PAH/ALP)_5$ multilayers after one and two use cycles, or in the supernatant, as indicated.

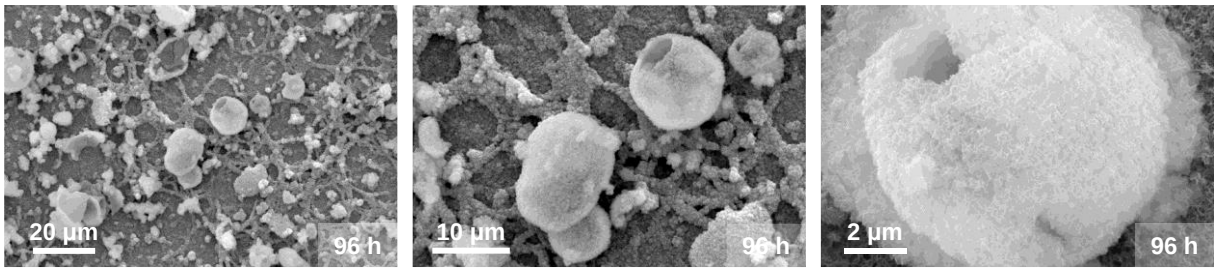

Figure S4.3. SEM images recorded at different magnitudes on $(Col/HA)_3(PAH/ALP)_5$ multilayers mineralized during 96 h (pH 7.4, 37 ℃).

Table S4.1. Surface concentration (mole fraction (%) computed over the sum of all elements except hydrogen) of elements determined by XPS $(Col/HA)_3(PAH/ALP)_5$ multilayers after 1; 3; 5 and 6 h of immersion in the mineralization solution (pH 7.4, 37 ℃).

	C	N	O	Si	Ca	P	Mg
NM	67.3	14.06	17.33	0.70	bdl	bdl	bdl
1 h	60.98	12.13	18.96	6.33	0.35	1.22	0.18
3 h	58.29	15.47	22.37	2.72	0.11	1.04	bdl
5 h	54.67	9.76	25.05	3.33	3.38	3.28	0.55
6 h	49.94	5.26	27.11	3.32	5.33	5.67	0.82

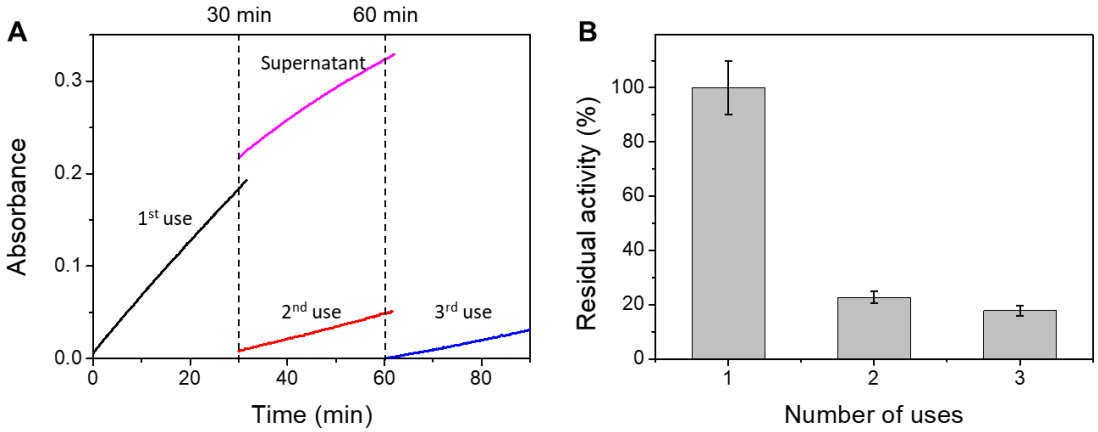

Figure S4.4. Catalytic activity of $(Col/HA)_3(PAH/ALP)_5$ multilayers measured at room temperature. (A) Typical evolution of the absorbance at 410 nm due to the production of pnp vs time. (B) Residual activity of ALP embedded within the multilayers, calculated as the percentage of initial activity after repeated use and rinsing cycles.

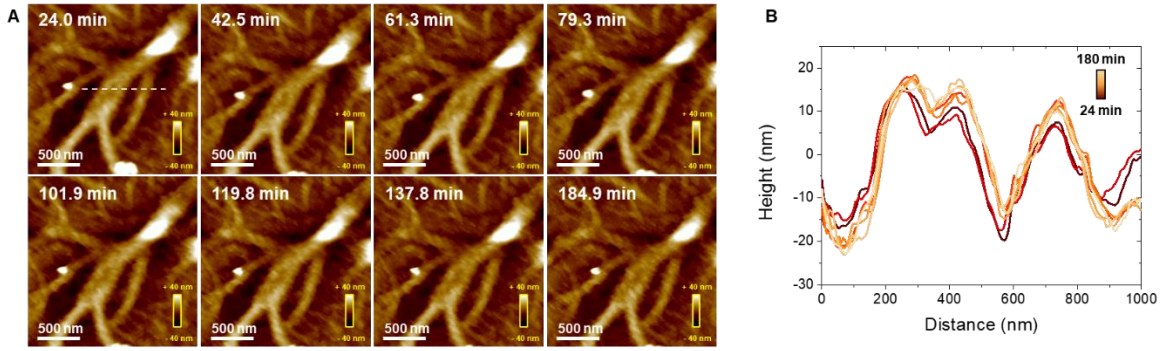

Figure S4.5 In situ monitoring of $(Col/HA)_3(PAH/ALP)_5$ under the substrate (7 mM) solution. (A) AFM height images over time. (B) Overlap of cross-section from a dash ed line in (A) over time.

Conclusion and perspective

In this thesis, enzyme-assisted CaP mineralization inspired by biological processes was investigated especially focusing on the two biological features: (i) homeostasis and (ii) compartmentalization. The use of ALP generated the orthophosphate in situ, simulating the regulation of phosphate levels in ECM. The incorporation of ALP and collagen in multilayers through the LbL method successfully segregated the spatial arrangement of CaP crystallization and the mineralization solution. It imitated the control of biomineralization in space and in time by compartmentalization and homeostasis. The enzyme-assisted mineralization in solutions and multilayers was explored to discover how CaP crystalizes in different conditions or in the vicinity of collagen fibrils.

The literature review in the first chapter addressed the biomineralization mediated by MVs and further mineralization of the collagen matrix. From the process, two biological features were highlighted: (i) homeostasis and (ii) compartmentalization. The homeostasis of phosphate concentration by enzymes in MVs stimulated the use of ALP as an in situ orthophosphate generator for biomimetic CaP mineralization. The compartmentalization in CaP mineralization was achieved by heterogenous catalysis-based systems. In order to design enzyme-assisted CaP mineralization mimicking compartmentalization, the versatile surface functionalization technique, LbL assembly, was adopted and explained the principles of the technique.

In the third chapter, the enzyme, ALP, was introduced in the homogeneous phase in the presence of the substrate of the ALP and calcium ions. The experimental parameters were modified such as the catalytic activity and the concentration of an additional divalent ion. The enzyme-assisted mineralization in different conditions was monitored by real-time light scattering measurements. These experiments shed then a new light on the transition from ACP to HAP, exhibiting and allowing to quantify how the control of the enzyme activity can be tuned to adjust the nucleation rate of ACP particles and highlighting the role of magnesium ions in the retardation of the process but also on the growth rate of the new phase. They also enabled to isolate growth intermediates obtained only in the presence of magnesium ions and displaying remarkable core-shell structures

The fourth chapter showed the enzyme-assisted mineralization in the heterogeneous phase mimicking both homeostasis and compartmentalization. ALP and type I collagen were successfully immobilized in the same multilayers on flat surfaces using the LbL method. The mineralization of multilayers showed the localized CaP crystallization controlled in time and

space by the enzymatic conversion of a substrate to phosphate ions. The comparison of the mineralization between with and without collagen fibrils resulted in the accelerated mineralization in the presence of collagen fibrils by the favor adsorption of ALP. Moreover, the formation of colloidal particles of CaP along the fibrils was observed in the early stage of mineralization, followed by a significant surface coverage of minerals over time. The mineralization of collagen fibrils was also monitored in real time using AFM in the liquid phase. The result suggested the occurrence of intrafibrillar mineralization in the early stages.

Overall, this PhD project investigated the advanced biomimetic system of CaP mineralization through an enzymatic approach. The enzyme-assisted mineralization in multilayers enabled to control of the CaP crystallization in space and time by generating the phosphate precursors in situ and separating the spatial arrangement between the enzyme and mineralization solution. The investigation of CaP mineralization over multilayers revealed the role of collagen fibrils in the formation of the mineral on the surface. Furthermore, the real-time monitoring of the system, performed by AFM in the liquid phase, provided an important clue to distinguish intra- and extra-fibrillar mineralization.

While these results contribute to our understanding of the biomineralization of CaP, it is important to acknowledge that there are numerous challenges and factors yet to be explored from the inherent complexity of biological systems:

i. The phase evolution of CaP mineralization in the biomimetic systems. CaP minerals have various phases as shown in Table 1.2 in Chapter 1. Although the appearances of ACP and HAP in biomineralization have been widely reported, the transition between the two phases is not well elucidated. Especially, the presence of additional molecules or biomacromolecules can influence the kinetic behavior of the possible intermediate phases. For example, as shown in this study: the addition of Mg^{2+} ions in the enzyme-assisted mineralization in the homogeneous phase led to the formation of core-shell structured intermediates. However, the capture of the intermediate phase is typically difficult because of the short lifetime, thermodynamical unstability and sensitivity to the experimental conditions. Therefore, further studies of CaP mineral phases, with additional biomolecules or under biomimetic conditions, that account for the intermediates as biological environments need to be undertaken.

ii. Further mineralization of collagen fibrils: In this thesis, the early stage of collagen fibril mineralization showed the formation of colloidal particles along the collagen fibrils followed by the coverage of entire surfaces. However, it does not describe how to form

well-ordered CaP minerals over the collagen matrix as mineralizing tissues. It leads to the need for further monitoring of CaP crystallization for a longer time or changing the experimental parameters to develop the system.

Moreover, further monitoring can be also associated with mechanical property evolution. As preliminary research, we tried to see the changes in Young's modulus of collagen fibrils. Although the modulus did not change significantly after 1 hour of mineralization, it is expected to differ with longer mineralization especially when extrafibrillar mineralization occurs.

iii. Development of advanced ECM mimicking systems. In this work, the most well-known enzyme, ALP and the most abundant proteins in ECM, collagens, were included. However, in ECM, there are different proteins or enzymes that may influence CaP mineralization such as MVs-bound enzymes or NCPS in ECM as shown in section *1.2.2* or *2.2* in Chapter 1. Therefore, the additional incorporation of extra proteins will advance the biomimetic system for further understanding of CaP mineralization in biological systems. As preliminary work, fetuin-A is introduced to the enzyme-assisted mineralization in a homogeneous phase. The protein is a hepatic plasma protein involved in the metabolism of calcified matrix. When fetuin-A is introduced, the DLS result showed the delayed growth of CaP minerals followed by the formation of well-crystalline HAP (Figure 1).

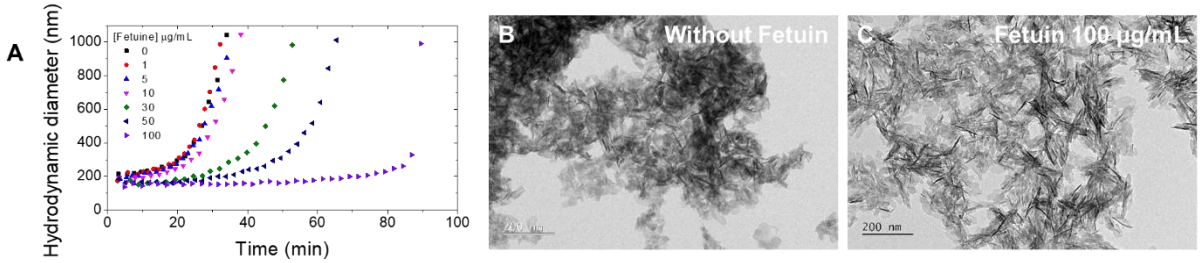

Figure 1. Enzyme-assisted mineralization with the addition of fetuin A. (A) Evolution of hydrodynamic diameter by mineralization time. (B, C) TEM images without fetuin (B) and in the presence of fetuin (C).

Publication and communications

- **Publications**

1. **J. LEE**, A. Konaté, C Guibert & J. Landoulsi, Biomimetic mineral layer over layer-by-layer assemblies: Growth mechanism directed by collagen fibrils, *Surf. Interfaces* **2023** *40*, 103059.
   DOI : 10.1016/j.surfin.2023.103059
2. **J. LEE**, S. Casale, J. Landoulsi & C Guibert, Kinetic study of calcium phosphate mineralization in biomimetic conditions: An enzymatic model approach, *Colloids Surf., B* **2023** *226*, 113290.
   DOI: 10.1016/j.colsurfb.2023.113290
3. E. Colaço, C. Guibert, **J. Lee**, E. Maisonhaute, D. Brouri, C. Dupont-Gillain, K. El Kirat, S. Demoustier-Champagne & J. Landoulsi, Embedding Collagen in Multilayers for Enzyme-Assisted Mineralization: A Promising Way to Direct Crystallization in Confinement, *Biomacromolecules* **2021** 22 (8), 3460-3473.
   DOI: 10.1021/acs.biomac.1c00565

- **Communications**

1. [Oral & Poster*] Enzyme-assisted mineralization of calcium phosphates: role of collagenous and non-collagenous proteins / Jihye LEE, Clément GUIBERT, and Jessem LANDOULSI / 04.11.2022 / JED 2022, Paris France.
   *: Prized

2. [Poster] Real-time study of enzyme-assisted calcium phosphate mineralization / Jihye LEE , Sandra CASALE, Clément GUIBERT, and Jessem LANDOULSI / 20.07.02022 / EKC (Europe-Korea Conference on Science and Technology) 2022, Marseille, France

3. [Oral] Investigating and tuning biomineralization through enzymatic-controlled processes on surfaces / Jihye LEE , Adama Konaté, Clément GUIBERT, and Jessem LANDOULSI / 26.04.2022 / ICASS 2022, Mallorca, Spain